www.nature.com/natbiomedeng / July 2021 Vol. 5 No. 7

nature biomedical engineering

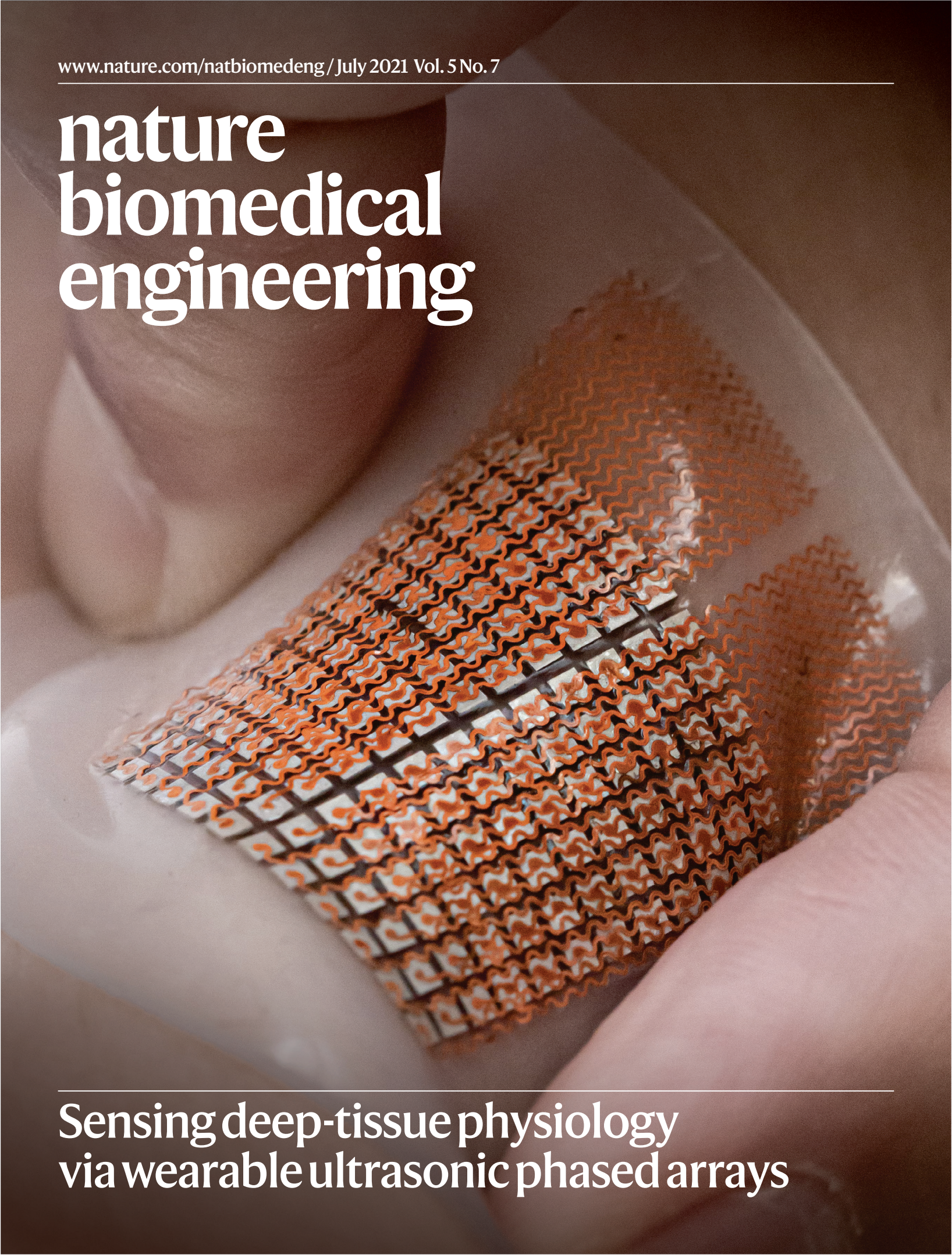

Sensing deep-tissue physiology via wearable ultrasonic phased arrays

nature biomedical engineering

ARTICLES

https://doi.org/10.1038/s41551-021-00763-4

Check for updates

Continuous monitoring of deep-tissue haemodynamics with stretchable ultrasonic phased arrays

Chonghe Wang[1,9,10], Baiyan Qi[2,10], Muyang Lin[1,10], Zhuorui Zhang[1,10], Mitsutoshi Makihata[1], Boyu Liu[1], Sai Zhou[1], Yi-hsi Huang[1], Hongjie Hu[2], Yue Gu[2], Yimu Chen[1], Yusheng Lei[1], Taeyoon Lee[3,4], Shu Chien[5], Kyung-In Jang[6], Erik B. Kistler[5,7] and Sheng Xu[1,2,5,8] ✉

Stretchable wearable devices for the continuous monitoring of physiological signals from deep tissues are constrained by the depth of signal penetration and by difficulties in resolving signals from specific tissues. Here, we report the development and testing of a prototype skin-conformal ultrasonic phased array for the monitoring of haemodynamic signals from tissues up to 14 cm beneath the skin. The device allows for active focusing and steering of ultrasound beams over a range of incident angles so as to target regions of interest. In healthy volunteers, we show that the phased array can be used to monitor Doppler spectra from cardiac tissues, record central blood flow waveforms and estimate cerebral blood supply in real time. Stretchable and conformal skin-worn ultrasonic phased arrays may open up opportunities for wearable diagnostics.

Most chronic diseases directly manifest on one or more deep tissues[1]. Thus, continuous and non-invasive monitoring of physiological signals in deep tissues to interrogate disease initiation and progression is paramount to support clinical decisions for diagnosing and treating chronic diseases[2,3]. However, two major characteristics of deep tissues present challenges to continuous and non-invasive signal acquisition (Fig. 1a). First, they are buried under strongly attenuating tissue layers[4]. Second, object dimensions range from decimetres to micrometres. Therefore, to capture biological parameters in deep tissues of interest, measurement strategies must possess both sufficient penetration depth and high spatial resolution. At present, clinically available imaging techniques that can achieve both, including X-ray computed tomography, magnetic resonance imaging and positron emission tomography, are widely used by trained practitioners. However, due in part to their large footprint and high cost, these modalities are generally only accessible at a tertiary hospital or clinic. There is a critical need for continuous and non-invasive monitoring of anatomies and functions deep beneath the skin surface in both in- and outpatient environments.

Stretchable electronics that place a minimum constraint on the motion of the participant provide an exciting avenue for continuous and non-invasive monitoring of patient conditions[5–7]. Considerable efforts have been expended to overcome the challenges of probing deep tissues with stretchable electronics (Extended Data Fig. 1). Sensing modalities based on optical[8–10], thermal[11,12], chemical[5,13], terahertz[14–16] and radiofrequency[4] mechanisms lack either penetration depth or spatial resolution. Ultrasonic waves have remarkable penetration depth in—and proven biocompatibility with—the human tissues. An unfocused single element has a penetration depth of ~3–4 cm and can sense a region directly beneath it (also known as line-of-sight detection)[17,18]. Considering the complexity of human anatomy[19], it is very challenging to target specific regions with a single element. The phased-array technique, which synchronizes an array of transducers to enhance the energy density and enable beam steering, is ideal for overcoming this challenge[20–22]. Some cell phone-based ultrasound phased arrays can provide accurate diagnoses by clinicians and show great promise, as well as developing trends in the field (for example, https://www.butterflynetwork.com/iq, https://www.usa.philips.com/healthcare/sites/lumify and https://www.sonoque.com/)[23], but these commercial machines are more in the realm of accessibility rather than advancements in technology per se. Also, they are still on rigid substrates with thick profiles[24–27] and require burdensome manual holding during measurements, which precludes them from unobtrusive integration with the human body for continuous and long-term monitoring. There are some efforts on flexible phased arrays that can be integrated on static developable surfaces[4,28,29], but cannot conform to dynamic non-developable biological surfaces. Moreover, these flexible phased arrays have limited spatial resolution, beamforming control and penetration depth. Therefore, stretchable electronics for non-invasive and continuous monitoring of deep tissues in the human body is still a grand challenge (Supplementary Discussions 1 and 2).

Here, we report a stretchable ultrasonic phased array that addresses this critical need (Fig. 1b). The elastic mechanical properties of the device allow for intimate and natural integration with the dynamic non-developable human skin for continuous and

[1]Department of Nanoengineering, University of California, San Diego, La Jolla, CA, USA. [2]Materials Science and Engineering Program, University of California, San Diego, La Jolla, CA, USA. [3]School of Electrical and Electronic Engineering, Yonsei University, Seoul, Republic of Korea. [4]Department of Bio and Brain Engineering, Korea Institute of Science and Technology, Seoul, Republic of Korea. [5]Department of Bioengineering, University of California, San Diego, La Jolla, CA, USA. [6]Department of Robotics Engineering, Daegu Gyeongbuk Institute of Science and Technology, Daegu, Republic of Korea. [7]Department of Anesthesiology and Critical Care, University of California, San Diego, La Jolla, CA, USA. [8]Department of Electrical and Computer Engineering, University of California, San Diego, La Jolla, CA, USA. [9]Present address: John A. Paulson School of Engineering and Applied Sciences, Harvard University, Cambridge, MA, USA. [10]These authors contributed equally: Chonghe Wang, Baiyan Qi, Muyang Lin, Zhuorui Zhang. ✉e-mail: shengxu@ucsd.edu

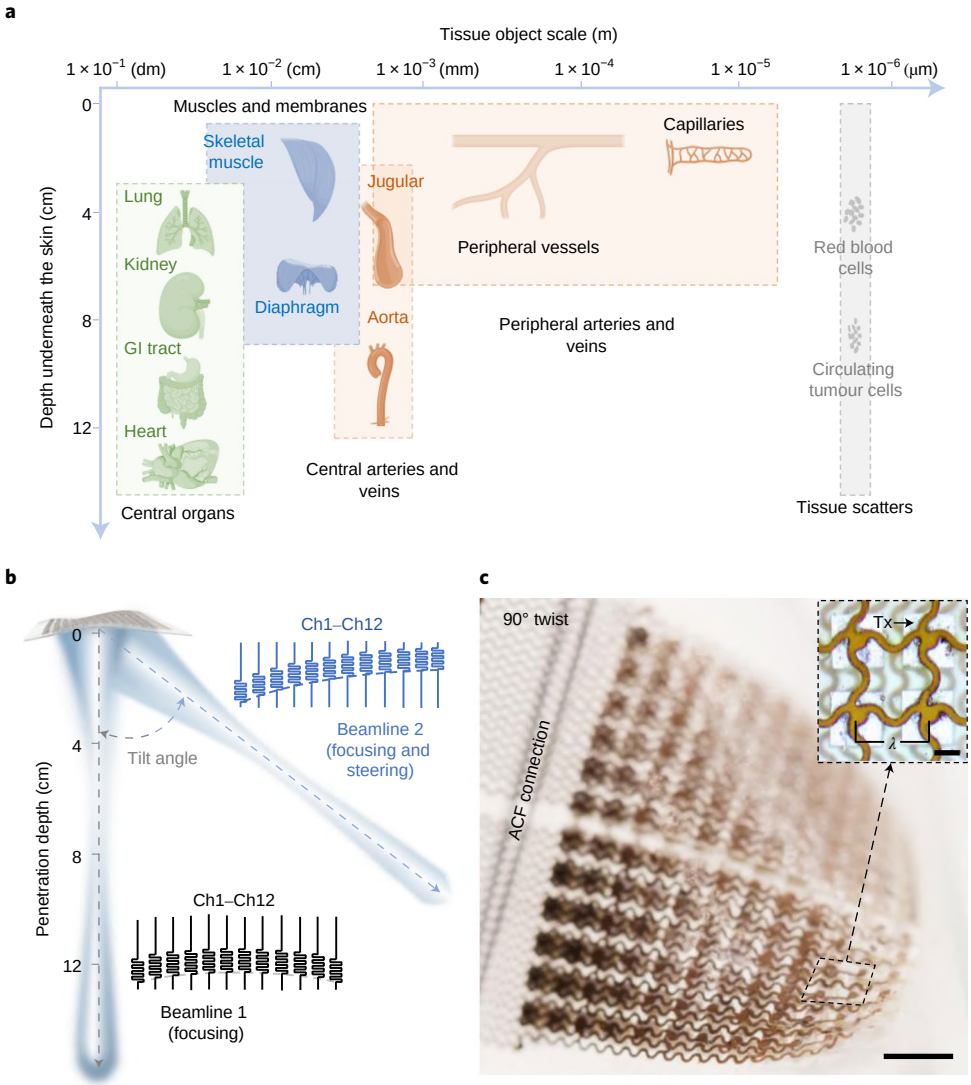

Fig. 1 | Challenges of deep-tissue monitoring and mechanism of the stretchable ultrasonic phased array. a, Depths underneath the skin (*y* axis) and dimensions (*x* axis) of representative human tissues and organs of interest. The stretchable sensor needs to have long penetration depths and to resolve structures at multiple scales. GI, gastrointestinal. **b**, Working principle of ultrasonic phased-array transmit beamforming. With a pre-designed pulse time profile, the phased array can focus and steer the ultrasonic beam to target regions of interest. Beamline 1 illustrates the penetration depth of a focused ultrasonic beam (up to 14 cm in human tissues). Beamline 2 illustrates the focusing and steering of the ultrasonic beam by adjusting the pulse time profile of the phased array. Ch, channel. **c**, Optical image of a 12 × 12 stretchable phased array twisted 90°, with bending and stretching of the interconnects. Inset: magnified image of four transducer (Tx) elements in the array, with an island bridge design and a pitch (λ) of 0.8 mm—approximately one ultrasonic wavelength at 2 MHz according to Huygens' principle. ACF, anisotropic conductive film. Scale bars, 2 mm (main image) and 300 μm (inset). Organ icons in **a** created with BioRender.com.

long-term monitoring. The seamless integration removes air gaps at the device–skin interface, which eliminates the requirement for ultrasound gels typically used for rigid and flexible ultrasonic devices[30]. We applied the phased-array control to every element for transmit and receive beamforming[31,32] (Fig. 1c). The resulting focused ultrasonic beam was much higher in intensity than that of an unfocused single element[17,18], which greatly enhanced the signal-to-noise ratio (SNR) of the reflection signals from deep tissues of dimensions from decimetres to micrometres. The relatively long wavelength of the ultrasonic waves largely enhanced the tolerance of beamforming to the phase aberration induced by the shape change of the device on the human skin. We could control the focal length and steer the direction of the ultrasonic beam from −20° to 20° (Fig. 1b), allowing for active targeting of specific regions of interest in the human body. As a proof of concept, we demonstrated the detection of left and right human heart ventricular Doppler signals ~3–14 cm beneath the skin. The ultrasonic beam could be steered to intercept blood flow at an appropriate Doppler angle, allowing accurate recordings of blood flow spectra in major arteries and veins[33]. Combining the blood flow and vessel dimension measurements, we were able to estimate cerebral blood flow in real time.

Based on Huygens' principle, the ultrasonic wavelength needs to be about the same as the pitch of the phased array to enable high-quality beam convergence[34]. The requirements on penetration depth and resolution place competing needs for the ultrasonic wavelength: a shorter wavelength has a better resolution but a lower penetration depth, and vice versa. We chose a wavelength of 770 μm (corresponding to a centre frequency of ~2 MHz) to reduce

the linear attenuation while maintaining sufficient resolutions[35]. This wavelength provides sufficient penetration for sensing tissues ~14 cm beneath the skin, with sufficient axial and lateral resolutions to differentiate major anatomic structures and fluid dynamics in major vessels[36]. The pitch of the device was therefore designed to be ~770 μm. Additionally, the 770-μm wavelength reduces the sensitivity of individual elements to the phase aberration caused by shape changes of the phased array when integrated on the human body. Each element in the phased array is connected with a serpentine wire to achieve individual element control and system-level stretchability. With a total thickness of 650 μm, the device has a low form factor and can be twisted or stretched. The device can easily conform to non-developable surfaces (Supplementary Figs. 1 and 2) and can be stretched elastically to an equal biaxial strain level of 16%, beyond which the interconnects undergo plastic deformations (Supplementary Fig. 3 and Methods).

The elements show comparable electromechanical coupling to commercial rigid probes, as well as highly consistent centre frequencies and electromechanical coupling coefficients across the entire array (Fig. 2a, Supplementary Fig. 4 and Supplementary Discussion 3)[37]. A single element has a spreading ultrasonic field, which will interfere with that of the adjacent element to create a converged beam at the focal point (Fig. 2b). A lower element frequency leads to a larger insonation area and better convergence (Supplementary Figs. 5 and 6). At the focal point, the beam intensity of a 1 × 12 linear array is much higher than that of the beam from a single element (Supplementary Fig. 7), resulting in substantial penetration of 14 cm in tissues. The phased array delivers 0.47 W cm^{-2} ultrasonic energy to deep tissues, which is within the safe range defined by the Food and Drug Administration (up to 190 W cm^{-2}; Supplementary Discussion 4)[38].

Tuning the pulse time profile of the phased array allows steering of the beam direction of a tilting angle from −20° to 20° in three-dimensional (3D) space (Supplementary Fig. 8, Supplementary Video 1 and Methods). 3D mapping of the ultrasonic beam shows the high penetration depth and excellent beam convergence of the device (Fig. 2c). A long focal length can narrow the beam width and improve the beam directivity, leading to better spatial resolution (Supplementary Fig. 9). The stretchable phased array has a similar beam directivity (in a wide range of tilting angles) to that of a commercial rigid phased array (Supplementary Fig. 10). The axial resolution of the stretchable ultrasonic phased array is much higher than that of electromagnetic devices[4] (Supplementary Discussion 5). The lateral resolution can be further increased with more elements in the linear array, such as from 12 in this study to 128 in commercial devices.

To further enhance the directivity and intensity of the beam, and therefore the lateral resolution and SNR, we excited elements in multiple rows (Supplementary Figs. 8 and 11) and multiple pulses together (Supplementary Figs. 12 and 13). The associated benefits were threefold. First, multi-row excitation generates a more focused ultrasonic beam, which gives a better lateral resolution and produces a higher SNR, which is critical for sensing small reflectors (for example, red blood cells). For imaging applications, the SNR should be above 18 dB[39,40]. In vitro characterization of the SNR along the main beam demonstrated an SNR of >18 dB, even at 20 cm depth for all incident angles (Fig. 2d and Methods). Second, multi-pulse excitation has a much smaller bandwidth. For example, 15 pulses have a bandwidth of 5.72%, compared with 24.58% for a single pulse (Supplementary Fig. 12). A smaller bandwidth leads to a higher sensitivity to the Doppler shift, which is beneficial for sensing small reflectors (Supplementary Discussion 6)[41]. Third, multi-pulse excitation enhances the tolerance of beamforming to shape changes of the stretchable phased array. In this study, activation of a minimum of three rows (a 3 × 12 array) was required to generate sufficient signal strength for sensing haemodynamics in deep tissues. This activation scheme consumes 36 times the power of a single element. The power budget of three rows (0.25 W) is still manageable for wearable devices (Methods).

To date, phased-array beamforming has only been implemented in rigid[24–26] and flexible[27–29] probes, because correcting the phase aberration induced by changes in the pitch of a stretchable phased array remains a grand challenge. When a stretchable device undergoes tensile or compressive strain, each element is displaced from its predefined location, causing deviations in the acoustic interference and thus beamforming. Although auto-correction methods can measure the location of each element and minimize the associated phase aberration[42], the dynamic curvilinear human skin poses a daunting task for tracking elements' locations accurately in real time. In this work, we chose a relatively long wavelength of 770 μm, which has sufficient axial resolution and reflection intensity from small reflectors (Supplementary Discussion 7)[43]. Most importantly, this relatively long wavelength minimizes the sensitivity of beamforming to shape changes of the device in any direction. Moreover, the multi-pulse excitation enables a higher probability of interference; therefore, beamforming is enhanced (Supplementary Fig. 13), which further minimizes the sensitivity of beamforming to device deformation.

To quantify how the long wavelength mitigates the phase aberration, we first investigated the phase error created by the dynamic curvature of the human skin. With a 3D scanner, we measured the minimum curvature radius of a human neck in different postures to be ~4.2 cm (Supplementary Figs. 14 and 15). Figure 2e shows the required pulse time profile for a linear array on a flat surface (blue bars) and deviation on a surface with a curvature radius of ~4.2 cm (orange bars) to create a synthetic wave front at the same focal point. The deviation is the largest for the element on the edge of the array (corresponding to a phase aberration of 4.26%) and is the smallest for the element at the centre (corresponding to a phase aberration of 0.06%). Therefore, at an ultrasonic wavelength of 770 μm, the phase aberration from typical neck skin is relatively small and has

Fig. 2 | Performance characterizations of the stretchable ultrasonic phased array. a, Impedance and phase-angle spectra of a single piezoelectric transducer after integration into the stretchable array, showing a centre frequency of 1.96 MHz, an antiresonance frequency of 2.06 MHz, a phase angle of 75° and an electromechanical coupling factor k_t of 0.61. **b**, Mapped ultrasonic field of a single element transducer (Tx, 2 MHz, 0.55 mm × 0.55 mm × 0.6 mm (length × width × thickness)). The inset is the cross-section of the insonation region in the *x*–*y* plane, with the position and size of the element marked by the square, to show the beam spreading of a single element. Scale bars, 5 mm (main image) and 3 mm (inset). **c**, Mapped ultrasonic field of the phased array in three dimensions. The scale bars in all directions are 1 cm. Inset: magnified cross-section of the ultrasonic field at the focal point, demonstrating good beam convergence in the *x*–*y* plane. Scale bar, 1 cm. **d**, Characterization of the SNR along the beam in water, showing a high SNR at different incident angles. The blue shaded region indicates that an SNR above 18 dB is typically needed for high-quality imaging. **e**, Top: effect of the shift in elements' positions on the phased-array beamforming performance. The blue bars denote the required time delay of the pulse signal sent to each element on a planar surface. The orange bars denote the required correction to achieve the same beamforming outcome on a curved surface with a curvature radius of 4.2 cm (that is, the minimum radius of the human neck in normal postures in this study). Bottom: schematic image showing the propagation and convergence of the synthetic wavefronts of the phased array. **f**, Mapped ultrasonic fields demonstrating beam steering from −20° to 20° on a curved surface with a curvature radius of 4.2 cm. The results show a high-intensity main beam and a low-intensity grating lobe when the incident angle is large. Scale bars, 0.5 cm. Panels **c** and **f** share the same intensity bar.

minimal effect on the phased-array beamforming (Supplementary Discussions 7–9). For theoretical modelling of wave propagation, see Supplementary Video 2.

Then, to test the beamforming of the stretchable ultrasonic phased array on a complex surface, the device was laminated on a tissue-mimicking phantom replicated from the human neck. Testing results showed that on both planar and phantom surfaces the ultrasonic beam could be steered in a wide range of incident angles (Extended Data Fig. 2 and Supplementary Fig. 16). The working range for high-accuracy sensing is defined as the range in which the intensity of the grating lobe is at least −15 dB weaker than the main beam[44]. When the device follows the contours of the phantom, the working range is from −20° to 20° (Fig. 2f), with a 0.1° accuracy of the post-end testing system (Methods). The beam tilting of this phased array enables active targeting of regions of interest over a wide range, which is impossible for single transducers or annular arrays that can only adjust focal depth directly below the transducers[45]. Besides bending, the performance of the phased array was

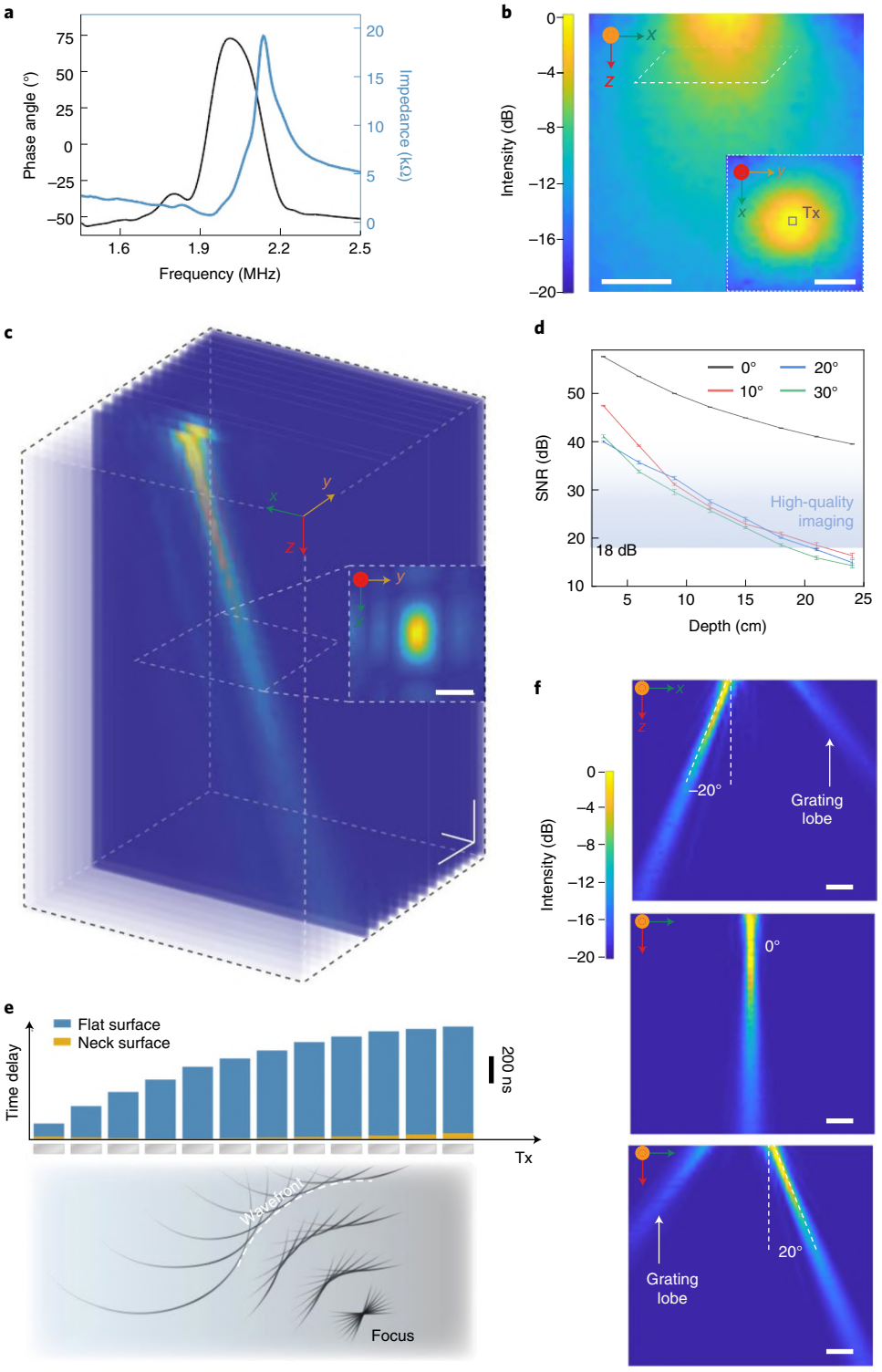

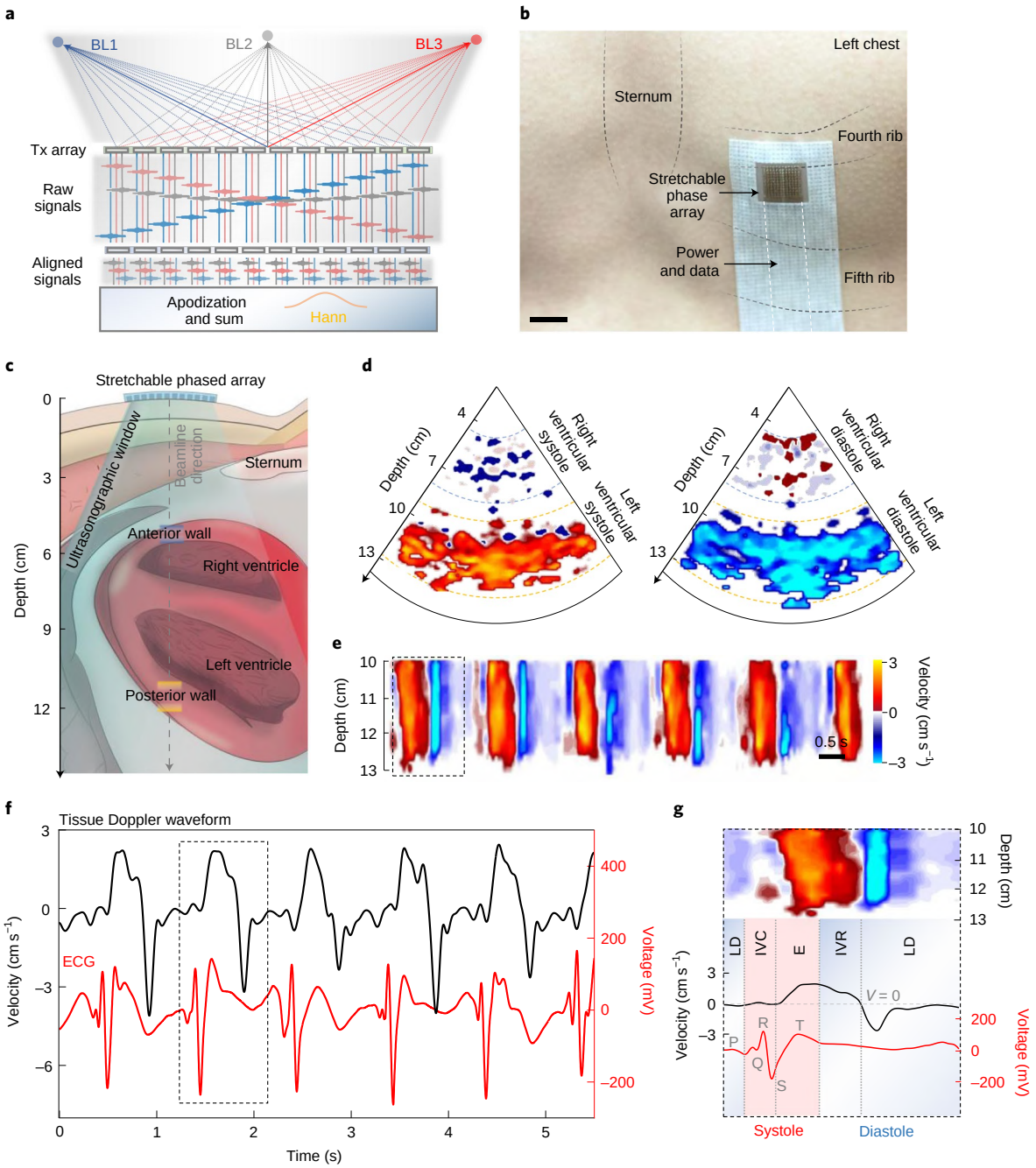

Fig. 3 | Cardiac activity monitoring. a, Working principle of phased-array receive beamforming. The SNR of the signal can be enhanced by delaying and summing the raw signals received by each transducer channel. The signal can be a weighted sum with the choice of proper window functions (for example, the Hanning function) to further enhance the contrast. BL, beamline; Hann, Hanning window function. **b**, Optical image of the device on the human chest. The key components are labelled. Scale bar, 1 cm. **c**, Schematic of the ultrasonographic window used in cardiac activity monitoring. The 0° beamline, anterior wall of the right ventricle (blue) and posterior wall of the left ventricle (orange) are labelled. **d**, Doppler spectra of the ventricles, clearly showing systole (left) and diastole (right) of both the right ventricle and left ventricle. Orange/red indicate tissue movement towards the device, whereas blue indicates movement away from the device. Brighter colours indicate faster tissue movements. **e**, Detailed Doppler spectra analysis of the left ventricle posterior wall, clearly demonstrating systolic and diastolic phases during cardiac cycles. **f**, Tissue Doppler waveform of the left ventricular posterior wall (black curve; showing the systolic and diastolic velocities) and ECG waveform (red curve) measured simultaneously. **g**, Magnified image of simultaneously measured tissue Doppler spectra from the dashed box in **e**, along with the tissue Doppler waveform and ECG signal from the dashed box in **f**, showing the correspondence of the three signals in one cardiac cycle, including systole (red; iso-volumetric contraction (IVC) and ejection (E)) and diastole (blue; iso-volumetric relaxation (IVR) and late diastole (LD)). Panels **d**, **e** and **g** share the same velocity bar.

also characterized under in-plane deformations. The results showed that the beamforming is reliable under 20% tensile or compressive strain, which is typically the maximum strain of the human skin in a natural posture (Supplementary Fig. 17).

With strong penetration and well-controlled beam focusing and steering characteristics, even on curvilinear surfaces, the stretchable ultrasonic phased array has broad implications for targeted deep-tissue monitoring. We focused this technology on cardiovascular

systems that dominate mortality in organ failure[1] and demonstrated two applications: in cardiac tissue Doppler imaging at a depth of ~3–14 cm beneath the skin; and in blood flow spectrum recording (with red blood cells several micrometres in size) for quantitative analysis of central cardiovascular dynamics.

Echocardiography is widely used for non-invasive direct diagnoses of cardiovascular diseases, such as cardiomyopathy[46] and valvular diseases[47–50], but is mostly conducted in clinics only, with data captured only at the point of care[51]. Typical echocardiographic probes are rigid and bulky, making them impractical for chronic patient monitoring. Moreover, obtaining high-quality data from these probes in current clinical settings requires extensive labour and high cost[52]. Longitudinal echocardiographic measurements of cardiac functions have therefore not been available. Monitoring of cardiac functions relies on either invasive probes (for example, pulmonary artery catheter) or non-invasive probes that provide indirect estimates based on relevant parameters (for example, arterial waveform analysis, impedance changes and aortic Doppler). The stretchable ultrasonic phased array, which may be considered as an ultrasound-based Holter monitor, allows direct probing of cardiac sites and interrogation of myocardial dynamics, and thus holds promise for ambulatory management of cardiac functions.

Since ventricular structures are ~3–14 cm beneath the human skin, ventricular signals experience huge attenuation in both the transmitting and receiving processes[53]. The quality of the received signals depends not only on the transmitting beam intensity, but also the receiving performance of the phased array. To enhance the SNR of the received signals, we utilized receive beamforming (Fig. 3a)—a reverse process of the transmit beamforming[31]. The receive beamforming takes into account the signals received by all elements in the array, compensates for their phase differences and then adds up the signals to reconstruct a stronger echo with a higher SNR (Supplementary Fig. 18). With transmit and receive beamforming, the stretchable phased array can detect objects in various orientations up to 17 cm deep in water (Supplementary Fig. 18), as well as tissue-mimicking phantoms (Supplementary Fig. 19 and Supplementary Video 3). The results were validated in the same condition with a commercial device (Supplementary Fig. 19).

Figure 3b,c illustrates the operational setup of the stretchable ultrasonic phased array and schematic cardiac anatomy when the device is placed between the fourth and fifth ribs (Supplementary Fig. 20 and Methods). By decoding the Doppler shift in the entire ultrasonographic window, tissue Doppler images can be reconstructed to show the ventricular wall motions in real time. Figure 3d shows the simultaneous contractions of the right and the left ventricular walls in the systole phase (left) and their relaxation in the diastole phase (right). A close-up of the velocity profile at a depth of ~10–13 cm reveals the periodic systolic and diastolic pattern of the left ventricular posterior wall (Fig. 3e and Extended Data Fig. 3). Figure 3f shows the correlation between the tissue Doppler waveform (black curve) and electrocardiogram (ECG) (red curve; Supplementary Fig. 21 and Methods). Figure 3g shows the tissue Doppler spectrum, waveform and ECG recorded simultaneously. The two phases of systole can be clearly identified. In the iso-volumetric contraction (IVC) phase, the atrioventricular valves close. This IVC phase is then followed by the ejection period, during which the aortic valve opens, blood is discharged into the aorta, and the ventricular ejection reaches its highest velocity. Diastole consists of two phases. The early iso-volumetric relaxation phase is represented by a decrease in the ventricular velocity curve to zero, when all valves are closed. Following this is the late-diastole phase, during which the atrioventricular valves open, allowing the ventricles to begin to refill. The cardiac phases acquired by the stretchable ultrasonic phased array match well with the cardiac cycle traced by the ECG. The measured tissue Doppler provides a direct quantitative assessment of specific myocardium, which complements conventional ECG and stethoscope measurements[49]. The continuous direct insights on anatomies and functions of cardiac tissues offered by the stretchable ultrasonic phased array may be valuable for acute disease prognosis and post-surgery monitoring[54].

Continuous blood flow monitoring can be useful for long-term evaluation of tissues or organs at risks, such as blood supply to the cerebrum or the lower extremities in patients with vascular diseases[11,55–57]. At present, there are several skin- or tissue-integrated devices that show promise for accurate long-term blood flow monitoring[11,58]. However, these devices cannot quantitatively assess the blood flow rate, which is the key to analysing tissue blood supply[59]. Doppler ultrasonography is widely considered as the gold standard for quantitative blood flow measurements in central blood vessels, but similar to echocardiography, Doppler ultrasonography is generally limited to point-of-care applications. The stretchable ultrasonic phased array allows monitoring of blood flow in major arteries and veins quantitatively and continuously.

In this study, we focused on measuring the blood flow in the carotid artery and the neighbouring jugular vein because they are the key pathways for cerebral blood supply and drainage[60]. Compared with specular reflection signals (for example, those from cardiac muscle interfaces), signals from red blood cell scattering have a much lower intensity due to the much smaller size of the scatters (~8 μm in diameter) than the ultrasonic wavelength

Fig. 4 | Central blood flow monitoring. a, Working principle of ultrasonic Doppler sensing. The device sends a focused beam at an incident angle of ~20° to moving red blood cells. Inset: interaction between an ultrasonic pulse and a moving red blood cell. **b**, Optical image of the device on the human neck. The key components are labelled. **c**, Colour flow image reconstructed from reflection signals received by the device. The beam direction is marked by the dashed orange line. The reflection signal intensity is in the grey scale. The insonation area achieved with the stretchable phased array is comparable to a commercially available device (Supplementary Fig. 19). The initial resonance area (whitened area) immediately beneath the device is due to the transducer's ringing effect[71]. The colour flow image clearly shows the jugular venous (blue) and carotid arterial (red) flows with depth and directional information. The magnitude of the flow velocity is in the colour scale, with red flowing towards the device and blue flowing away from it. Fw, forwards; Bw, backwards. **d**,**e**, Colour flow images of the carotid artery (**d**) and jugular vein (**e**). The Doppler angles in **d** and **e** are 58° and 54°, respectively. **f**,**g**, Carotid artery (**f**) and jugular vein (**g**) flow spectra, compared with those of a commercial rigid ultrasonic device. EDV, end-diastolic velocity; PSV, peak systolic velocity. **h**, Bland–Altman analysis of the PSV of carotid arterial flow measured by the stretchable phased array. The stretchable phased array yields a biased error (μ) of 0.046 m s^{-1} and a precision error (σ) of 0.191 m s^{-1}, comparable to the commercial device ($\mu = -0.035$ m s^{-1}; $\sigma = 0.175$ m s^{-1}). **i**, Bland–Altman analysis of the EDV of the carotid arterial flow measured by the stretchable phased array. The stretchable phased array yields $\mu = 0.004$ m s^{-1} and $\sigma = 0.047$ m s^{-1}, comparable to the commercial device ($\mu = -0.002$ m s^{-1}; $\sigma = 0.040$ m s^{-1}). In **h** and **i**, the solid horizontal lines represent the mean difference and the dashed lines represent ±1.96 standard deviations. **j**, Cerebral blood circulation volume calculated by measuring the CBF over a period of 30 min on three participants. Note the spike at minute 15, indicating an exercise-induced increase in CBF. Centre values for minutes 0, 5, 10, 15, 20, 25 and 30, respectively, are 0.71, 0.81, 0.62, 1.56, 0.83, 0.45 and 0.60 l min^{-1} for the stretchable phased array and 0.48, 0.78, 0.6, 1.58, 0.74, 0.45 and 0.80 l min^{-1} for the comparator. Measures of dispersion (σ) for minutes 0, 5, 10, 15, 20, 25 and 30, respectively, are 0.23, 0.11, 0.11, 0.12, 0.16, 0.16 and 0.12 l min^{-1} for the stretchable phased array and 0.04, 0.03, 0.13, 0.11, 0.17, 0.13 and 0.12 l min^{-1} for the comparator. Error bars represent standard deviation of the CBF. Replicates were biological. Scale bars, 1 cm (**b**) and 5 mm (**c**–**e**).

(Supplementary Fig. 22). Phased-array transmit and receive beamforming creates a high SNR, which enables sufficient ultrasonic energy scattered from groups of red blood cells (note that it is not from a single red blood cell) to compute blood flow signals (Supplementary Fig. 23). By extracting the Doppler shift and vessel orientation (Supplementary Figs. 24 and 25), the blood flow velocity can be calculated by equation (1)[33]:

$$V = \frac{c f_d}{2 f_0 \cos\theta} \quad (1)$$

where V is the flow velocity, c is the ultrasonic wave speed in human tissues (~1,540 m s^{-1}), f_d is the captured Doppler shift, f_0 is the centre frequency of the transducer and θ is the Doppler angle between the beam and the blood vessel.

The stretchable phased array is placed on the human neck and the ultrasonic beam is focused and steered to achieve optimal insonation of the carotid artery and jugular vein (Fig. 4a,b). The amplitude and Doppler frequency shift of the received signals can be used to reconstruct a colour flow image (Fig. 4c), which depicts tissue structures in a grey scale and blood flow in a colour scale[61]. To accurately record the flow velocity, the Doppler angle should not exceed 60°, beyond which errors are induced[33] (Fig. 4d,e, Supplementary Figs. 25 and 26 and Methods). The measured flow spectra of the carotid artery and jugular vein show characteristic cardiac pulsation patterns (Fig. 4f,g). The peak systolic and

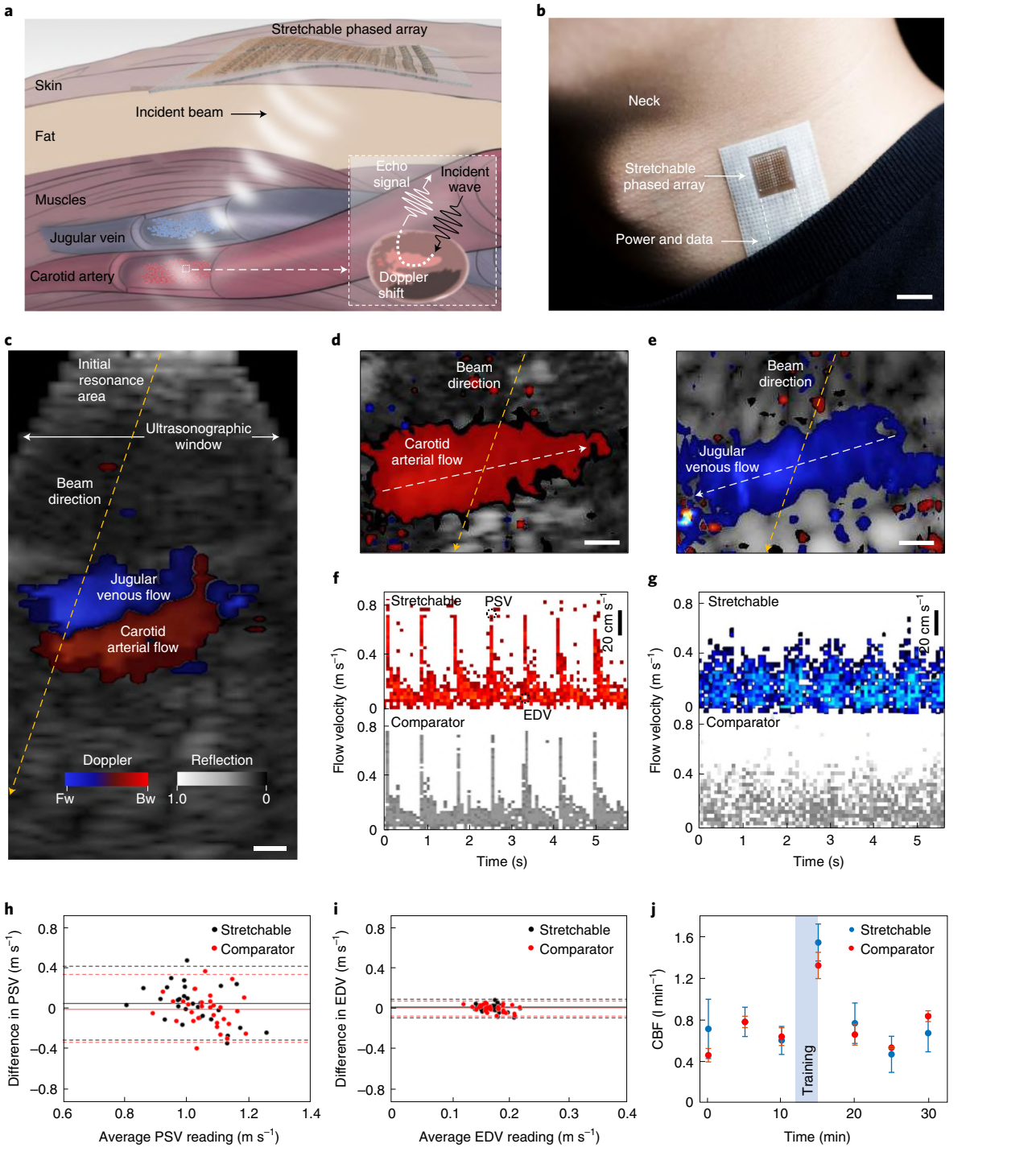

end-diastolic velocities, which are of particular interest for haemodynamic analysis, can be identified directly on the spectra. To validate the results, the stretchable phased array (top curves in Fig. 4f,g) and a commercial phased array (bottom curves in Fig. 4f,g) are used to measure the flow velocity simultaneously (Methods). The measurements were repeated 30 times on three healthy participants with both devices. Bland–Altman analysis of the data shows a high level of agreement, demonstrating that the precision and accuracy of the stretchable device, without any calibration, are comparable to those of the commercial one (Fig. 4h,i)[62]. The stretchable phased array can be readily integrated with the skin, eliminating the need for manual holding and scanning (Supplementary Fig. 27), which enables stable recordings of central blood flow for at least 7 d, with 1 h of continuous recording per day (Supplementary Figs. 28 and 29). The stretchable device is robust with minimal performance degradation after 60 d of repetitive use (Supplementary Fig. 30).

Cerebral blood circulation is critical for sustaining the central nervous system, and it is easily affected by changes in acceleration and microgravity, as well as vascular diseases[63]. So far, it has been difficult to evaluate cerebral circulation using non-invasive methods. Stretchable electronics that can record blood flow volume continuously over the long term meet this critical need[64,65]. Because carotid arteries are the key pathway to the brain, the carotid blood flow (CBF) can be correlated with the volume of cerebral blood circulation[66]. CBF can be measured using a handheld rigid ultrasonic probe. However, this method is limited to diagnosis in the hospital and requires steep operator training, and the results can be highly operator dependent[67].

With the stretchable ultrasonic phased array, the flow velocity inside a blood vessel and the vessel diameter can be measured simultaneously (Supplementary Fig. 31). Multiplying the average CBF velocity by the vessel cross-sectional area yields the CBF (Supplementary Discussion 10). We measured the CBF of a participant over a period of 30 min with 5-min intervals, with the participant resting during the first 12 min then performing a 3-min burpee test during minutes 13–15 (Fig. 4j, shaded in blue) and resting in the last 15 min[68]. From the data, it was clear that at minute 15 the CBF increased from 0.590–1.560 l min^{-1}. After the participant rested for 5 min, the CBF returned to the baseline (Fig. 4j). The results showed good reproducibility, as evidenced by the error bars from three consecutive measurements on the same participant, with a measurement precision of 0.421 l min^{-1} ($n=3$). The CBF measurement results were validated against those from a commercial device (Fig. 4j). During the entire process, seamless integration of the stretchable device to the skin removed the need for ultrasound gel, yielding negligible degradation in signal quality, even with hairs on the skin (Supplementary Figs. 32–34).

The stretchable ultrasonic phased array reported here opens up a new sensing dimension for existing stretchable electronics. The sensing range of the stretchable phased array is no longer limited to areas directly below the device, but expands to a much wider window. The capability of steering the ultrasonic beam enables active targeting of deep tissues of interest. Leveraging the phased-array transmit and receive beamforming, the device has a high SNR and maintains a high resolution for sensing groups of microscale objects, such as red blood cells. The accessible deep tissues are not limited to those studied in this work but can be extended to many others, providing critical capabilities for perfusion monitoring and continuous surveillance of organs at risk for many patients. Technical challenges still remain before we deploy this preliminary prototype to other general settings. For example, the front-end sensor still requires wired data outputs to the back-end acquisition system for post-processing (Supplementary Fig. 35). Ongoing research efforts are focusing on integrating the sensors with on-board signal pre-conditioning, memory and wireless data transmitting, and replacing the power supply with a state-of-the-art flexible lithium-polymer battery. Additionally, the combined strategies of low-frequency and multi-pulse excitation in this work bypass the requirement of calculating the relative position and phase of each element in the phased array. For future applications that require an enhanced spatial resolution, we will develop adaptive algorithms following the time reversal principle, which uses reference points in the tissue to correct the phase aberration of each element induced by the skin deformation.

Methods

Human testing protocols, specifications and anatomical data. The commercial probe used to validate the stretchable phased array was a Verasonics P4-2v phased-array transducer. The P4-2v probe contains 64 elements with a pitch of 0.3 mm, an elevation focus of 50–70 mm and a sensitivity of around −69 to −95 dB. All measurements were conducted following a standard ultrasound probe operational procedure. The blood flow was measured on three healthy participants in a static sitting position. All human tests were approved under University of California, San Diego Institutional Review Board (IRB) protocol 170812. All participants gave voluntary consent to blood flow measurements and skin curvature characterizations. The anatomical data that appear in Figs. 1 and 3, Extended Data Fig. 3 and Supplementary Fig. 20, including the dimensions and locations of central organs and deep tissues, are from the Complete Anatomy platform (copyright 2019; 3D4Medical, Elsevier; https://3d4medical.com/). Using this software, we measured the depth of each listed organ, including the heart, lung, gastrointestinal tract, vascular system and so on. The model used in Complete Anatomy is a representation of a typical human participant; thus, we acknowledge that there may be variations between the model and specific participants with regard to age, gender, ethnicity and body conditions[69].

Biaxial mechanical testing and strain measurement protocols. During tensile testing, we measured the strain by tracking the distance variation between two adjacent elements on a customized stretcher. The tensile experiments were performed under an optical microscope coupled with a charge-coupled device camera and an imaging software system (10× magnification). We were able to continuously and accurately track and measure the centre-to-centre distance of two adjacent elements both laterally and horizontally.

Scalability of the array size, device layout designs, resolution testing, activation scheme, directivity analysis, intensity comparison, power consumption and simulation conditions. The array number was not limited to 12 × 12 in this work. By adopting the fabrication technique of a multi-layered stretchable circuit[70], the array number could be scaled up without physical constraints. The mass production of the stretchable design could be accomplished by standard microfabrication with high yield and low cost. Compared with the unfocused ultrasonic device developed previously[17,18], we decreased the centre frequency of the elements from 7.5 to 2 MHz and reduced the element pitch from 2.5 mm × 2 mm to 0.8 mm × 0.8 mm. Therefore, the element density was increased by 7.8-fold to achieve a higher energy density for deep-tissue penetration. For phased arrays, systems typically employ a $\lambda/2$ pitch to avoid grating lobes. We did not use the $\lambda/2$ pitch here because this $\lambda/2$ pitch would require dicing of the piezoelectric 1–3 composite materials to ~0.3–0.4 mm in size with 1 mm thickness, which was very challenging with the existing facilities. Also, the small pitch would largely reduce the stretchability of the entire device.

The resolution was characterized by applying the line spread function[17]. B mode images were taken in water using the stretchable ultrasonic phased array (with a 4-cm focal length). All radiofrequency data were sampled and processed using the Verasonics system. The beamline tilt resolution was 0.1°, controlled by the Verasonics system. An iron wire with a diameter of 0.5 mm was placed at depths of 5, 10, 20 and 30 cm beneath the device. By calculating the imaged diameter of the iron wire, the axial resolution could be calculated. We activated three rows (36 elements) simultaneously to generate sufficient signal strength to accomplish the applications in this work. The power consumption of the device under this excitation scheme was 0.25 W (25 V, 5,000 Hz and ten pulse excitations). This power budget could potentially be met by a commercial lithium-polymer battery. We observed very minimal heating while using an activating voltage of 25 V (Supplementary Figs. 36–38). The surface temperature of the device barely rose. These results showed the feasibility of integrating the stretchable phased array in a fully wearable system for future low-power, long-term central haemodynamic recording.

The axial resolutions of the stretchable phased array are listed in Supplementary Discussion 5. The directivity, penetration and intensity calculations of the device, as shown in Supplementary Figs. 5–7, 10 and 12, were performed in Field II, MATLAB (MathWorks). Except for the centre frequency and transducer geometry, all conditions were set to be identical, including the input excitation voltage, single-cycle pulse and electromechanical coupling coefficient. The attenuation coefficient of the media was defined as 0.75 dB cm^{-1} MHz^{-1} to mimic human tissues.

System setup, beam steering and optimal insonation adjustment. The stretchable phased array contains two parts, including the front-end probe and the back-end electronics and customized software (Supplementary Fig. 35). The front-end is a stretchable patch, which can be attached to the area of interest on the skin. To

connect all channels to the post-end Verasonics system, we designed a flexible and stretchable elongating region. This elongating region was for strain isolation between the stretchable front-end patch and the rigid adaptor and the post-end system (Supplementary Fig. 35). The length of the elongating region was decided by the application needs in consideration of the distance between the post-end system and the human participant. The elongating region was bonded to an anisotropic conductive film, which was then connected to a customized circuit board. The circuit board contained an array of Bayonet Neill–Concelman connectors and cables, which could be connected to the Verasonics system for signal processing and analysis. The participant under test could freely move in a considerable range with the patch adhered to the skin surface. The back-end electronics and customized software were all contained in the Verasonics system (Vantage 64). The ultrasonic beam could be steered to any pre-designed angle instantly. After laminating the patch on the skin, we first adopted the mode of colour flow image to locate the tissue of interest, including the depth and orientational angle relative to the device centre. Then, we adjusted the optimal insonation, which used the relative positional information to steer the ultrasonic beam to the region of interest.

SNR measurements. The SNR data were measured using a 3D ultrasonic mapping system (AIMS III hydrophone scanning system; Onda Corporation). The key components of the system include an automated scanning tank, a motion controller, an oscilloscope and a computer with embedded imaging software. The automated scanning tank is composed of a 3D linear motor, a rotator and a hydrophone, which can achieve 3D spatial and angular mapping of ultrasonic fields (positioning repeatability: <5 μm; x, y, z step size = 5.5 μm).

The SNR of any given point in the ultrasonic field was measured and calculated via equation (2):

$$\mathrm{SNR} = 20\log[\frac{V_{\mathrm{beam}}}{V_{\mathrm{noise}}}] \quad (2)$$

where V_{beam} is the peak voltage at a specific spatial point of the ultrasonic beam measured by the hydrophone, and V_{noise} is the voltage amplitude of the noise in the A mode measured by the hydrophone.

ECG measurements. ECG was simultaneously recorded with the tissue Doppler imaging on the same participant using the SphygmoCor EM3 device (AtCor Medical) (Supplementary Fig. 21). The healthy participant was in a sitting position with an ECG electrode on each arm and a common ground electrode on the left leg above the ankle.

Maximum skin curvature and strain characterization of the human neck. The skin curvature of the human neck was characterized using a high-resolution 3D scanner (HDI Advance; LMI Technologies). The field of view (FOV)-dependent accuracy of the scanner is 40 μm at 200 mm FOV, 65 μm at 400 mm FOV and 85 μm at 600 mm FOV. The duration was 1.2 s per scan. Skin curvatures were measured on 20 participants of different age, gender and ethnicity (Supplementary Fig. 14). The 3D scanning and model reconstruction were carried out with the FlexScan3D software (Polyga). The skin strain was measured on three participants in four postures, including head rotation to the left and right (with yaw angles from −60° to 60°) and flexion/extension (with pitch angles from −37° to 30°).

Colour flow image, tissue Doppler processing, filtering and vessel angle recognition. The colour flow imaging was applied to cardiac tissue Doppler imaging and blood flow imaging. The spectrum was decoded and displayed instantly by Verasonics. For cardiac tissue Doppler imaging, since the left and right ventricles have a depth range of ~3–14 cm, we extracted the Doppler signal in the entire ultrasonographic window. The tissue Doppler waveform was extracted by averaging the speed of the spectrum signal from a tissue depth of 10–13 cm. For blood flow imaging, we adopted a range-gated method to selectively extract Doppler signals from the vessel lumen region, so that the Doppler signals from pulsating vessel walls were removed. The vessel angle was calculated from the colour flow image using an image-processing algorithm. A finite impulse response filter (13 taps; −60 dB at a pulse-repetitive frequency of <0.003 and −3 dB at a pulse-repetitive frequency of 0.08) was added to improve the image quality. All of the coloured pixels in the vessel lumen region were used to calculate the flow direction vector, and to estimate the vessel angle and, therefore, the Doppler angle for calculating the flow velocities.

CBF measurements. As shown in Supplementary Fig. 31, there was a 4 × 5 unfocused ultrasonic patch (7.5 MHz) laminated at the top and a phased-array patch (2 MHz) laminated at the bottom. The 7.5-MHz patch was used for carotid artery blood vessel diameter recording, whereas the 2-MHz patch was for blood flow recording. We used the 7.5-MHz patch for recording the vessel diameter, which needed a high spatial resolution for resolving tissue interfaces. We used the 2-MHz patch for recording the flow velocity, which had a sufficient SNR. The 7.5-MHz patch directly recorded the vessel diameter underneath. The 2-MHz patch focused and steered the beam with a certain incident angle towards the 7.5-MHz patch direction so that we could study the vessel diameter and blood flow velocity at the same location. In this way, we could monitor and correlate these two physiological signals simultaneously. The required tilting angle depended on the inclination angle of the carotid artery. Due to the large difference in centre frequencies (7.5 and 2 MHz), there was not any noticeable crosstalk that would affect the signal quality of either patch.

Reporting Summary. Further information on research design is available in the Nature Research Reporting Summary linked to this article.

Data availability

The main data supporting the results in this study are available within the paper and its Supplementary Information. Data generated in this study, including source data and the data used to produce the figures, are available from Harvard Dataverse at https://dataverse.harvard.edu/dataset.xhtml?persistentId=doi:10.7910/DVN/EPITIY.

Received: 24 July 2020; Accepted: 10 June 2021;
Published online: 16 July 2021

References

1. Tran, D. D., Groeneveld, A., Nauta, J., van Schijndel Strack, R. & Thijs, L. Age, chronic disease, sepsis, organ system failure, and mortality in a medical intensive care unit. *Crit. Care Med.* **18**, 474–479 (1990).
2. Knaus, W. A., Draper, E. A., Wagner, D. P. & Zimmerman, J. E.Prognosis in acute organ-system failure. *Ann. Surg.* **202**, 685–693 (1985).
3. Tsai, M.-H. et al. Organ system failure scoring system can predict hospital mortality in critically ill cirrhotic patients. *J. Clin. Gastroenterol.* **37**, 251–257 (2003).
4. Agrawal, D. R. et al. Conformal phased surfaces for wireless powering of bioelectronic microdevices. *Nat. Biomed. Eng.* **1**, 0043 (2017).
5. Gao, W. et al. Fully integrated wearable sensor arrays for multiplexed in situ perspiration analysis. *Nature* **529**, 509–514 (2016).
6. Someya, T., Bao, Z. & Malliaras, G. G. The rise of plastic bioelectronics. *Nature* **540**, 379–385 (2016).
7. Rogers, J. A., Someya, T. & Huang, Y. Materials and mechanics for stretchable electronics. *Science* **327**, 1603–1607 (2010).
8. Kim, J. et al. Battery-free, stretchable optoelectronic systems for wireless optical characterization of the skin. *Sci. Adv.* **2**, e1600418 (2016).
9. Chung, H. U. et al. Binodal, wireless epidermal electronic systems with in-sensor analytics for neonatal intensive care. *Science* **363**, eaau0780 (2019).
10. Khan, Y. et al. A flexible organic reflectance oximeter array. *Proc. Natl Acad. Sci. USA* **115**, E11015–E11024 (2018).
11. Webb, R. C. et al. Epidermal devices for noninvasive, precise, and continuous mapping of macrovascular and microvascular blood flow. *Sci. Adv.* **1**, e1500701 (2015).
12. Tian, L. et al. Flexible and stretchable 3ω sensors for thermal characterization of human skin. *Adv. Funct. Mater.* **27**, 1701282 (2017).
13. Kim, J., Campbell, A. S., de Ávila, B. E.-F. & Wang, J. Wearable biosensors for healthcare monitoring. *Nat. Biotech.* **37**, 389–406 (2019).
14. Suzuki, D., Oda, S. & Kawano, Y. A flexible and wearable terahertz scanner. *Nat. Photon.* **10**, 809–813 (2016).
15. Garbacz, P. Terahertz imaging—principles, techniques, benefits, and limitations. *J. Mach. Constr. Maint.* **1**, 81–92 (2016).
16. You, B., Chen, C.-Y., Yu, C.-P., Wang, P.-H. & Lu, J.-Y. Frequency-dependent skin penetration depth of terahertz radiation determined by water sorption–desorption. *Opt. Express* **26**, 22709–22721 (2018).
17. Hu, H. et al. Stretchable ultrasonic transducer arrays for three-dimensional imaging on complex surfaces. *Sci. Adv.* **4**, eaar3979 (2018).
18. Wang, C. et al. Monitoring of the central blood pressure waveform via a conformal ultrasonic device. *Nat. Biomed. Eng.* **2**, 687–695 (2018).
19. Schulze, R. K., Ćurić, D. & d'Hoedt, B. B-mode versus A-mode ultrasonographic measurements of mucosal thickness in vivo. *Oral. Surg. Oral. Med. Oral. Pathol. Oral. Radiol. Endod.* **93**, 110–117 (2002).
20. Van Keuk, G. & Blackman, S. S. On phased-array radar tracking and parameter control. *IEEE Trans. Aerosp. Electron. Syst.* **29**, 186–194 (1993).
21. Saucan, A.-A., Chonavel, T., Sintes, C. & Le Caillec, J.-M. CPHD-DOA tracking of multiple extended sonar targets in impulsive environments. *IEEE Trans. Signal Process.* **64**, 1147–1160 (2015).
22. Nissen, S. E. et al. Application of a new phased-array ultrasound imaging catheter in the assessment of vascular dimensions. In vivo comparison to cineangiography. *Circulation* **81**, 660–666 (1990).
23. Baribeau, Y. et al. Hand-held point of care ultrasound probes—the new generation of POCUS. *J. Cardiothorac. Vasc. Anesth.* **34**, 3139–3145 (2020).
24. Cheng, J., Potter, J. N., Croxford, A. J. & Drinkwater, B. W. Monitoring fatigue crack growth using nonlinear ultrasonic phased array imaging. *Smart Mater. Struct.* **26**, 055006 (2017).
25. J. Lee, H.-S. & Sodini, C. G. in *Intracranial Pressure & Neuromonitoring XVI* 111–114 (Springer, 2018).
26. Daum, D. R., Smith, N. B., King, R. & Hynynen, K. In vivo demonstration of noninvasive thermal surgery of the liver and kidney using an ultrasonic phased array. *Ultrasound Med. Biol.* **25**, 1087–1098 (1999).

27. Shi, K., Que, K. & Guo, D. Flexible ultrasonic phased-array probe. *Tsinghua Sci. Technol.* **9**, 574–577 (2004).
28. Bhuyan, A. et al. Miniaturized, wearable, ultrasound probe for on-demand ultrasound screening. In *Proc. IEEE International Ultrasonics Symposium* 1060–1063 (IEEE, 2011).
29. Pashaei, V. et al. Flexible body-conformal ultrasound patches for image-guided neuromodulation. *IEEE Trans. Biomed. Circuits Syst.* **14**, 305–318 (2019).
30. Abdelfattah, R. et al. Outbreak of *Burkholderia cepacia* bacteraemia in a tertiary care centre due to contaminated ultrasound probe gel. *J. Hosp. Infect.* **98**, 289–294 (2018).
31. Thomenius, K. E. Evolution of ultrasound beamformers. In *Proc. IEEE International Ultrasonics Symposium* 1615–1622 (IEEE, 1996).
32. Smith, S. W., Pavy, H. G. & von Ramm, O. T. High-speed ultrasound volumetric imaging system. I. Transducer design and beam steering. *IEEE T. Ultrason. Ferr.* **38**, 100–108 (1991).
33. Gill, R. W. Measurement of blood flow by ultrasound: accuracy and sources of error. *Ultrasound Med. Biol.* **11**, 625–641 (1985).
34. Wooh, S.-C. & Shi, Y. A simulation study of the beam steering characteristics for linear phased arrays. *J. Nondestruct. Eval.* **18**, 39–57 (1999).
35. Cloostermans, M. & Thijssen, J. A beam corrected estimation of the frequency dependent attenuation of biological tissues from backscattered ultrasound. *Ultrason. Imaging* **5**, 136–147 (1983).
36. Ng, A. & Swanevelder, J. Resolution in ultrasound imaging. *Continuing Educ. Anaesthesia Crit. Care Pain* **11**, 186–192 (2011).
37. Gururaja, T. et al. Piezoelectric composite materials for ultrasonic transducer applications. Part I: resonant modes of vibration of PZT rod-polymer composites. *IEEE Trans. Sonics Ultrason.* **32**, 481–498 (1985).
38. Food & Drug Administration *Marketing Clearance of Diagnostic Ultrasound Systems and Transducers* (Center for Devices and Radiological Health, 2019).
39. Gazit, S., Szameit, A., Eldar, Y. C. & Segev, M. Super-resolution and reconstruction of sparse sub-wavelength images. *Opt. Express* **17**, 23920–23946 (2009).
40. Mills, D. M. Medical imaging with capacitive micromachined ultrasound transducer (CMUT) arrays. In *Proc. IEEE Ultrasonics Symposium* 384–390 (IEEE, 2004).
41. Ophir, J., McWhirt, R., Maklad, N. & Jaeger, P. A narrowband pulse-echo technique for in vivo ultrasonic attenuation estimation. In *Proc. IEEE Transactions on Biomedical Engineering* 205–212 (IEEE, 1985).
42. Hunter, A. J., Drinkwater, B. W., Wilcox, P. & Russell, J. Automatic image correction for flexible ultrasonic phased array inspection. In *Proc. 8th International Conference on NDE in Relation to Structural Integrity for Nuclear and Pressurised Components* (JRC-NDE, 2010).
43. Shung, K. K., Sigelmann, R. A. & Reid, J. M. Scattering of ultrasound by blood. In *Proc. IEEE Transactions on Biomedical Engineering* 460–467 (IEEE, 1976).
44. Von Ramm, O. T. & Smith, S. W. Beam steering with linear arrays. In *Proc. IEEE Transactions on Biomedical Engineering* 438–452 (IEEE, 1983).
45. Ketterling, J. A., Aristizabal, O., Turnbull, D. H. & Lizzi, F. L. Design and fabrication of a 40-MHz annular array transducer. *IEEE Trans. Ultrason. Ferroelectr. Freq. Control* **52**, 672–681 (2005).
46. Abbasi, A. S., Chahine, R. A., Mac Alpin, R. N. & Kattus, A. A. Ultrasound in the diagnosis of primary congestive cardiomyopathy. *Chest* **63**, 937–942 (1973).
47. Mohan, J. C. *A Practical Approach to Clinical Echocardiography* (JP Medical, 2014).
48. Ommen, S. R. et al. Clinical utility of Doppler echocardiography and tissue Doppler imaging in the estimation of left ventricular filling pressures: a comparative simultaneous Doppler-catheterization study. *Circulation* **102**, 1788–1794 (2000).
49. Galiuto, L., Ignone, G. & DeMaria, A. N. Contraction and relaxation velocities of the normal left ventricle using pulsed-wave tissue Doppler echocardiography. *J. Am. Coll. Cardiol.* **81**, 609–614 (1998).
50. Søgaard, P. et al. Tissue Doppler imaging predicts improved systolic performance and reversed left ventricular remodeling during long-term cardiac resynchronization therapy. *Am. J. Cardiol.* **40**, 723–730 (2002).
51. Auricchio, A. et al. Long-term clinical effect of hemodynamically optimized cardiac resynchronization therapy in patients with heart failure and ventricular conduction delay. *Am. J. Cardiol.* **39**, 2026–2033 (2002).
52. Auricchio, A. & Abraham, W. T. Cardiac resynchronization therapy: current state of the art: cost versus benefit. *Circulation* **109**, 300–307 (2004).
53. Thimot, J. & Shepard, K. L. Bioelectronic devices: wirelessly powered implants. *Nat. Biomed. Eng.* **1**, 0051 (2017).
54. Joyner, C. R. Jr, Hey, E. B. Jr, Johnson, J. & Reid, J. M. Reflected ultrasound in the diagnosis of tricuspid stenosis. *Am. J. Cardiol.* **19**, 66–73 (1967).
55. Flammer, A. J. et al. The assessment of endothelial function: from research into clinical practice. *Circulation* **126**, 753–767 (2012).
56. Petrofsky, J. S. Resting blood flow in the skin: does it exist, and what is the influence of temperature, aging, and diabetes? *J. Diabetes Sci. Technol.* **6**, 674–685 (2012).
57. Herholz, K. et al. Regional cerebral blood flow in patients with leuko-araiosis and atherosclerotic carotid artery disease. *Arch. Neurol.* **47**, 392–396 (1990).
58. Boutry, C. M. et al. Biodegradable and flexible arterial-pulse sensor for the wireless monitoring of blood flow. *Nat. Biomed. Eng.* **3**, 47–57 (2019).
59. Dymling, S. O., Persson, H. W. & Hertz, C. H. Measurement of blood perfusion in tissue using Doppler ultrasound. *Ultrasound Med. Bio.* **17**, 433–444 (1991).
60. Chung, C. P. et al. More severe white matter changes in the elderly with jugular venous reflux. *Ann. Neurol.* **69**, 553–559 (2011).
61. Merritt, C. R. Doppler colour flow imaging. *J. Clin. Ultrasound* **15**, 591–597 (1987).
62. Bland, J. M. & Altman, D. Statistical methods for assessing agreement between two methods of clinical measurement. *Lancet* **327**, 307–310 (1986).
63. Bondar, R. L. et al. Cerebral blood flow velocities by transcranial Doppler during parabolic flight. *J. Clin. Pharmacol.* **31**, 915–919 (1991).
64. Jawad, K., Miller, J. D., Wyper, D. J. & Rowan, J. O. Measurement of CBF and carotid artery pressure compared with cerebral angiography in assessing collateral blood supply after carotid ligation. *J. Neurosurg.* **46**, 185–196 (1977).
65. Cope, M. & Delpy, D. T. System for long-term measurement of cerebral blood and tissue oxygenation on newborn infants by near infra-red transillumination. *Med. Biol. Eng. Comput.* **26**, 289–294 (1988).
66. Soustiel, J. et al. Assessment of cerebral blood flow by means of blood-flow-volume measurement in the internal carotid artery: comparative study with a 133xenon clearance technique. *Stroke* **34**, 1876–1880 (2003).
67. Gunst, M. et al. Accuracy of cardiac function and volume status estimates using the bedside echocardiographic assessment in trauma/critical care. *J. Trauma Acute Care Surg.* **65**, 509–516 (2008).
68. Podstawski, R., Kasietczuk, B., Boraczyński, T., Boraczyński, M. & Choszcz, D. Relationship between BMI and endurance-strength abilities assessed by the 3 minute burpee test. *Int. J. Sports Sci.* **3**, 28–35 (2013).
69. Ma, Y.-C., Peng, C.-T., Huang, Y.-C., Lin, H.-Y. & Lin, J.-G.The depths from skin to the major organs at chest acupoints of pediatric patients. *Evid. Based Complement. Altern. Med.* **2015**, 126028 (2015).
70. Huang, Z. et al. Three-dimensional integrated stretchable electronics. *Nat. Electron.* **1**, 473–480 (2018).
71. Burckhardt, C. B. Speckle in ultrasound B-mode scans. *IEEE Trans. Sonics Ultrason.* **25**, 1–6 (1978).
72. Liu, Y. et al. Epidermal mechano-acoustic sensing electronics for cardiovascular diagnostics and human-machine interfaces. *Sci. Adv.* **2**, e1601185 (2016).
73. Delgado-Trejos, E., Quiceno-Manrique, A., Godino-Llorente, J., Blanco-Velasco, M. & Castellanos Dominguez, G. Digital auscultation analysis for heart murmur detection. *Ann. Biomed. Eng.* **37**, 337–353 (2009).
74. Lee, K. et al. Mechano-acoustic sensing of physiological processes and body motions via a soft wireless device placed at the suprasternal notch. *Nat. Biomed. Eng.* **4**, 148–158 (2019).

Acknowledgements

We thank Z. Wu and L. Chen for guidance on the ultrasonic imaging algorithm and data processing; S. Xiang for feedback on manuscript preparation; and Y. Hu and Z. Liu for advice on the cardiac tissue Doppler experiments. The content is solely the responsibility of the authors and does not necessarily represent the official views of the National Institutes of Health (NIH). All biological experiments were conducted in accordance with the ethical guidelines of the NIH and with the approval of the IRB of the University of California, San Diego (IRB number 170812). We acknowledge support from the NIH (grant 1R21EB027303-01A1) and the Center for Wearable Sensors at the University of California, San Diego.

Author contributions

C.W., B.Q., M.L., Z.Z. and S.X. designed the research. C.W., B.Q., M.L., B.L. and Z.Z. performed the experiments. C.W., B.Q. and Z.Z. performed the simulations. C.W., Z.Z., B.Q. and M.L. analysed the data. C.W. and S.X. wrote the paper. All authors provided active and valuable feedback on the manuscript.

Competing interests

The authors declare no competing interests.

Additional information

Extended data is available for this paper at https://doi.org/10.1038/s41551-021-00763-4.

Supplementary information The online version contains supplementary material available at https://doi.org/10.1038/s41551-021-00763-4.

Correspondence and requests for materials should be addressed to S.X.

Peer review information *Nature Biomedical Engineering* thanks John Ho and the other, anonymous, reviewer(s) for their contribution to the peer review of this work.

Reprints and permissions information is available at www.nature.com/reprints.

Publisher's note Springer Nature remains neutral with regard to jurisdictional claims in published maps and institutional affiliations.

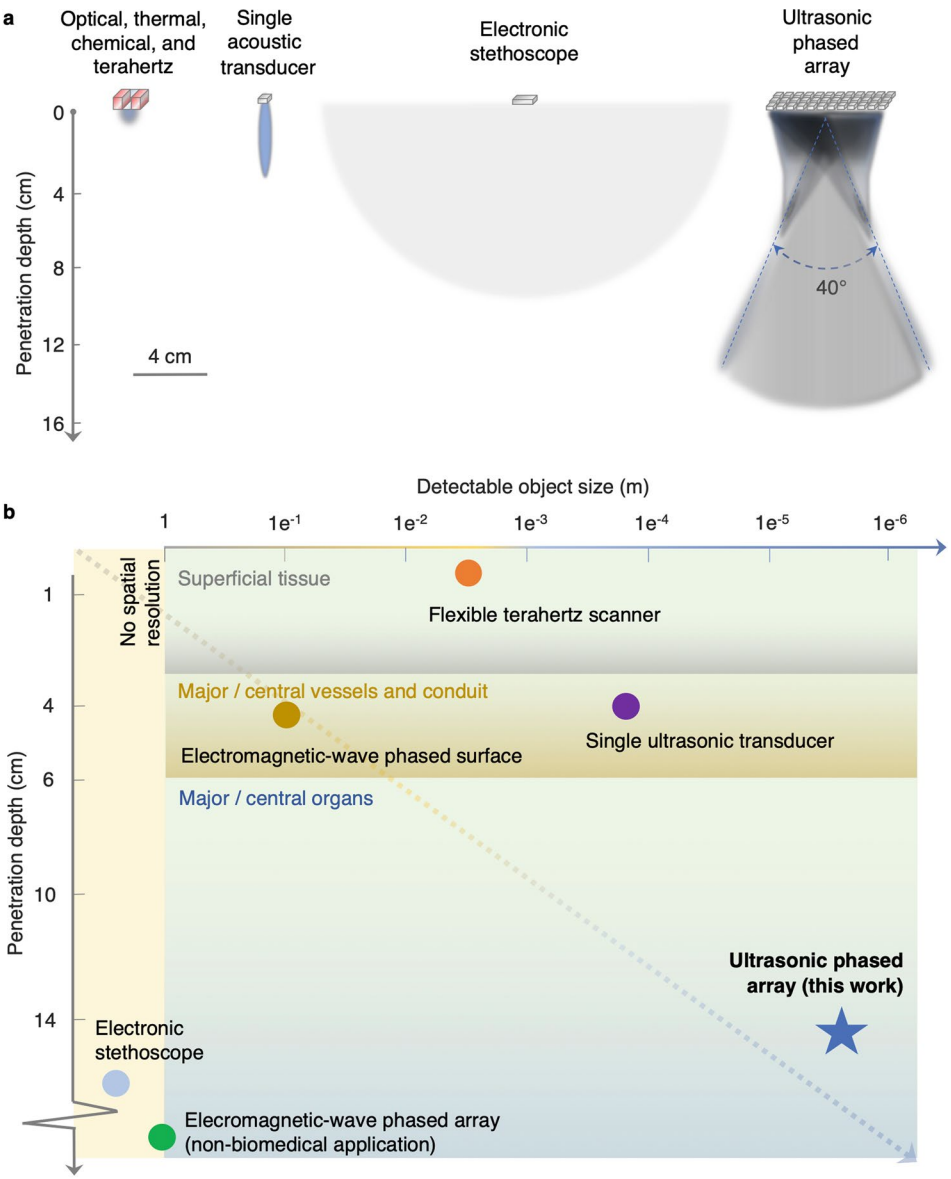

Extended Data Fig. 1 | Comparison of existing flexible or stretchable electronic devices for deep-tissue monitoring. a, Comparison of the detection range (shaded areas underneath each sensing mode) of the stretchable phased array with all other flexible/stretchable biosensors, including optoelectronics, thermal electronics, iontophoresis based electrochemical sensors, terahertz wave-based sensors, a single ultrasonic transducer, and electronic stethoscopes. The phased array has distinct advantages compared to the other sensing modalities in both penetration depth and spatial resolution. With phased array beamforming, the stretchable ultrasonic probe can focus the beam to achieve longer penetration (up to 14 cm in human tissues) and steer the beam to scan over a 40° range with a high signal-to-noise ratio (SNR). The insonation area in 2D can reach ~68.41 cm^2, 380 times larger than the insonation area of a single element, ~0.18 cm^2, calculated by Field II, MATLAB, MathWorks, Natick, MA. **b**, Comparison of the penetration depth and detectable object size of representative flexible/stretchable biosensors in the literature. Stretchable optoelectronics illuminates the tissue to analyze changes in blood oxygen saturation, but the depth of penetration is generally limited to ~8 mm[8–10]. Stretchable thermal electronics suffer from similar limitations[11,12]. Although flexible terahertz devices show high penetration in dielectric materials[14], terahertz electromagnetic waves attenuate quickly in water[15], leading to a maximum penetration depth of only 0.3 mm in the human tissue[16]. Flexible electromagnetic devices in the frequency range of ~GHz can penetrate more than 5 cm of human tissue, but their spatial resolution ranges from 5 to 50 cm, which is inadequate for most biomedical applications[4]. Stretchable stethoscopes based on kinematics can sense vibrations far beneath the skin[72]; but due to the omnidirectional propagation of vibrations, these devices can receive signals from all organs in their sensing range, and thus lack spatial resolution[73,74]. Additionally, they can only detect low-frequency pulsations, missing critical information from static objects (for example, their location, dimension, and modulus) or high-frequency pulsations (for example, hemodynamics). The result shows the stretchable phased array has a long penetration depth with sufficient resolving capabilities for deep tissue monitoring.

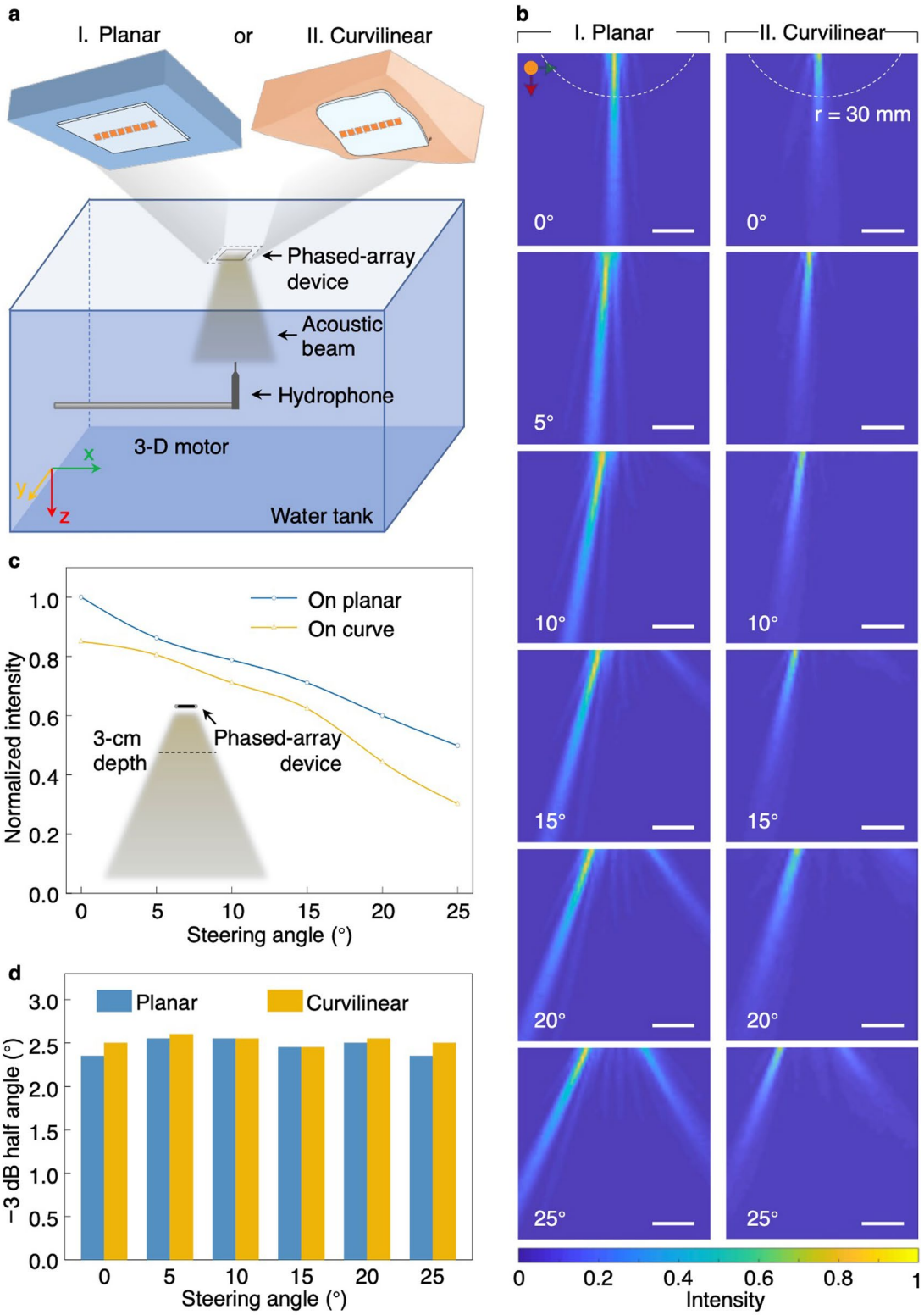

Extended Data Fig. 2 | Performance of the stretchable phased array at all incidence angles in the *xz* plane on the phantom replicated from the human neck. a, A schematic setup of the characterization. Ultrasonic field mapping is carried out with the stretchable phased array on a flat (top left) or a curvilinear (top right) surface. The characterization system is composed of a water tank and a 3D motor system with a hydrophone at its tip. **b**, Mapped ultrasonic fields with the stretchable phased array on a flat (left) or a curvilinear (right) surface with an incidence angle range of 0° - 25°. Scale bars are 2 cm. **c**, Normalized beam intensity of the stretchable phased array at a typical carotid artery depth (~3 cm) with different incident angles. The inset illustrates the depth at which the intensity measurements are taken. **d**, Beam directivity of the stretchable phased array at a typical carotid artery depth (~3 cm) with different incident angles. The beam directivity of the stretchable phased array is comparable on the two surfaces at all incident angles in the range tested.

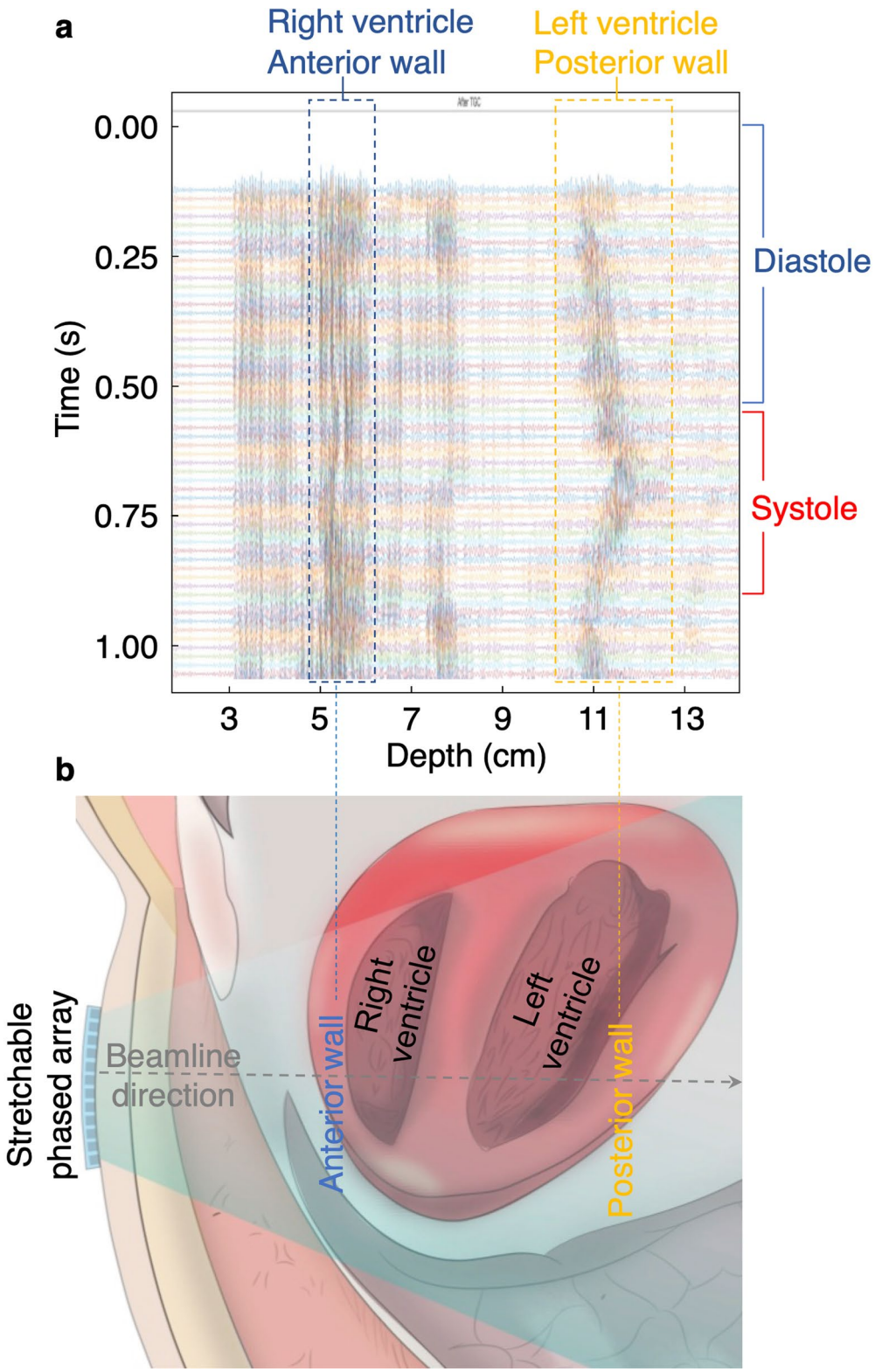

Extended Data Fig. 3 | Raw radiofrequency signals of the tissue Doppler in the time domain, and corresponding human anatomy. a, Raw radiofrequency signals of the tissue Doppler in one cardiac cycle. Note that the y-axis is time. The x-axis is converted to depth by multiplying the ultrasonic speed by the time-of-flight of ultrasonic pulses in the human tissue. As a proof of concept, we neglect the non-uniformity of the ultrasonic speed in the human body. From the pattern, we can clearly observe the reflection peaks from the anterior wall of the right ventricle (RV) in the blue dashed box and the posterior wall of the left ventricle (LV) in the orange dashed box. The positions of the reflection peaks shift during the cardiac cycle. The RV anterior wall peak shifts to the left from 0 to 0.6 s, corresponding to RV diastole, and shifts to the right from 0.6 to 0.8 s, corresponding to RV systole. Meanwhile, the LV posterior wall peak shifts to the right from 0 to 0.6 s, corresponding to LV diastole, and shifts to the left from 0.6 to 0.8 s, corresponding to LV systole. The peak shifting clearly indicates the relaxation and contraction of the cardiac chambers. **b**, The cross-sectional structure of the parasternal short-axis view corresponding to the signal peaks in a.

nature research

Corresponding author(s): Sheng Xu

Last updated by author(s): May 28, 2021

Reporting Summary

Nature Research wishes to improve the reproducibility of the work that we publish. This form provides structure for consistency and transparency in reporting. For further information on Nature Research policies, see our Editorial Policies and the Editorial Policy Checklist.

Statistics

For all statistical analyses, confirm that the following items are present in the figure legend, table legend, main text, or Methods section.

n/a	Confirmed	
☐	☒	The exact sample size (*n*) for each experimental group/condition, given as a discrete number and unit of measurement
☐	☒	A statement on whether measurements were taken from distinct samples or whether the same sample was measured repeatedly
☐	☒	The statistical test(s) used AND whether they are one- or two-sided *Only common tests should be described solely by name; describe more complex techniques in the Methods section.*
☒	☐	A description of all covariates tested
☒	☐	A description of any assumptions or corrections, such as tests of normality and adjustment for multiple comparisons
☐	☒	A full description of the statistical parameters including central tendency (e.g. means) or other basic estimates (e.g. regression coefficient) AND variation (e.g. standard deviation) or associated estimates of uncertainty (e.g. confidence intervals)
☐	☒	For null hypothesis testing, the test statistic (e.g. *F*, *t*, *r*) with confidence intervals, effect sizes, degrees of freedom and *P* value noted *Give P values as exact values whenever suitable.*
☒	☐	For Bayesian analysis, information on the choice of priors and Markov chain Monte Carlo settings
☐	☒	For hierarchical and complex designs, identification of the appropriate level for tests and full reporting of outcomes
☒	☐	Estimates of effect sizes (e.g. Cohen's *d*, Pearson's *r*), indicating how they were calculated

Our web collection on statistics for biologists contains articles on many of the points above.

Software and code

Policy information about availability of computer code

Data collection	Data collection of the ultrasound signal was carrried out with the Verasonics Vantage platform.
Data analysis	Data of the ultrasound signal was analyzed via the Verasonics Vantage and Matlab platform.

For manuscripts utilizing custom algorithms or software that are central to the research but not yet described in published literature, software must be made available to editors and reviewers. We strongly encourage code deposition in a community repository (e.g. GitHub). See the Nature Research guidelines for submitting code & software for further information.

Data

Policy information about availability of data

All manuscripts must include a data availability statement. This statement should provide the following information, where applicable:

- Accession codes, unique identifiers, or web links for publicly available datasets
- A list of figures that have associated raw data
- A description of any restrictions on data availability

The main data supporting the results in this study are available within the paper and its Supplementary Information. Data generated in this study, including source data and the data used to make the figures, are available from Harvard Dataverse via the identifier https://dataverse.harvard.edu/dataset.xhtml?persistentId=doi:10.7910/DVN/EPITIY.

Field-specific reporting

Please select the one below that is the best fit for your research. If you are not sure, read the appropriate sections before making your selection.

☒ Life sciences ☐ Behavioural & social sciences ☐ Ecological, evolutionary & environmental sciences

For a reference copy of the document with all sections, see nature.com/documents/nr-reporting-summary-flat.pdf

Life sciences study design

All studies must disclose on these points even when the disclosure is negative.

Sample size	Three healthy subjects, for proof-of-principle testing.
Data exclusions	No data were excluded.
Replication	All attempts at data replication were successful.
Randomization	Not relevant. Validation testing was carried out as a correlation analysis between the newly developed prototype and a standard tool.
Blinding	Not relevant.

Reporting for specific materials, systems and methods

We require information from authors about some types of materials, experimental systems and methods used in many studies. Here, indicate whether each material, system or method listed is relevant to your study. If you are not sure if a list item applies to your research, read the appropriate section before selecting a response.

Materials & experimental systems

n/a	Involved in the study
☒	☐ Antibodies
☒	☐ Eukaryotic cell lines
☒	☐ Palaeontology and archaeology
☒	☐ Animals and other organisms
☐	☒ Human research participants
☒	☐ Clinical data
☒	☐ Dual use research of concern

Methods

n/a	Involved in the study
☒	☐ ChIP-seq
☒	☐ Flow cytometry
☒	☐ MRI-based neuroimaging

Human research participants

Policy information about studies involving human research participants

Population characteristics	Blood flow was measured on three healthy subjects in a static sitting position.
Recruitment	All human-testing subjects participating in blood flow measurements and skin-curvature characterizations had all agreed to the voluntary consent.
Ethics oversight	All experiments were conducted in accordance with the ethical guidelines of the NIH and with the approval of the Institutional Review Board of the University of California, San Diego (IRB no. 170812).

Note that full information on the approval of the study protocol must also be provided in the manuscript.

nature portfolio

https://doi.org/10.1038/s41551-021-00763-4

Supplementary information

Continuous monitoring of deep-tissue haemodynamics with stretchable ultrasonic phased arrays

In the format provided by the authors and unedited

Content

Supplementary Discussion 1 | Comparison between our work and other representative rigid, flexible ultrasound array work.

As summarized in Table 1, recent work has been focusing on rigid and flexible ultrasound arrays. To realize deep tissue sensing, however, the ideal ultrasonic probe should have several features. First, the elastic mechanical properties of the device should enable seamless contact with the skin to minimize the interfacial reflection and irritation to the skin. Otherwise, any residual gas bubbles at the interface would strongly reflect the ultrasound signals and significantly reduce the SNR. Also, the mechanical mismatch between the flexible device and stretchable skin would constantly irritate the skin, which gradually degrades the interfacial contact and, therefore, the measurement results. Second, a low center frequency could allow for sufficient axial resolution, high tolerance to phase aberration induced by the geometry deformation, and high penetration in deep tissues. More than 6 cm penetration is required in order to access central organs such as the heart, lung, intestine et al. (Extended Data Fig. 1). Third, the phased array allows for beam focusing and steering for active targeting of tissues of interest. Considering those requirements, the existing devices lack one or more of those aspects and thus are not best suitable for biomedical applications, as demonstrated in this work. With the stretchable form factor, sufficient resolution, high tolerance to phased aberration, deep penetration, and the phased array control, the device reported here offers the most competitive advantages for deep tissue monitoring.

Wearable ultrasound probes	Pietrangelo et al, 2018[1]	Song et al, 2019[2]	Pashaei et al, 2020[3]	Bhuyan et al, 2011[4]	Hu et al, 2018[5]	Wang et al, 2018[6]	This work
Mechanical property	Rigid	Rigid	Flexible	Flexible	Stretchable	Stretchable	Stretchable
Frequency (MHz)	2	2.5	5	5	3.5	7.5	2
Penetration depth (cm) and media	N/A	N/A	2 cm (in tissue)	5 (in tissue mimicking gel)	7 (in aluminum)	4 (in tissue)	14 (in tissue)
Axial resolution (mm)	N/A	N/A	0.3	N/A	0.61	0.5	2.5
Pitch (mm^2)	1.6 x 1.6	Single transducer	0.2	0.3 (linear)	2.0 x 2.0	2.5 x 2.0	0.8 x 0.8
Phased array	Yes	No	Yes	Yes	No	No	Yes
Human testing	No	Yes	Yes	Yes	No	Yes	Yes

Table 1. Comparison on mechanical property, frequency, penetration, resolution, phased array control, and biomedical applications between this work and existing state-of-the-art.

Comparing with the work we published for imaging the defects using stretchable ultrasound array in inorganic material[5], the main focus of this work is to develop an active targeting and highly penetrating wearable sensor for monitoring deep tissue physiological signals. There are distinctions from previous work on the following three aspects. Firstly, the technologies are different. The phased array technique, by definition, is to vary the timing of each individual element for ultrasonic pattern control. By changing the progressive time delay of activating the elements, the synthesized beam can be focused and steered electronically. The beam can be swept like a searchlight through the tissue or object being examined. To our best knowledge, this type of active scanning and targeted sensing has never been realized by any wearable conformal sensors in the literature. In our previous work, each element works in a sequential and individual manner, which emits ultrasound pulses in a fixed direction. Therefore, it does not have active scanning or targeting capabilities to search a wide area inside the human body.

Secondly, the use cases are different. The previous work demonstrated the seamless integration with static civil infrastructures, especially specimens with curved surfaces, which was for structural health monitoring in civil engineering. The imaging on the human body demonstrated in this work is qualitatively different and more challenging than imaging on static civil infrastructures, e.g., an aluminum block. The phase/physical location of each element on the aluminum block can be precisely calculated. However, the human skin surface is dynamic, with different and unknown skin curvature at any given time.

Thirdly, we study the phase tolerance of ultrasonic devices on the human body, not on non-biological tissue, as in our previous effort. Conventionally, the phased array was believed impossible on the highly curved and dynamic human skin surface, because the associated phase correction required to compensate

for the unknown element positions was not available. In this work, we have studied in detail the parameters of the ultrasound phased array under various scenarios. We eventually concluded that it was possible to realize the phased array on the human body, even without prior knowledge of the element positions and the corresponding phased correction. Without the phase correction, the signal quality we could collect has proven to be sufficient to generate meaningful and valuable data in this study.

In all, we demonstrate in this work, for the first time, the phased array technique can be integrated with wearable conformal sensors. This kind of sensing approach using a focused and tunable ultrasound beam enables active scanning and targeting in 3D inside the human body, which opens up tremendous opportunities in continuous and noninvasive recordings of deep tissues and central organs.

Supplementary Discussion 2 | Comparison between our work and other representative electromagnetic phased array work.

The paper Agrawal, D. R. et al. demonstrated flexible fixed phased device for wireless powering application[7]. Specifically, the device has four emitters to form spatially controlled rough beamforming to powering tissue integrated devices. However, in that work, the device has an axial resolution of 3.6 cm and a penetration of 4.5 cm. Considering the characteristics including resolution, penetration, and beam pattern controlling, the former work only did a rough demonstration but far from reaching application in deep tissue organs.

Different from wireless powering, our application is for continuous sensing purposes whose spatial resolution is targeted for hundreds of micrometers, which is beyond the capability of other phased array prototypes, including the former work. To fill this technical gap, we need to accurately control the beam width and shape to target a specific organ of interest. This leads to the fundamental difference in technology development. We have to individually program a larger amount of array 36 than the four fixed phased elements as shown in the previous work to realize higher directivity and resolution, which can satisfy the need of sensing various biological signals in the deep tissue with high precision.

Supplementary Discussion 3 | Calculation of the electromechanical coupling factor.

The thickness mode coupling coefficient of a single element can be calculated by[8]:

$$k_t = \sqrt{\frac{\pi}{2}\frac{f_r}{f_a}\tan\left(\frac{\pi}{2}\frac{f_a - f_r}{f_a}\right)}$$

where f_r is the resonance frequency, and f_a is the anti-resonance frequency.

Supplementary Discussion 4 | Acoustic intensity measurement, calculation, and safety considerations.

1.1 Spatial-peak pulse-average ultrasonic intensity

We have confirmed the acoustic intensity of the stretchable phased array patch by hydrophone measurement, which is 0.47 W/ cm^2. In the experiment, we use a hydrophone moved by a 3D linear motor to measure the signal in the focusing region of our phased array, which is the highest intensity region in the acoustic field. The peak signal strength V_{output} is 30 mV. Our system has 20 dB in pre-amplifier, and the hydrophone sensitivity is -272 dB re. 1 V/μPa = 2.512e-8 V/Pa at 2 MHz frequency.

By converting the pre-amplifier gain, the signal before the amplifier is 0.003 V. Therefore, the acoustic pressure.

$$P_0 = \frac{0.003\ V}{\left(2.512^{-8} V/Pa\right)} = 0.12\ MPa$$

The acoustic intensity can be calculated by:

$$I_{sppa} = \frac{P_0^2}{2 \cdot \rho \cdot c} = \frac{120000^2}{(2 \times 1 \times 1540)} = 0.47\ W/cm^2$$

The result is close to the acoustic intensity of a standard ultrasound imaging device (GE Voluson S6, GE Medical Systems, Gyeonggi-do, South Korea) reported by literature[9].

Considering the bio-effects of ultrasonic waves, the U.S. Food and Drug Administration (FDA) regulates the spatial-peak temporal-average intensity ($I_{SPPA.3}$) of medical ultrasonic devices[10]. However, the intensity of the ultrasonic output can only be measured by a hydrophone in the water, rather than real tissues, which creates disparities due to the property difference between the water and tissues. Results from *in vitro* characterizations can't represent the actual intensity in the real tissue. Considering the frequency-dependent attenuation effect of human tissues, the derated spatial-peak temporal-average ultrasonic intensity $I_{SPTA.3}$ is adopted to understand the ultrasonic intensity of the stretchable phased array in this study[11].

1.2 Derated spatial-peak pulse-average ultrasonic intensity $I_{SPPA.3}$

The FDA imposes several application-specific exposure limits, including limits for peripheral vascular (190 W/cm^2), cardiac (central, 190 W/cm^2), fetal (190 W/cm^2), and ophthalmic (17 W/cm^2) ultrasonics[12]. Based on the derating principles, after converting the intensity in water to the intensity in human tissues, the derated $I_{SPTA.3}$ of the stretchable phased array is 0.47 W/cm^2. Considering our applications including cardiac Doppler and vascular hemodynamics, the intensity level of the stretchable phased array is lower than the FDA-allowed intensity for medical applications. If we aim for other applications such as ophthalmic or fetal monitoring that have a lower allowable intensity level, the ultrasonic intensity can be tuned down by lowering the activation voltage and reducing the number of elements.

1.3 The driving voltage of the stretchable phased array and safety evaluation

The peak excitation voltage of the stretchable phased array usually ranges from 100 to 200 V. However, this device will not cause any harm to the subjects who need continuous monitoring. The electrical hazard is determined by a combination of the peak voltage and the duration of the peak current, in a way that neither of the factors alone can injure human tissues[13]. To explain this further, a contact voltage (e.g., 200 V, the maximum voltage adopted by the stretchable phased array) can either produce severe injury or a benevolent effect, depending on the duration of the current flow. With direct contact to a 200 V continuous voltage source, considering the situation of the smallest resistance (in a moisturized environment), the current endurance duration must be shorter than 40 ms[14]. However, the voltage source is in a pulsed transduction mode in this study. Specifically, the element is vibrating in a repetitive and transient manner. The repetitive behavior of the stretchable phased array, decided by its pulse-repetitive-frequency (PRF), is 5 kHz, which means the element has 5 thousand working cycles in one second. The transient working state of the device implies that the sensor, in each working cycle, will experience an ultra-short (0.5 μs, determined by the center frequency of the device, 2 MHz) stimulation period with a 200 V peak-to-peak voltage. This transient process, which happens in merely 2.5 ms (determined by the center frequency of the device, 2 MHz), is far below the allowable human tolerance of 40 ms. In the pulsed excitation scheme, during 99.7% of the time, no voltage is applied to the element, and thus no current will flow across the human body. Therefore, the stretchable phased array, even in case of a leakage, will not harm the subject. In fact, the stretchable phased array is fully encapsulated by Ecoflex silicone, which is a superb insulator. Therefore, the stretchable phased array is safe for the human body.

Supplementary Discussion 5 | Axial and lateral resolution considerations of the stretchable phased array.

The axial resolutions of the stretchable phased array at different depths in the human tissue are listed in the following table 2. The detailed testing protocol is described in the Materials and Methods section.

Depth (cm)	Resolution (mm)
5	2.5
10	2.7
20	2.6
30	2.7

Table 2. The axial resolutions of the stretchable phased array at different depths

Another point we need to mention is the lateral resolution, which depends on the array pitch and the aperture size. A smaller pitch will increase the lateral resolution but will sacrifice the mechanical compliance and stretchability of the device. The aperture size is a critical factor for the focusing sharpness and thus the lateral resolution of ultrasound devices. A larger aperture has a sharper focus and thus a higher lateral resolution because the focus comes from the accumulated contributions of each individual element. Therefore, a larger aperture of the array is good for increasing the lateral resolution, especially for imaging applications. For developing the wearable patch, a 12x12 array is a minimal size to achieve the sensing applications in this work. On the other hand, we need to keep the array size small to minimize the overall power budget of the device. Therefore, we did not choose a larger array size. It is worth mentioning that minimizing the aperture size has a higher impact on low-frequency devices because low-frequency transducers have lower attenuation than high-frequency transducers. Additionally, lower frequency transducers have larger beam spreading characteristics (as shown by results in Supplementary Figs 5, 6, and 7), which means the marginal transducers of a low frequency still have large influences on the focusing center. Considering the focusing effect is the spatial superposition of all elements' contribution, the reduced aperture size (i.e., the reduced number of elements) has a larger impact on the sharpness of focusing for lower frequency devices. To potentially solve this problem, when there is a need for better focusing in the future, we can enlarge the array size by adding more elements. Adopting elements with a smaller footprint, such as micromachined ultrasound elements, to decrease the element pitch can also greatly enhance the focusing of the device.

Supplementary Discussion 6 | Advantages of narrowband signals over broadband signals in Doppler applications.

Because the Doppler signal processing requires the extraction of Doppler shift in the frequency domain, extractions from sharper peaks in the ultrasonic signal are easier and more accurate. Compared to broadband signals, the narrowband signals induced by long pulse excitations have a sharper profile in the frequency domain and are, therefore, more desirable for Doppler applications. We adopt the long pulse excitation mode for cardiac tissue Doppler and blood flow spectrum recording in this work.

We acknowledge long pulse excitation will decrease the axial resolution of the detection. Since the major focus of the application is for velocity interrogation, the adoption of multiple pulses to guarantee detection accuracy is required. In future work related to non-Doppler applications such as B-mode imaging, we will explore short pulse excitation to balance and optimize both resolution and the SNR.

Supplementary Discussion 7 | Specular reflection, scattering, and their relationship to ultrasonic device parameters and operational considerations.

There are two kinds of reflection modes in ultrasonic diagnosis: specular reflection and scattering. The former is often used for sensing interfaces, where the object or the interface scale is much larger than the ultrasonic wavelength (Supplementary Fig. 22a). The SNR is high and is related to the ultrasonic impedance difference between two tissue layers at the interface. The latter happens when using ultrasonic waves to sense small objects with sizes around or smaller than the ultrasonic wavelength, such as red blood cells (~8 μm in size) (Supplementary Fig. 22b). In this situation, the ultrasonic scattering intensity P_s is expressed as the following equation[15]:

$$P_s = \frac{P_t A_r^2 e^{-4\alpha_m^R} \eta S}{8T\lambda^2 R^4 {\alpha_1}^2 c}\left(e^{2ct_1\alpha_1} - e^{-2ct_2\alpha_1}\right)\left(e^{\tau c\alpha_1} - e^{-\tau c\alpha_1}\right)$$

where P_t is the ultrasonic power transmitted by the device, A_r is the effective receiving aperture of the device, α_m is the ultrasonic attenuation coefficient in the medium outside the lumen, R is the propagation distance of the ultrasonic wave, η is the backscattering coefficient, S is the cross-section of the ultrasonic beam, T is the burst period, λ is the ultrasonic wavelength in the tissue, α_1 is the ultrasonic attenuation constant in the lumen region, c is the ultrasonic propagation velocity in the tissue, t_1 is the travel time of the ultrasonic wave from the skin to the vessel's anterior-wall, t_2 is the traveling time of the ultrasonic wave from

the skin to the vessel's posterior-wall, and τ is the pulse width[15]. Based on the equation, there are several device parameters we can tune to maximize the received intensity. For example, the received signal intensity can be enhanced by decreasing the ultrasonic wavelength, elongating the pulse width with multi-pulse excitation, as demonstrated in Supplementary Figs. 12 and 13, and enhancing the transmitted ultrasonic power by raising the activation voltage and increasing the number of elements in the array.

Supplementary Discussion 8 | Propagation distance aberration of each element induced by the skin curvature.

When the positions of the phased array elements shift, the propagation distance of the wavefront from each element to a certain point in the 3D space will change, leading to phase distance aberrations. The following table 3 lists the theoretical calculation of the propagation distance aberration induced by curved skin (with a 4.2 cm curvature radius) of each element in the array, as well as their proportion to the ultrasonic wavelength (770 μm). We can see that the largest aberrations take place at the elements on the edge of the array, and the value gradually decreases as we move closer to the center of the array. The six elements near the center (corresponding to channels 4~9) have propagation distance changes lower than 10%. We conclude that the propagation distance change induced by the array deformation has minimal impact on the beamforming for the frequency used in this study.

Channel	1	2	3	4	5	6	7	8	9	10	11	12
Distance distortion (μm)	204.8	137.8	83.9	43.1	15.5	1.7	1.7	15.8	44.5	87.7	145.9	218.6
Percentage (%) of λ	26.6	17.9	10.9	5.6	2.02	0.23	0.23	2.1	5.8	11.4	18.9	28.4

Table 3. Theoretical calculation of the propagation distortion of each element induced by a surface (4.2 cm curvature radius) and relative percentage compared to the ultrasonic wavelength

Supplementary Discussion 9 | Frequency adoption consideration based on the SNR and skin curvature tolerance.

Given the same acoustic intensity level, although higher frequency devices have better SNR, frequencies that are too high will affect the curvature tolerance of phased array beamforming. Higher frequency ultrasonic waves are more sensitive to position shifts of the phased array elements as the wavefronts are less likely to have ultrasonic superposition with each other. Instead, they have a larger probability of canceling out each other due to phase aberration. Considering both the SNR we need and the tolerance to phase aberrations on the human neck, we choose a 2 MHz center frequency in this study. The recording results we demonstrate in Figs. 3 and 4 of central blood flow and cardiac tissue signal proved our selection.

Supplementary Discussion 10 | Carotid output measurements.

The carotid output was repeated on the same subject for three times. The test involved the simultaneous recording of the carotid blood flow (CBF) and the blood vessel distension. The CBF was recorded by a 12 x 12 phased array probe with a frequency of 2 MHz. The vessel diameter was recorded by a 4 x 5 unfocused stretchable ultrasonic patch (7.5 MHz, with a size of 1.5 cm x 1 cm)[4].

The CBF can be derived from multiplying the vessel cross-section, the average carotid flow velocity, and the heart rate (HR):

$$CBF = \frac{\pi \times d^2}{4} \times VTI \times HR$$

where *d* is the carotid diameter, *VTI* is the velocity-time integral, and *HR* is calculated from the periodic blood flow spectrum signal. The measurements were done every 5 minutes over a 30-minute period, with each recording period being 20 s. The average flow velocity and diameter were calculated to estimate the carotid output at a given time point.

Supplementary Figures

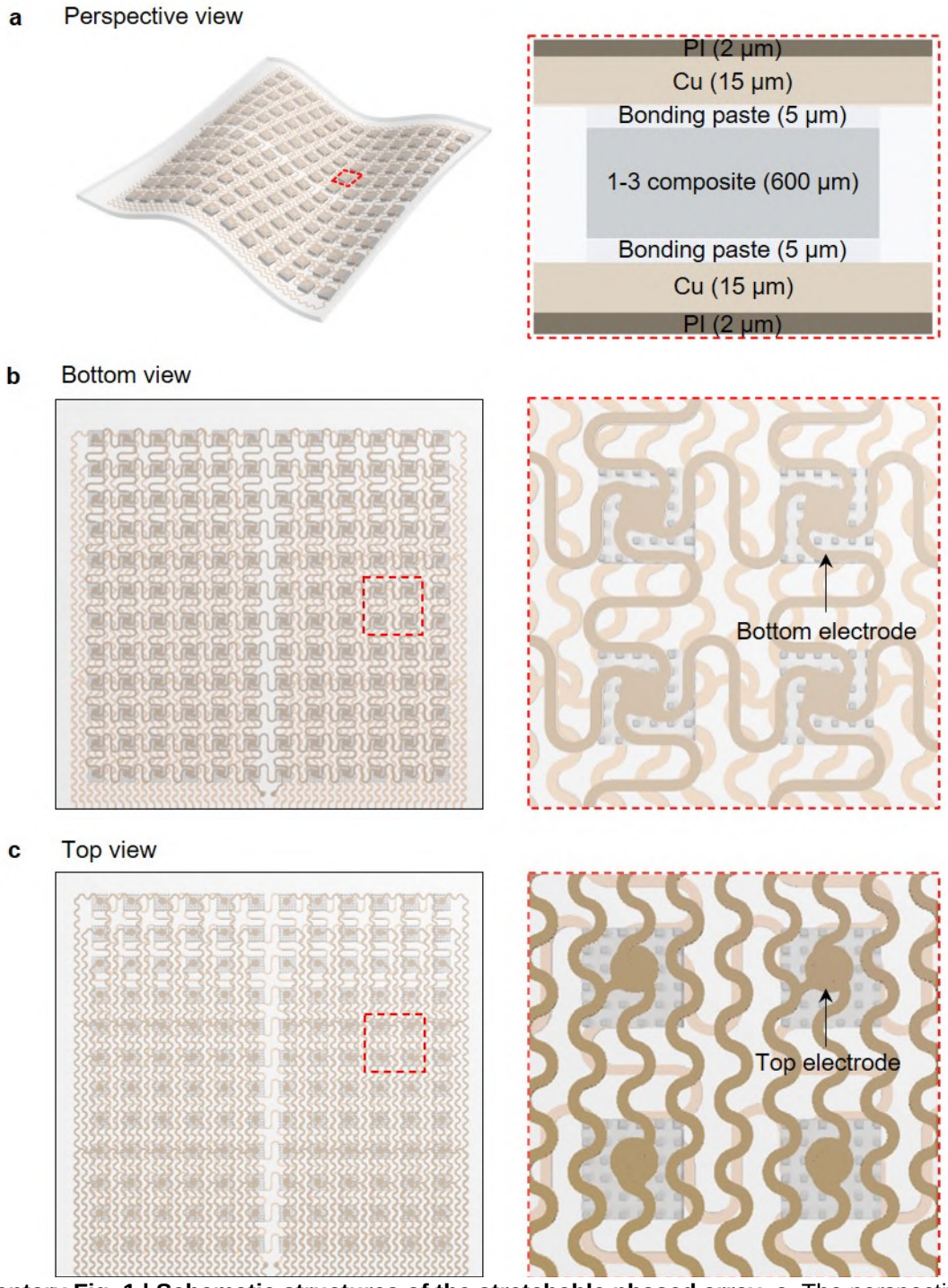

Supplementary Fig. 1 | Schematic structures of the stretchable phased array. a, The perspective view of the device. The inset shows the cross-section of a single element. The material layers and thicknesses are labeled. **b**, The bottom view of the device (left panel), and a zoomed-in image of a 2 x 2 array highlighting the bottom electrode design (right panel). **c**, The top view of the device (left panel), and a zoomed-in image of a 2 x 2 array highlighting the top electrode design (right panel).

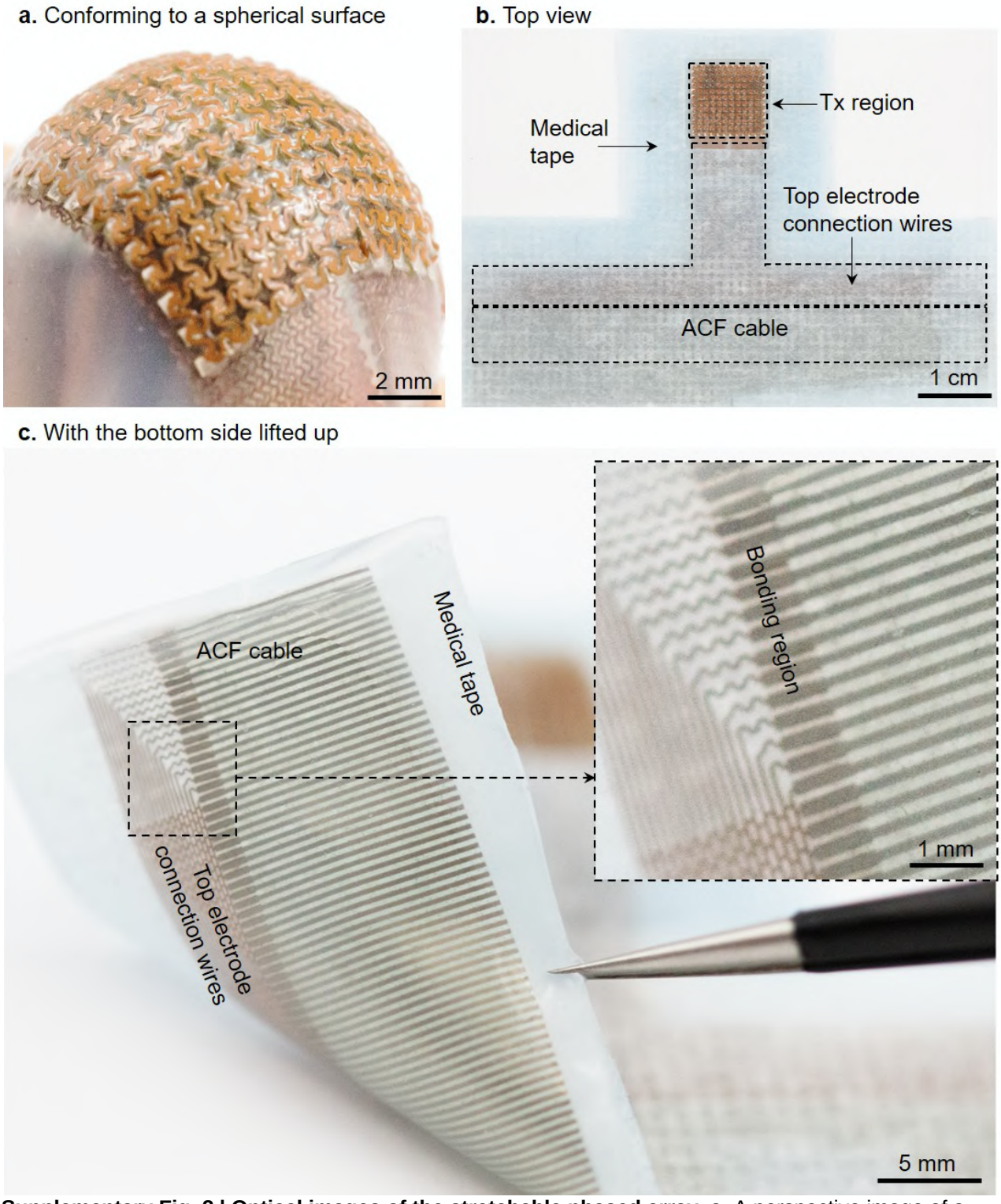

Supplementary Fig. 2 | Optical images of the stretchable phased array. a, A perspective image of a stretchable phased array on a spherical surface, showing its flexibility and stretchability. **b**, A top view of the entire device, containing the back-end connection with an anisotropic conductive film (ACF) cable, as labeled in the image. The device is covered with medical tape to facilitate adhesion to the skin. **c**, An image of the backside of the stretchable phased array in **b** showing the connection wires and the ACF cable.

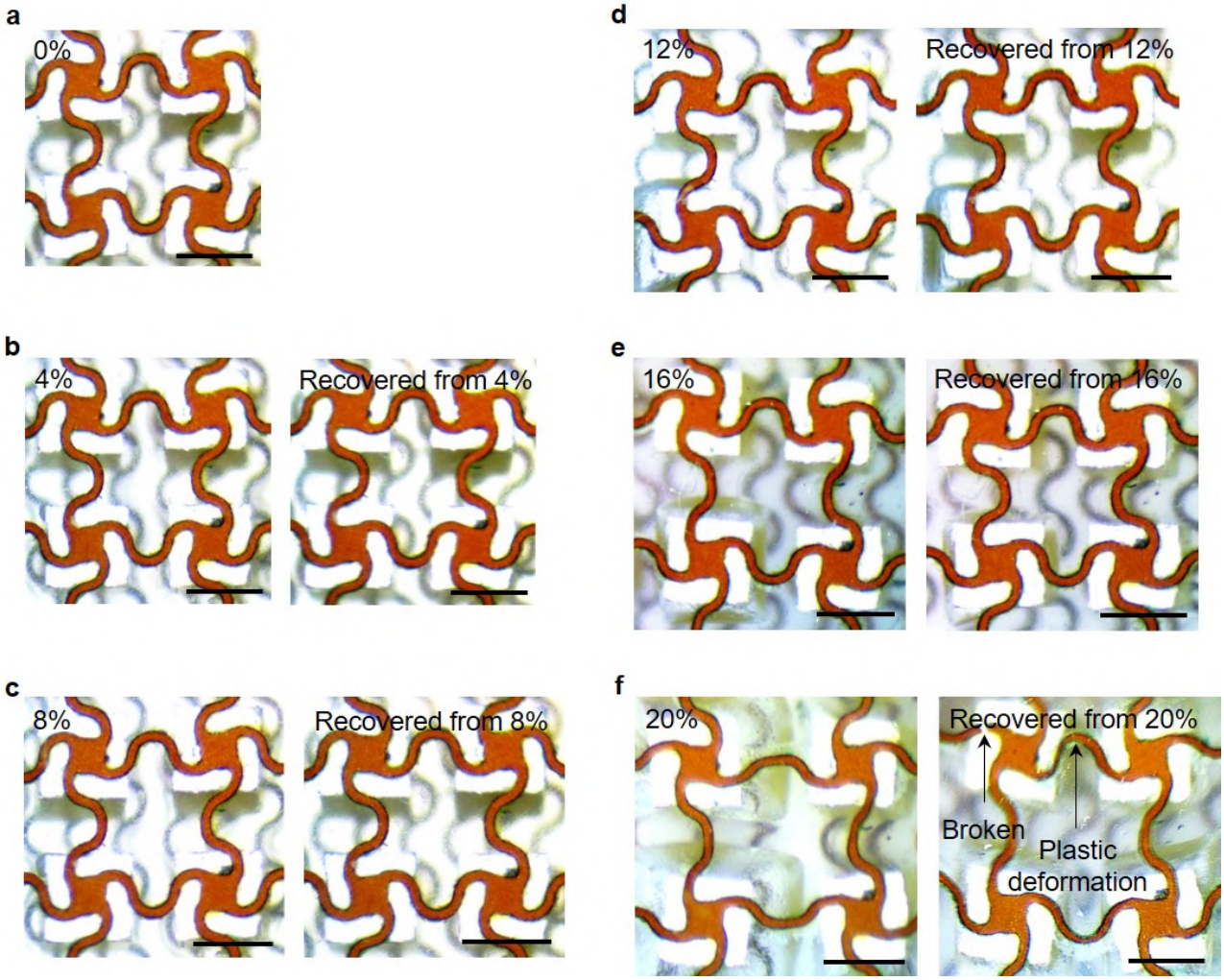

Supplementary Fig. 3 | Optical images of the stretchable phased array during the stretchability test. **a**, The device in its original state with 0% strain. **b**, The device under 4% biaxial tensile strain (left) and after recovery to a strain-free state (right). **c**, The device under 8% biaxial tensile strain (left) and after recovery to a strain-free state (right). **d**, The device under 12% biaxial tensile strain (left) and after recovery to a strain-free state (right). **e**, The device under 16% biaxial tensile strain (left) and after recovery to a strain-free state (right). The results show the device can withstand biaxial strain up to 16% without plastic deformation. **f**, The device under 20% biaxial tensile strain (left) and after recovery to a strain-free state, where plastic deformation and fracture are identified (right). Scale bars are all 0.5 mm.

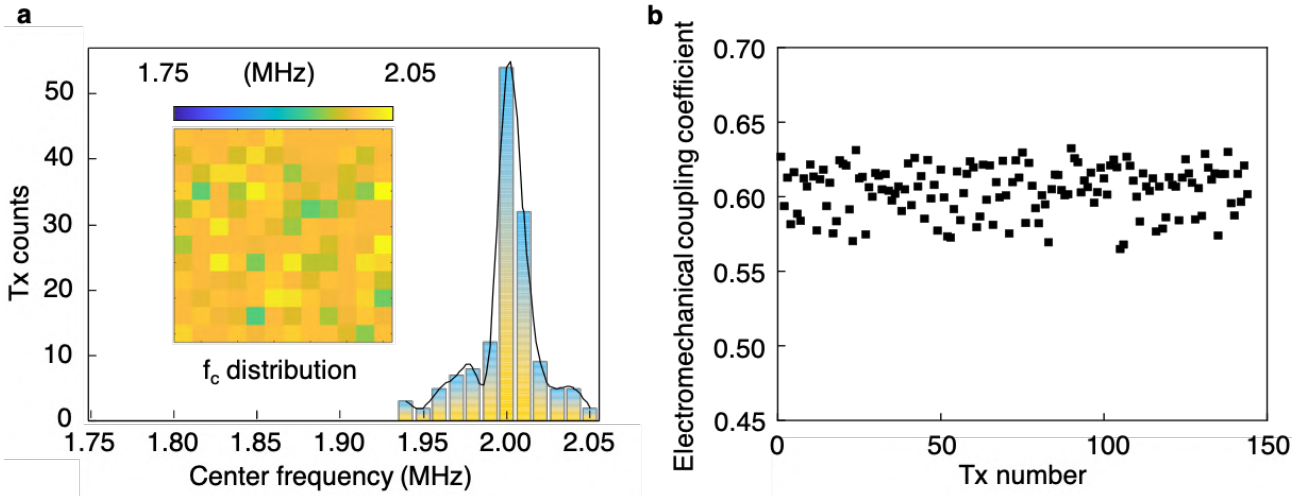

Supplementary Fig. 4 | Characterizations of the transducer (Tx) element property distribution in the stretchable phased array. a, Center frequency (f_c) and **b,** electromechanical coupling coefficient (K_t) distribution of the 144 elements in the array, showing the consistency of element properties and the reliability of the array fabrication process.

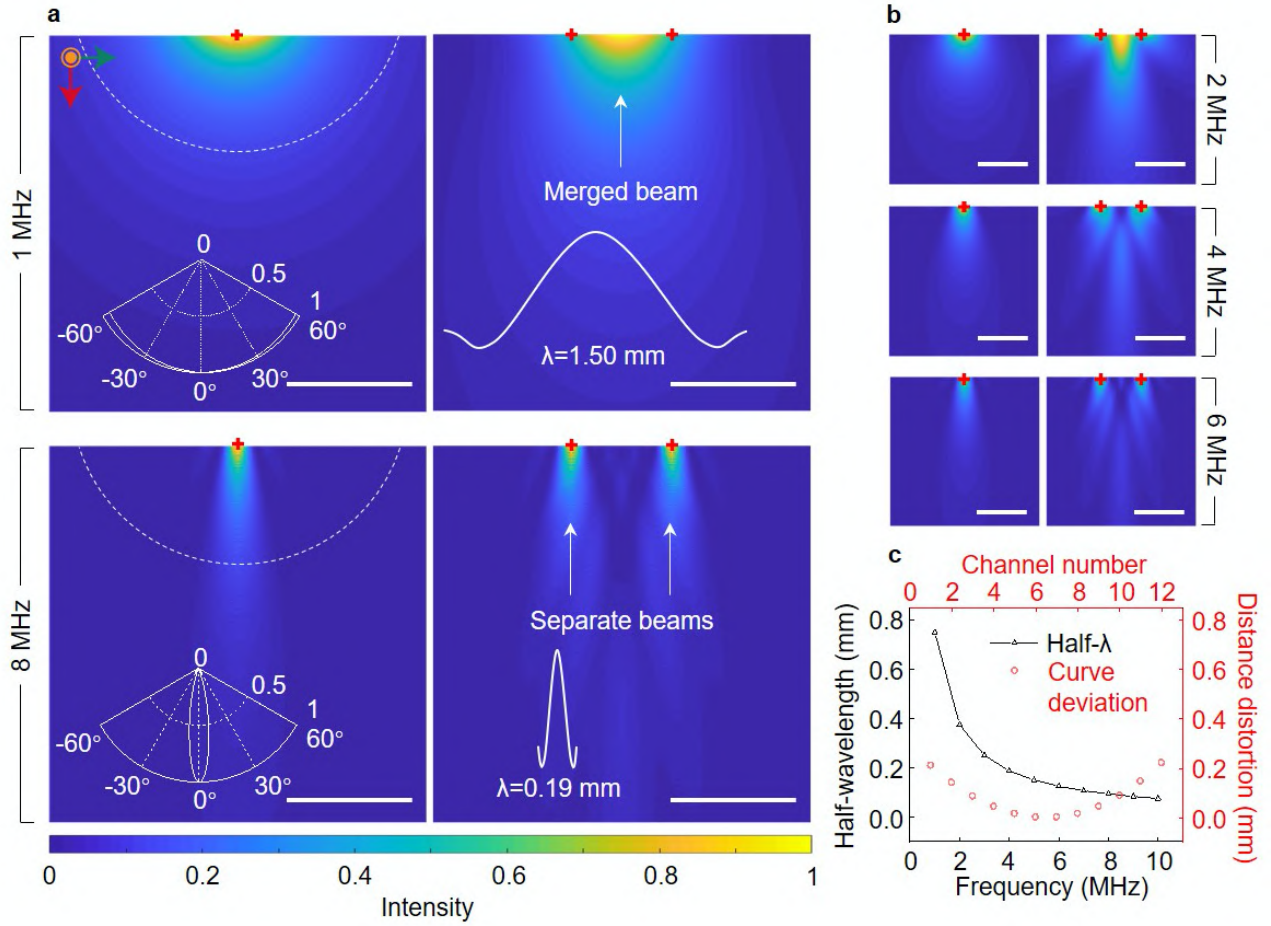

Supplementary Fig. 5 | Field II simulation of the beam convergence and deformation tolerance of phased array beamforming at various frequencies. a, Comparison between the ultrasonic fields of a single (left) and two (right) transducers in the x-z plane at 1 MHz (top panels) and 8 MHz (bottom panels). Insets in the left panels show the ultrasonic beam patterns extracted along the dashed circle. The left panels show that at 1 MHz, the single element has a large beam-spread, and at 8 MHz, the transducer produces a beam with high directivity. The right panels show the interference patterns of the ultrasonic beam generated by two transducers, with a convergent beam at 1 MHz, and two separate beams at 8 MHz. The comparison illustrates that beams with a large spread will have better convergence. Insets in the right panels show the pulse signals of corresponding frequencies. Scale bars, 1 mm. **b**, Ultrasonic fields of a single (left) and two (right) transducers at 2 MHz, 4 MHz, and 6 MHz, respectively. Scale bars, 1 mm. Locations of the transducers in **a** and **b** are labeled with red crosses. **c**, Phase deviation of each element in a 12-element linear array (numbered 1~12 according to their sequence in the array) upon deformation as compared to the half-wavelength at various frequencies. The black curve shows the half-wavelength at various frequencies. The pink dots show the phase deviation of the transducer array under a 4.2 cm curvature radius. Due to a large wavelength, the low-frequency transducers can tolerate more curved surface-induced distortions. Therefore, it is more suitable for the stretchable phased array. The data in **a** and **b** are simulated using Field II, MATLAB (MathWorks, Natick, MA). The data in **c** is derived from **a** and **b**.

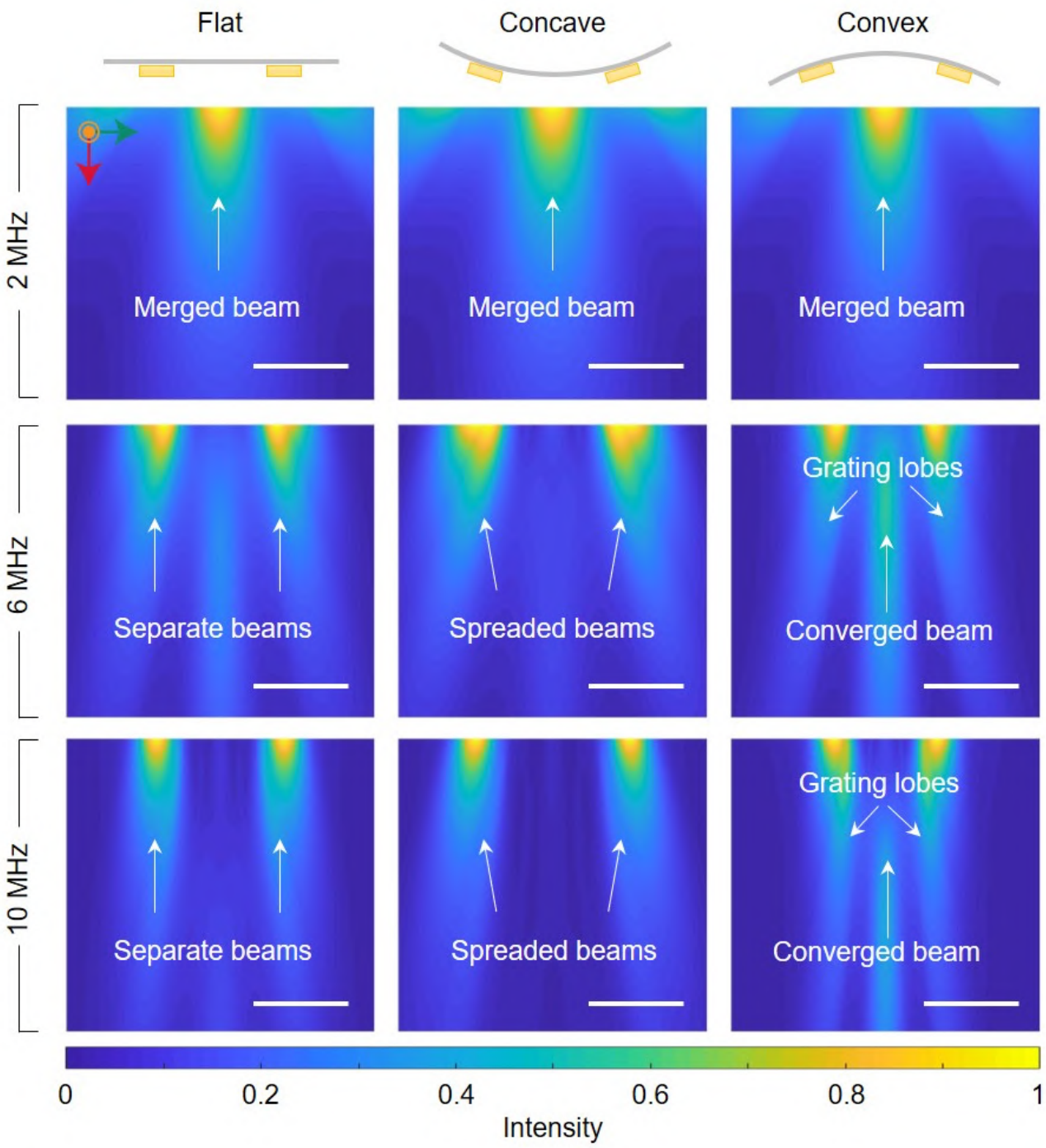

Supplementary Fig. 6 | Field II simulation of the beam convergence in the x-z plane at different frequencies in various bending scenarios. The bending radius of curvature is 4.2 cm. All simulation results in the panels are for beams produced by two transducers with a 0.6x0.6 mm^2 footprint and a 1 mm pitch. A comparison of the results in the same bending scenario at different frequencies shows that the beams can easily merge at a low frequency, regardless of surface bending. At higher frequencies, flat and convex surfaces can easily lead to beam spreading. Although the convex surface can lead to beam convergence at higher frequencies to a certain extent, grating lobes will appear. Therefore, a phased array transducer with a low frequency such as 2 MHz has a high tolerance for array deformations, which is why low frequencies are preferred for building the stretchable phased array. Scale bars are 1 mm. All data are derived by Field II, MATLAB (MathWorks, Natick, MA).

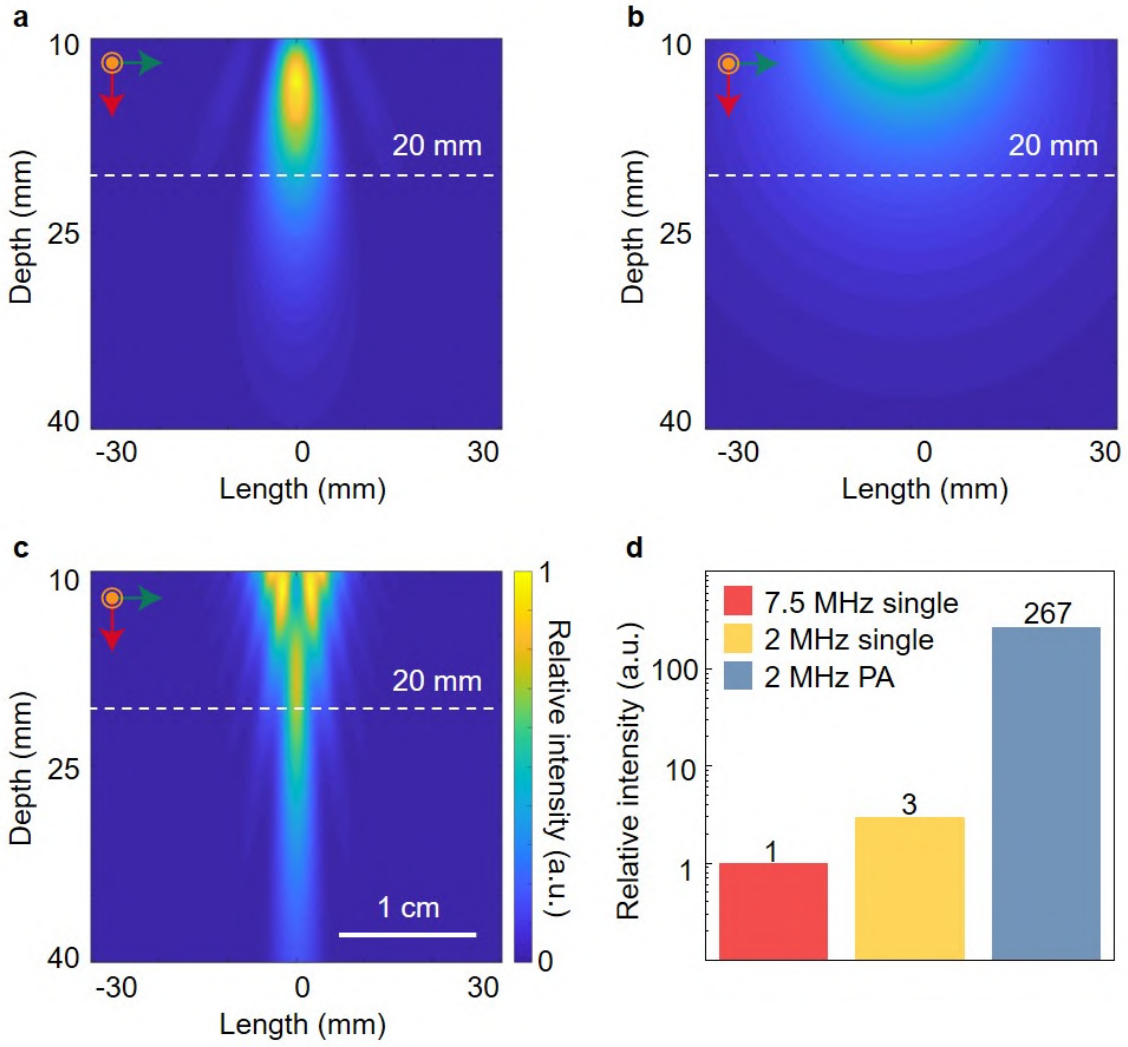

Supplementary Fig. 7 | Field II simulation of the beam produced by a single element and phased array transducers in the x-z plane. Simulated intensity profile of **a**, a 7.5 MHz, 0.9 x 0.9 mm^2 single element, **b**, a 2 MHz, 0.6 x 0.6 mm^2 single element, and **c,** a 2 MHz, 0.6 x 0.6 mm^2, 1 x 12 phased array. All intensity profiles are normalized individually and share the same scale bar on relative intensity. **d**, Normalized intensity comparison at 20 mm depth. The reason we chose 20 mm as the target depth is that the carotid artery depth is typically around 20 mm underneath the skin. All data are derived by Field II, MATLAB (MathWorks, Natick, MA). Signal attenuation has been taken into consideration in the simulation. Panel a, b, and c share the same color bar and are individually normalized.

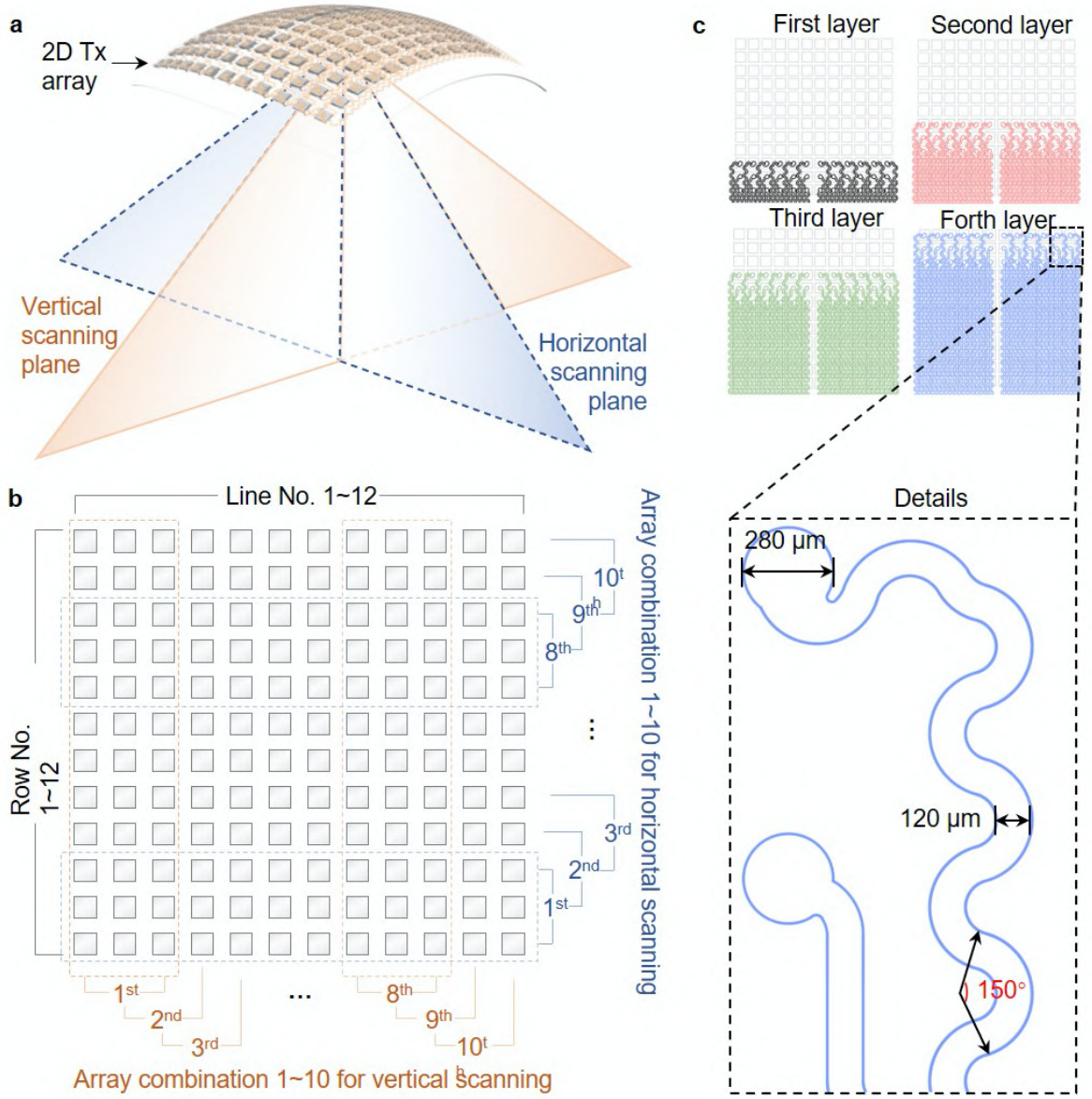

Supplementary Fig. 8 | Activation scheme, multilayer scheme, and circuit details of a 2D phased array. a, The overall device contains 144 individually addressable phased array transducer (Tx) elements (12 lines and 12 rows) in total. The scanning planes of the array can be in both horizontal (blue shade) and vertical (orange shade) directions by phased array beamforming. **b**, The 12 rows of elements are composed of 10-array combinations (in orange/blue dashed boxes) for vertical/horizontal scanning. For example, the 1st horizontal scanning combination involves the 1st, 2nd, and 3rd rows of the array matrix. Each subsequent combination is composed of three adjacent rows of elements sharing the same focal law to enhance the ultrasonic intensity and uniformity. During device operation, the 10 combinations of array elements can produce an ultrasonic beam that scans across the vertical or horizontal plane, enlarging the insonation area to cover the organs of interest. **c**, The multilayered electrode design for the ultrasonic phased array patch. Specific parameters are labeled, including the electrode size, linewidth, and angle of the serpentine interconnect.

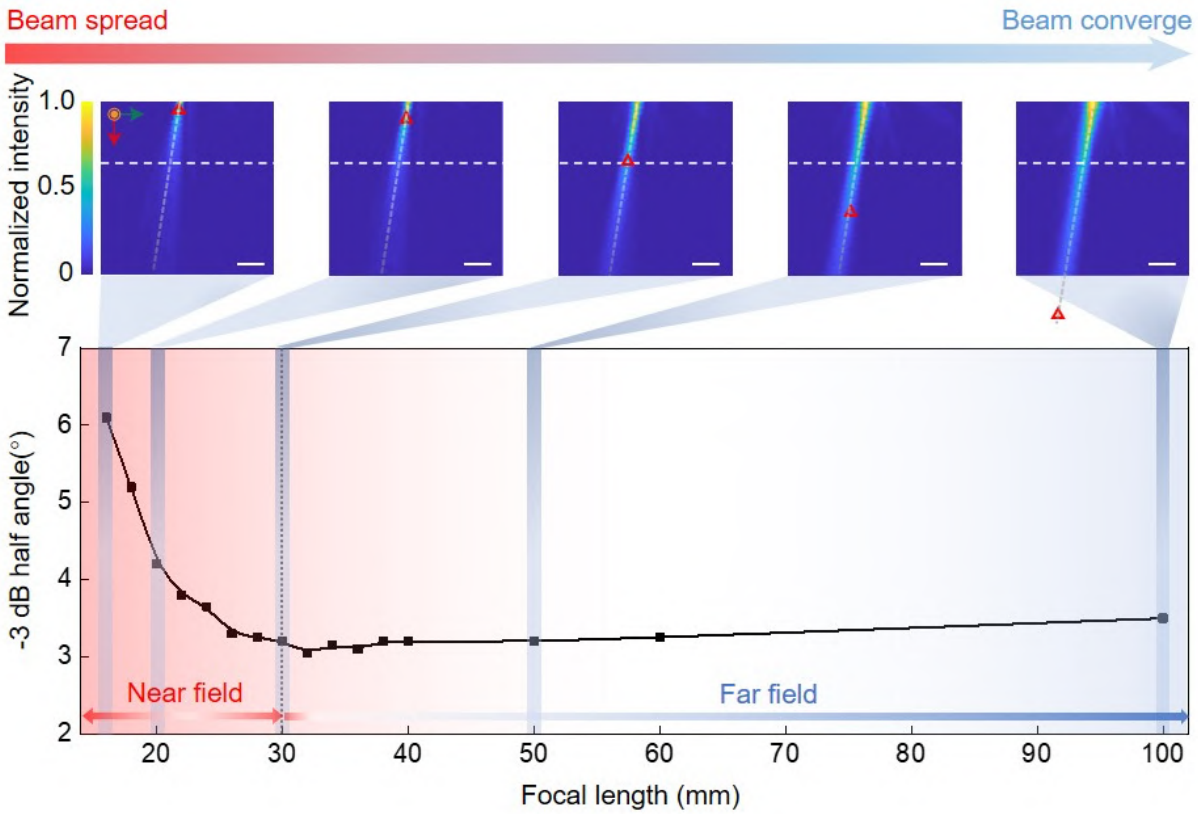

Supplementary Fig. 9 | Variation of the beam directivity with the focal length. From left to right, the top 5 images are representative ultrasonic fields generated by the stretchable phased array with a focal length of 16 mm, 20 mm, 30 mm, 50 mm, and 100 mm, respectively. The results show that a longer focal length leads to a higher beam directivity. The focal points are labeled with red triangles. Scale bars are 1 cm. The bottom chart characterizes the variation of beam directivity with the focal length from 16 mm to 100 mm. When the focal length increases from 16 mm to 30 mm, the directivity increases. Further increase in the focal length up to 100 mm does not affect the beam directivity significantly. All ultrasonic field data are mapped in the x-z plane using an Ultrasonic Intensity Measurement System (Onda, Sunnyvale, CA).

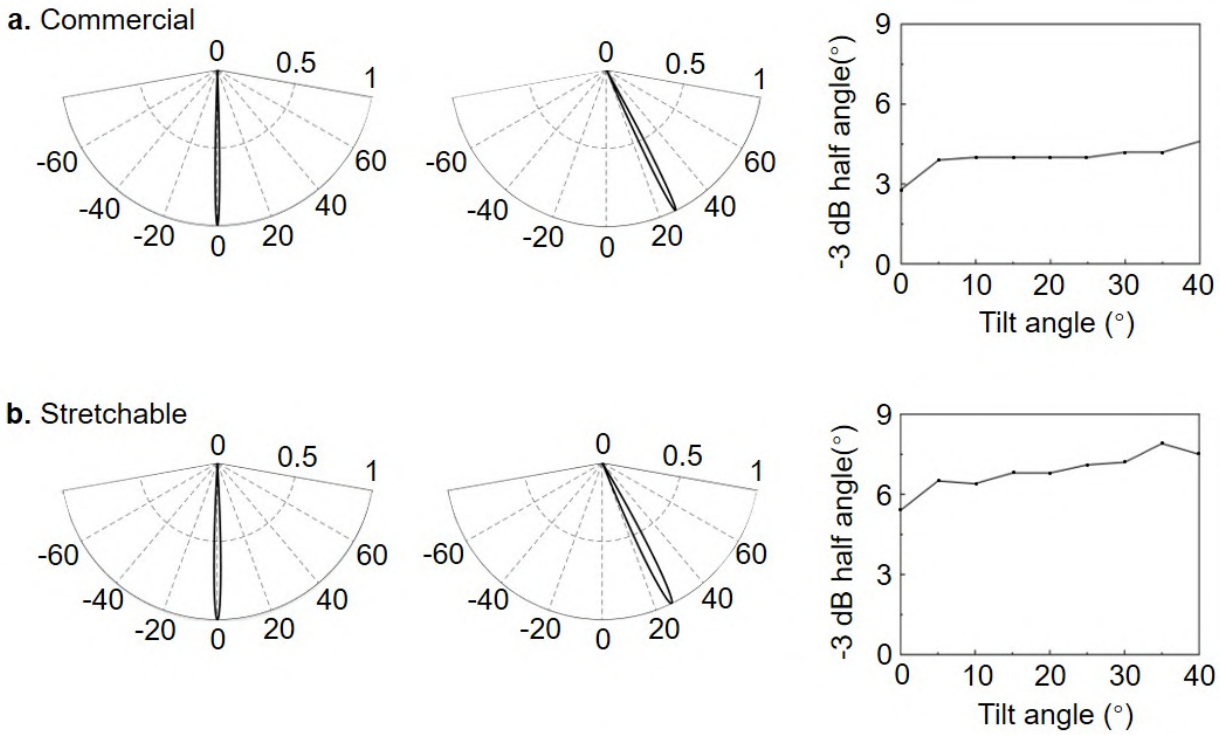

Supplementary Fig. 10 | Beam directivity comparison in the x-z plane between a commercial medical phased array and the stretchable phased array by Field II simulation, MATLAB (MathWorks, Natick, MA). a, Beam patterns of a medical 2 MHz phased array (Verasonics P4-2v probe) at 0° (left panel) and 25° (middle panel), and a summary of the beam directivity at various incidence angles (from 0° to 40°) (right panel). **b**, Beam patterns of the stretchable phased array on a curved surface (with a 4.2 cm radius of curvature) at 0° (left panel) and 25° (right panel), and summary of the beam directivity at various incidence angles (from 0° to 40°) (right panel).

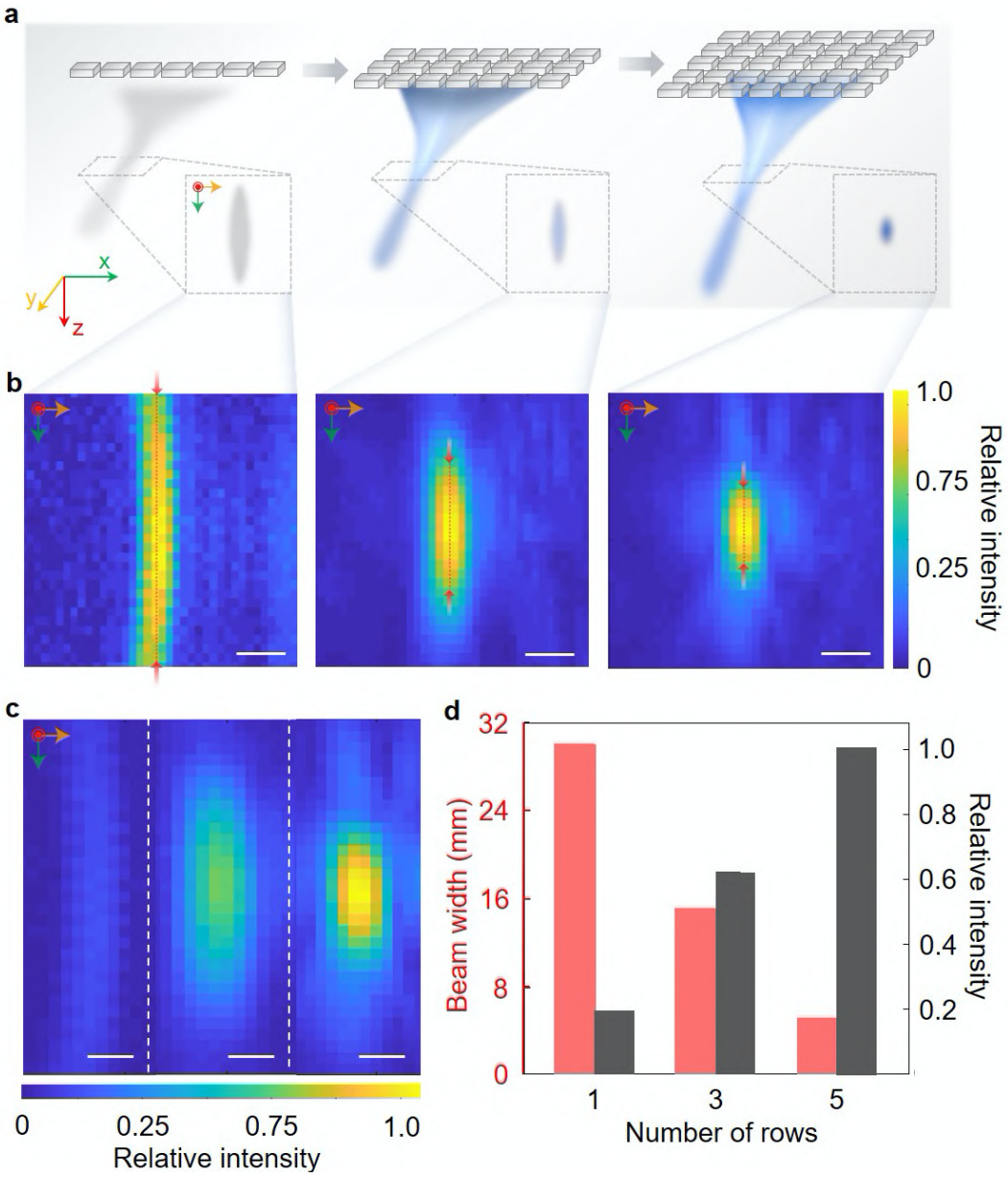

Supplementary Fig. 11 | Enhancement of orthogonal beam convergence in the x-y plane by increasing the number of rows of the phased array. a, Schematic images of the phased array with 1, 3, and 5 rows, with ultrasonic beams focusing at the same point. The insets are illustrations of the beam cross-sections in the x-y focal plane, corresponding to mapping locations in **b**. **b**, Normalized ultrasonic mapping results of beam intensity distributions in the x-y focal plane corresponding to the scenarios in **a**, showing better beam convergence by increasing the number of rows of the phased array. Scale bars are 3 mm. **c**, Comparison of the ultrasonic mappings of the three scenarios (from left to right: 1, 3, 5 rows, respectively), sharing the same intensity scale. Besides the enhancement in directivity, the beam intensity also increases with the number of rows. Scale bars are 2 mm. **d**, The beam width (red) and intensity (black) of the phased array with 1, 3, and 5 rows. More rows of the phased array lead to both higher beam directivity and intensity. All ultrasonic field data in **b** and **c** are mapped by an Ultrasonic Intensity Measurement System (Onda, Sunnyvale, CA).

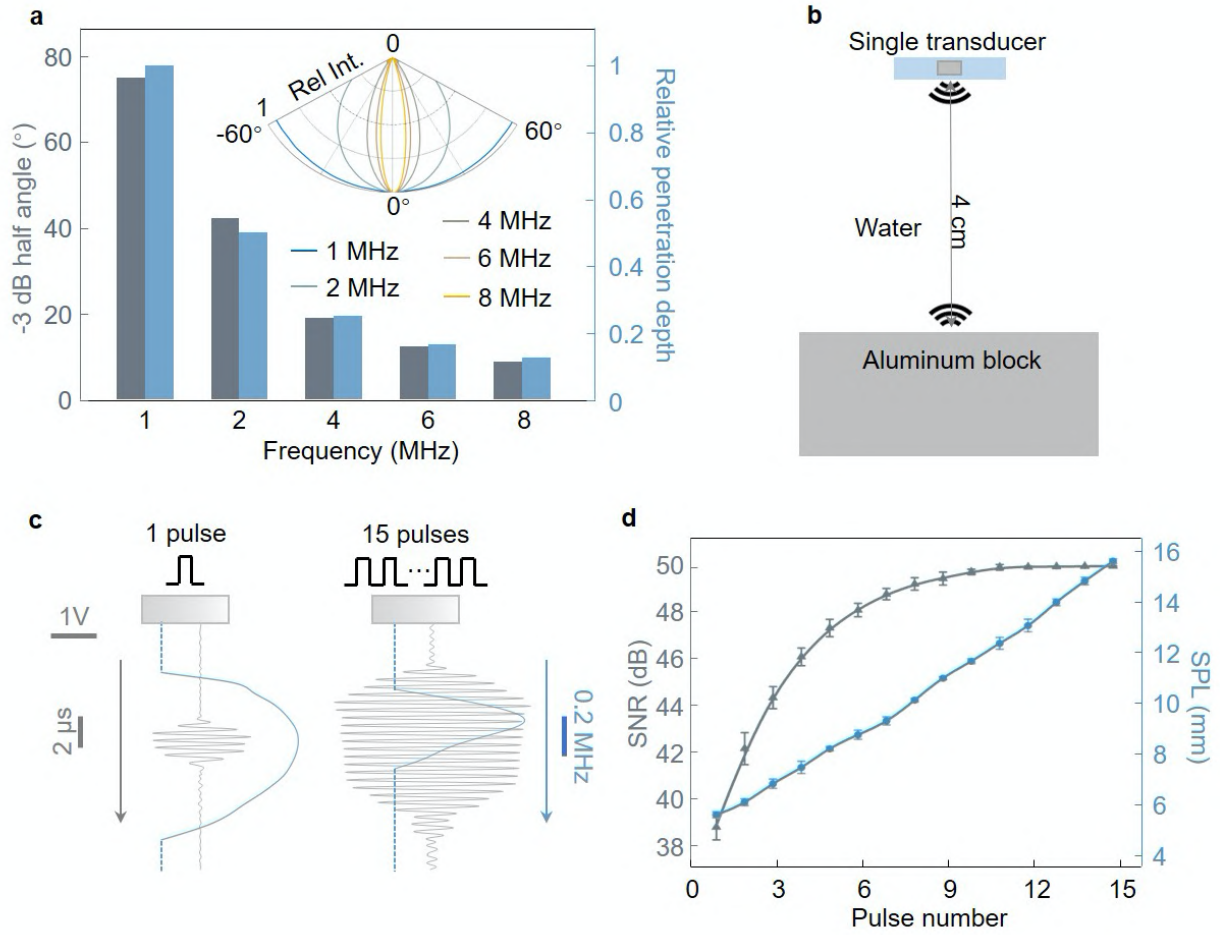

Supplementary Fig. 12 | Tuning the ultrasonic performance of a single element by the center frequency and the number of excitation pulses. The tunable properties of a single element include beam directivity, penetration, the bandwidth of the received signals, SNR, and spatial pulse length (SPL). **a**, Simulated -3 dB half-angle and penetration depth of a single element at frequencies from 1 to 8 MHz. The beam has high directivities at high frequencies, and vice versa; the beam has long penetration depths at low frequencies, and vice versa. Inset is the simulated beam pattern at different frequencies, with the largest beam spreading at low frequencies. The data are derived from Field II, MATLAB (MathWorks, Natick, MA). **b**, The experiment setup for a single element ultrasonic emission and receiving characterizations. **c,** Radiofrequency and corresponding fast Fourier transform (FFT) signals of a single pulse (left) and multi-pulse (right) excitation. The longer pulse duration and smaller bandwidth of the multi-pulse excitation enhance the sensitivity of the phased array probe to Doppler frequency shifts. **d**, Experimental characterizations of the SNR and SPL of a single element with different numbers of excitation pulses, showing enhancement in both the SNR and SPL with multi-pulse excitation. The signal is reflected from an aluminum block that is 2 cm away from the transducer.

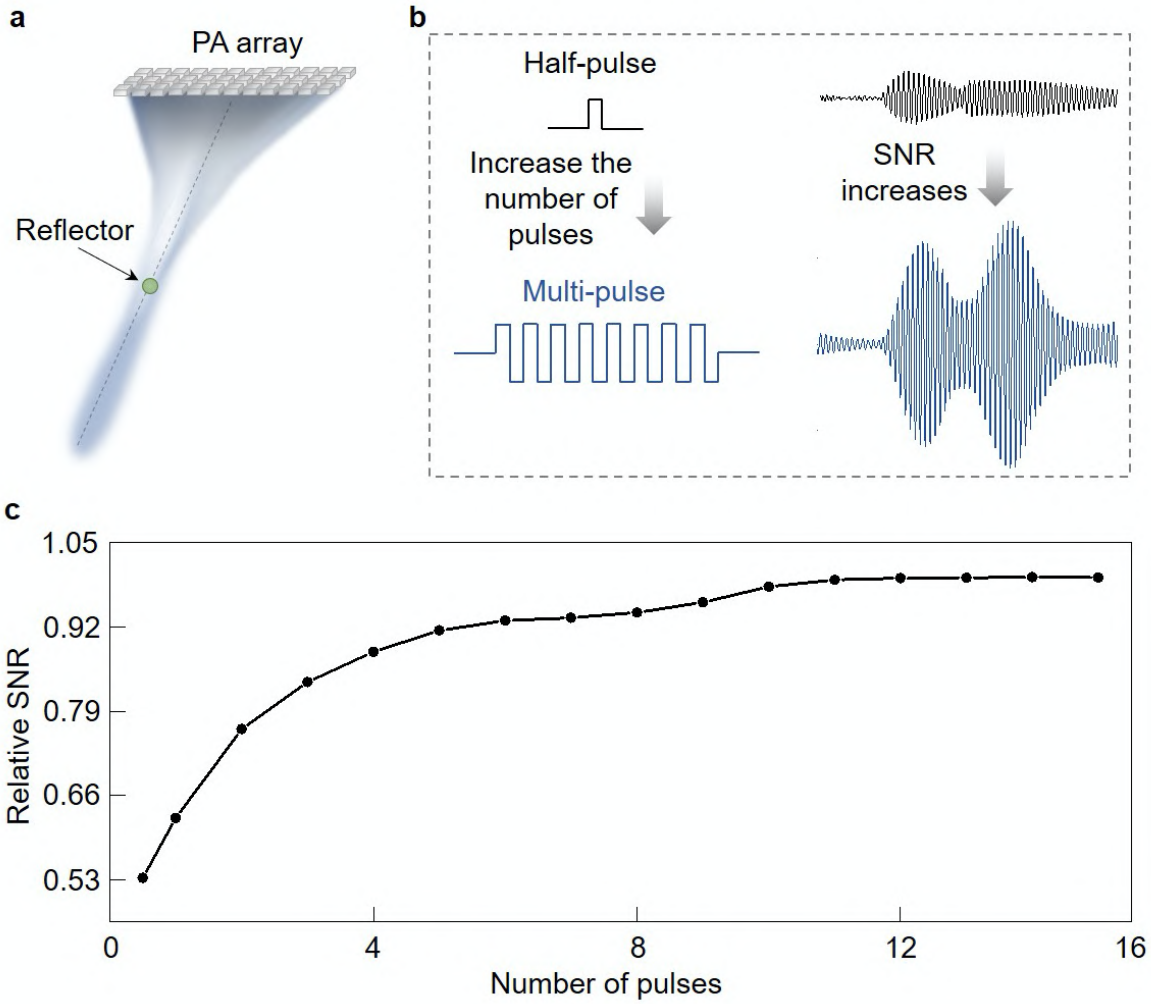

Supplementary Fig. 13 | Enhancement in the SNR of the phased array by multi-pulse excitation. a, A schematic image of the phased array with a reflector of 1 mm in diameter placed in the focused beam, simulating a sensing scenario in clinical applications. **b**, Schematic illustration of the half-pulse and multi-pulse excitation signals. The corresponding received signals are on the right, showing the enhanced SNR with multi-pulse excitation. **c**, The SNR (under a 10 cm depth in the tissue) as a function of the number of excitation pulses, showing that the SNR increases with the number of pulses for exciting the phased array elements.

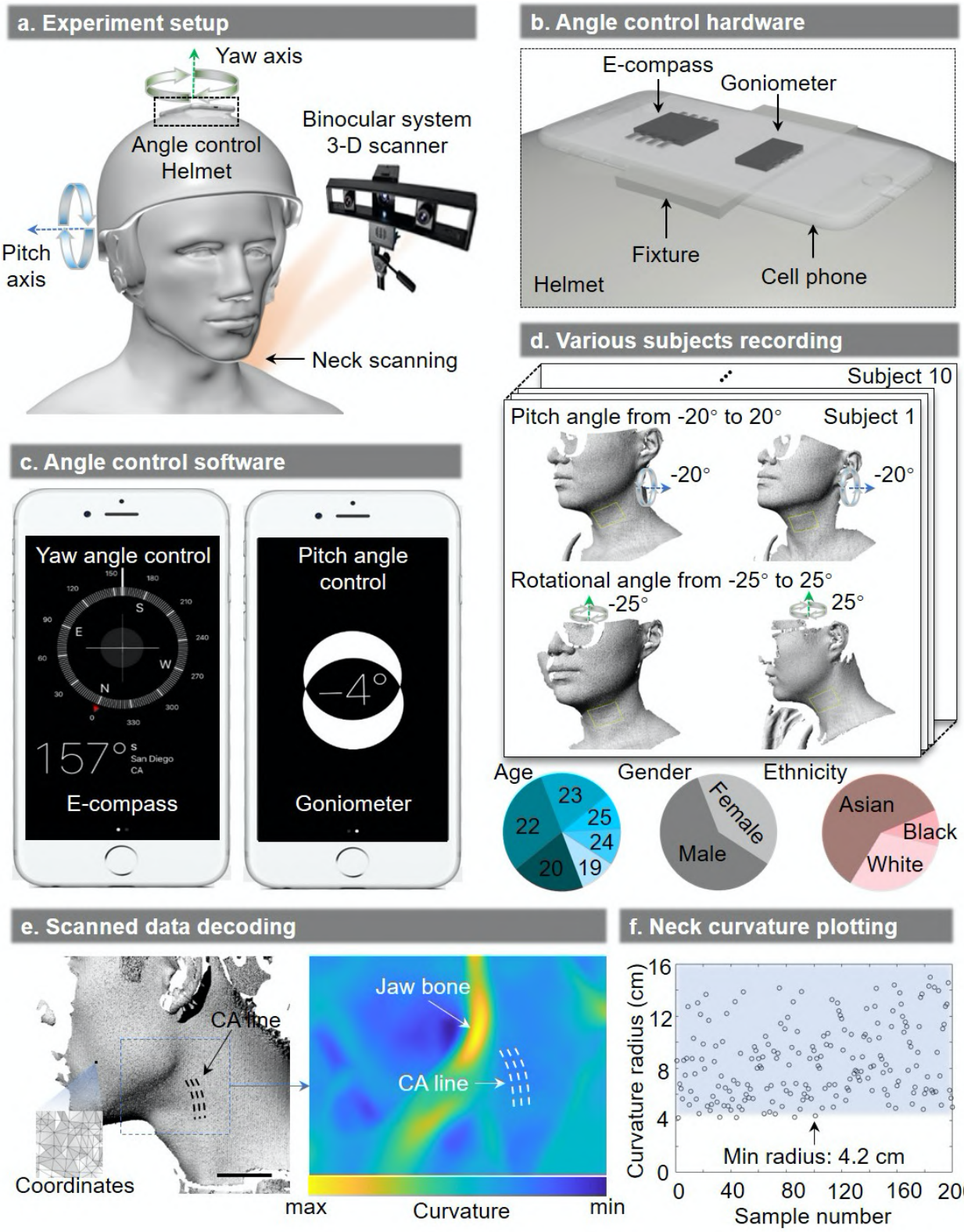

Supplementary Fig. 14 | Characterization of the skin curvature on the human neck in typical postures. a, Schematic setup for scanning the skin curvature. The posture is characterized by a helmet equipped with kinematic sensors. The posture is characterized by two axes of rotation, i.e., pitch and yaw. The skin surface in each posture is scanned by a 3D scanner (HDI Advances, LMI Technologies, Vancouver, Canada) to determine its maximum curvature. **b**, Detailed information about the hardware for posture characterization. A cell phone with a built-in E-compass and a goniometer is fixed on the helmet for sensing and characterization of the neck posture. **c**, Pitch and yaw angle reading software interface in the cell phone. **d**, The designated postures for the skin posture measurements (top) and the demographic information of the 20 test subjects (bottom). The measured pitch angle ranges from -20° to 20°; the measured yaw angle ranges from -25° to 25°. We sampled each subject for 10 curvatures at 10 various postures. **e**, The detailed process for analyzing the scanned data. The left panel shows the raw digital model recreated by the 3D

scanning, with the position of the carotid artery (CA) marked. The zoomed-in image at the lower-left corner shows an example of the skin profile information extracted from the raw model on a small area of the skin, which is used for local skin curvature calculations. The right panel shows the calculated curvature distribution in the region near the CA. **f**, Skin curvature distribution near the CA, showing the minimum curvature radius of all subjects is about 4.2 cm, which indicates the required deformation tolerance of the stretchable phased array.

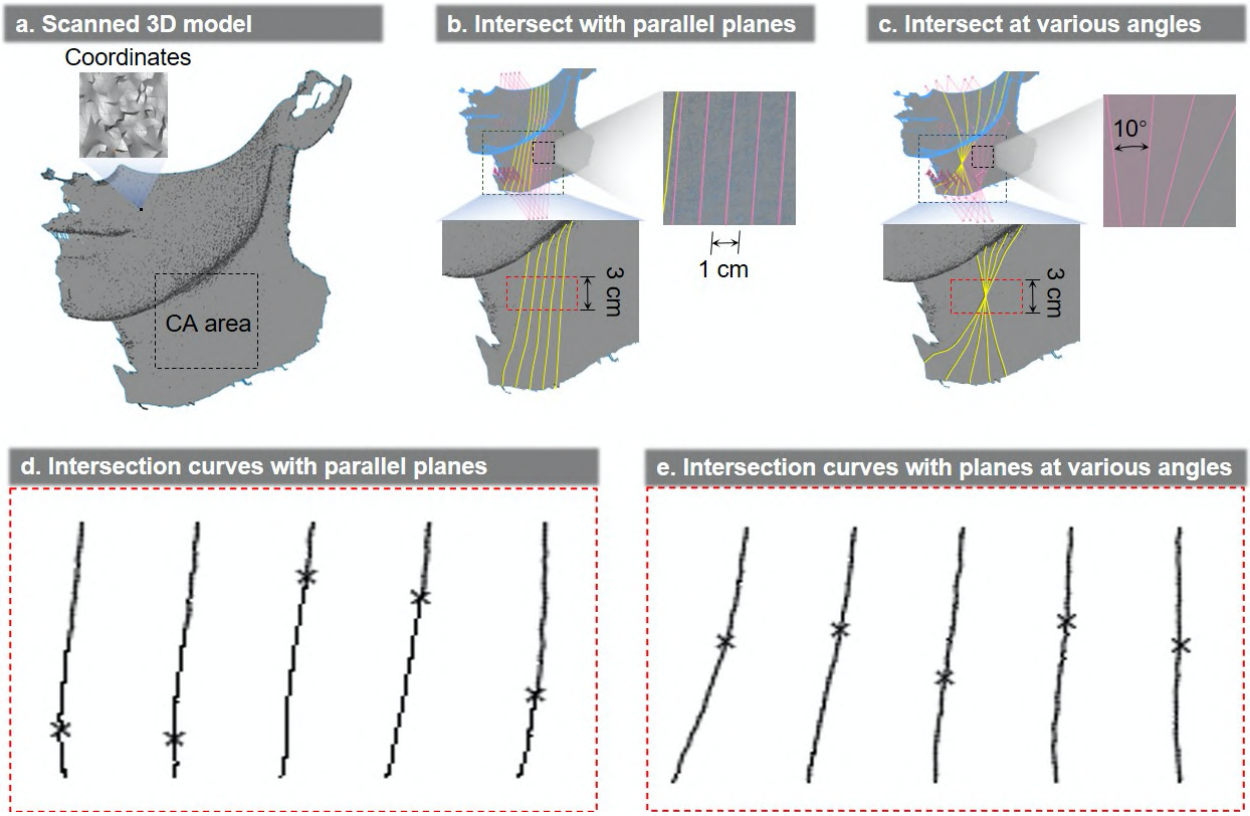

Supplementary Fig. 15 | Detailed skin curvature calculation protocols. a, A raw digital model from the skin curvature scanning. The 3D mesh digital model is created by a 3D scanner (HDI Advances, LMI Technologies, Vancouver, Canada). **b,** Five datum planes parallel to the CA line, with a pitch of 1 cm, are drawn to intersect the 3D model, generating five intersection curves. The intersecting lines on the skin surface are delineated in yellow. **c**, Five datum planes are drawn to intersect at the normal to the surface of the 3D model at a selected point near the CA, with an angle increment of 10°, generating five intersection curves. The goal is to ensure adjacent planes in the rotating direction can be processed near the actual CA line. **d,** A zoomed-in image of the intersection curves near the CA (area in the dashed lines in **b**). **e**, A zoomed-in image of the intersection curves near the CA (area in the dashed box in **c**). The intersection curves are used to identify the maximum curvature of the human neck skin in a specific body posture. The cross on each curve marks the point of maximum curvature along that curve. We pick the maximum curvature of all intersection curves in the typical human postures to represent the maximum curvature near the CA.

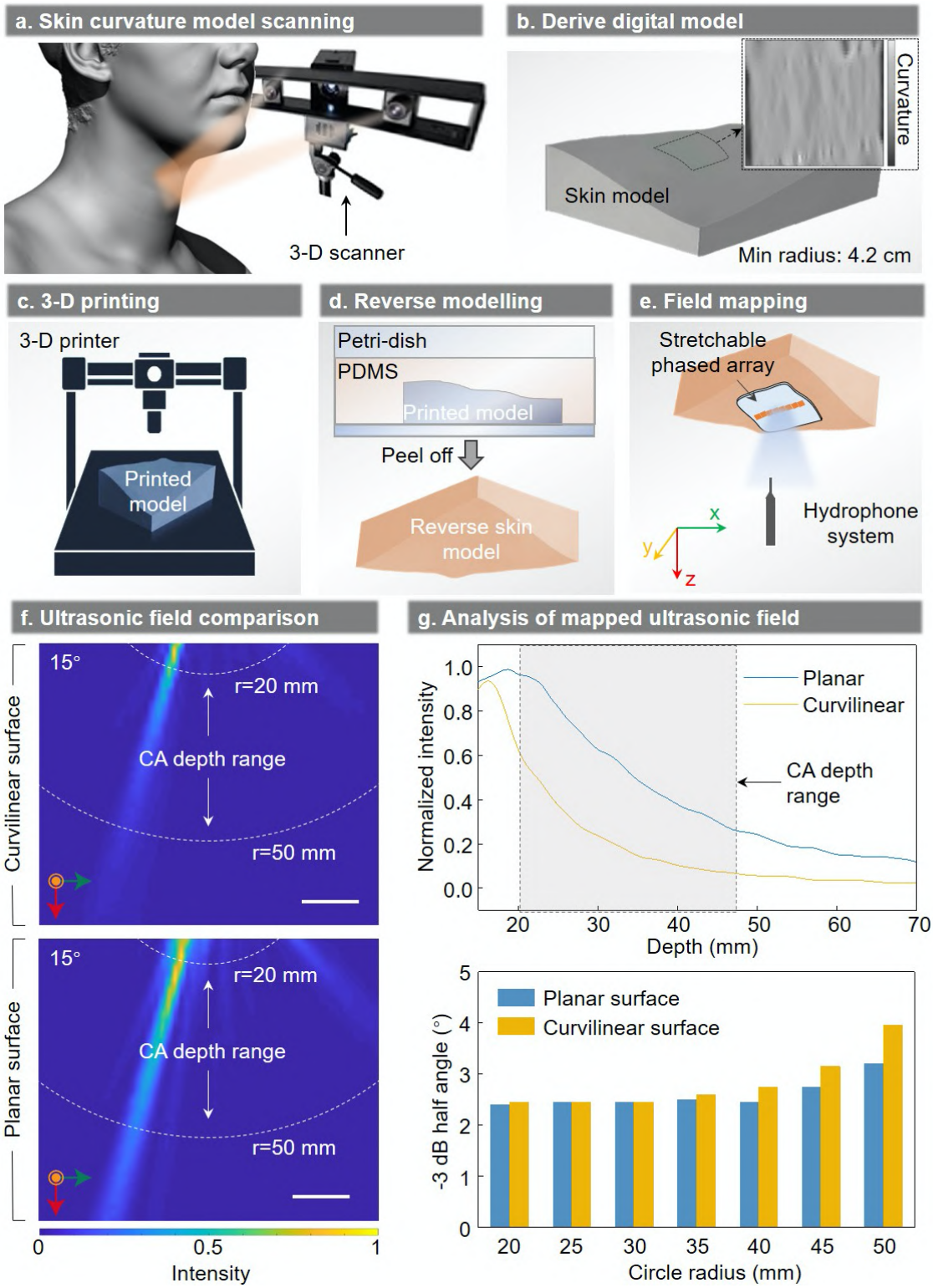

Supplementary Fig. 16 | Performance of the stretchable phased array in the x-z plane at the CA depth on a phantom replicated from the human neck. First, we created a 3D digital model from 3D scans of the human neck. A polydimethylsiloxane (PDMS) phantom was then cast from a 3D printed mold and used for subsequent probe testing. **a**, A schematic setup for scanning the skin curvature on the human neck. **b**, A 3D digital model created from the scan. **c**, A schematic setup for the phantom creation with 3D printing. **d**, A cast setup using the 3D printed model as the mold to cure the PDMS phantom. **e**, A schematic setup for mapping ultrasonic fields of the stretchable phased array. **f**, Mapped ultrasonic fields of the stretchable phased array on a curvilinear surface (top panel) and a flat surface (bottom panel). The depth range of the CA is marked by the dashed lines. The mapping intensity results share the same scale bar. **g**, Beam intensity (top panel) and directivity (bottom panel) analysis of the stretchable phased array at different depths. The performance of the stretchable phased array is comparable on the two surfaces. The shaded area in the top panel represents the depth range of the CA.

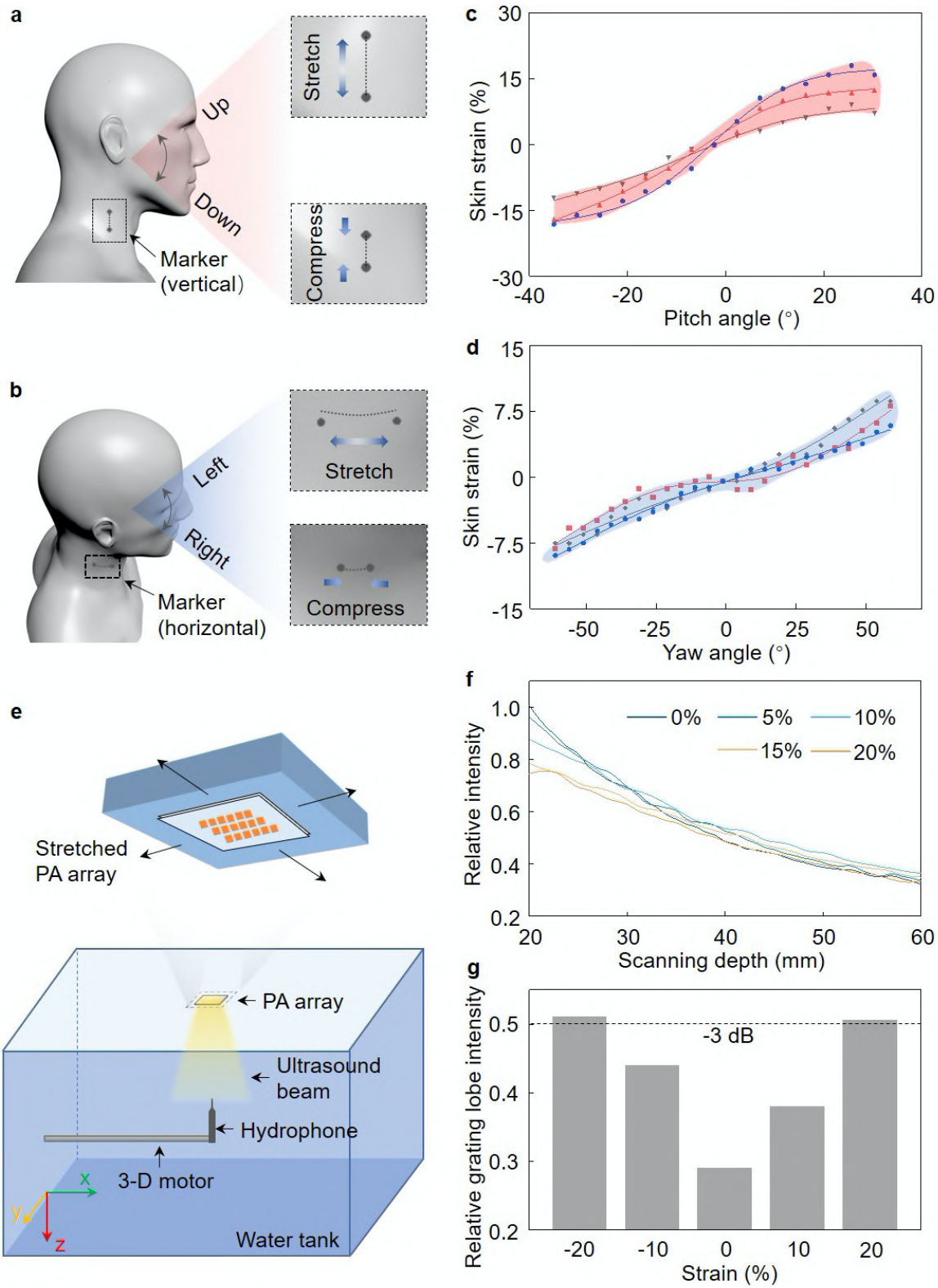

Supplementary Fig. 17 | Performance of the stretchable phased array under tensile and compressive strain. a, A schematic experiment setup for strain characterization of the human neck skin during head flexion/extension. A pair of markers are applied to the human neck near the CA region in the vertical direction. The distance between the two markers will increase/decrease when the subject lowers/lifts the head. **b**, A schematic experiment setup for strain characterization of the human neck skin during head rotation. A pair of markers are applied to the human neck near the CA region in the vertical direction. The distance between the two markers will increase/decrease when the subject turns the head left/right. **c**, The strain of the human neck skin as a function of the pitch (flexion/extension) angle. The data is measured by a 3D scanner (HDI Advances, LMI Technologies, Vancouver, Canada). **d**, The strain of the neck skin as a function of the yaw (rotation) angle. The negative sign means the strain is compressive. Note that the skin will not be under compressive strain but will form wrinkles to adapt to the compression. The data is

measured by a 3D scanner (HDI Advances, LMI Technologies, Vancouver, Canada). **e**, A schematic experiment setup for characterizing the performance of the stretchable phased array under biaxial tensile strain applied with a mechanical stretcher. The mapping system is illustrated in the bottom panel. PA: phased array. **f**, Beam intensity of the stretchable phased array under 0% - 20% tensile strain. The strain does not have a significant impact on the intensity of the main beam. The data are mapped using an Ultrasonic Intensity Measurement System (Onda, Sunnyvale, CA). **g**, Relative grating lobe intensity of the stretchable phased array under -20% - 20% strain. The data in the tensile strain are measured in the experiment, and the data in the compressive strain regime are derived from the simulation in Field II, MATLAB (MathWorks, Natick, MA). The -3 dB threshold is labeled which the grating lobe starts to influence the main beam in biomedical applications. The result shows the working range of the device is around 20% of tensile strain. Overly stretching will further increase the grating lobe intensity and thus decrease the SNR along the main beam direction.

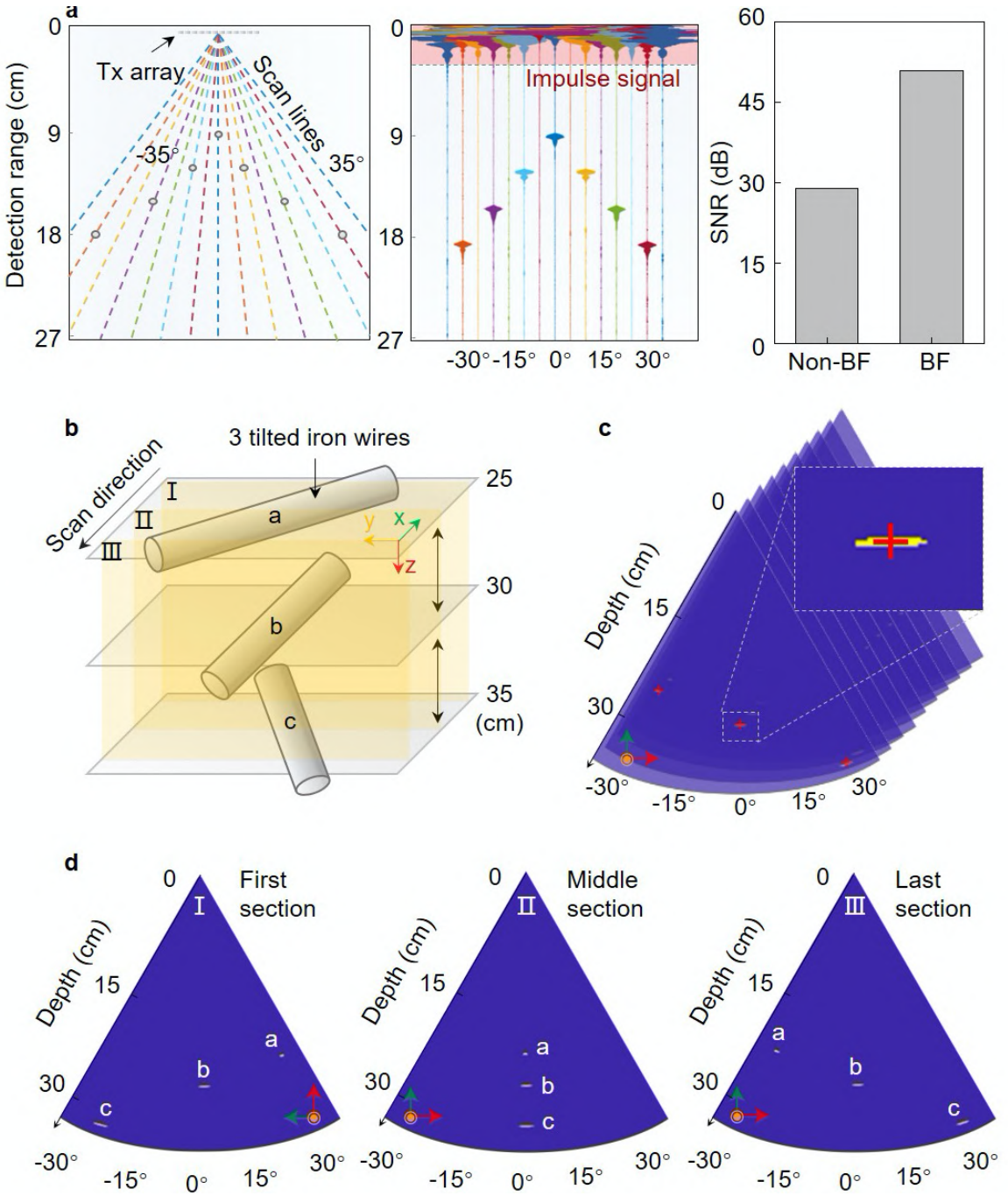

Supplementary Fig. 18 | A large sensing range of the stretchable phased array in x-z plane enabled by phased array receive beamforming. a, A designed experimental setup at 10~20 cm depth in water (the left panel). Tx: transducer. Seven reflectors (iron wires, marked by the circles) are arranged at a depth of 9, 12, 15, and 18 cm, respectively, at an angle with the vertical direction being 0°, 10°, 20°, and 30°, respectively. To detect those targets, 15 beamlines are created at an incidence angle of -35° to 35°, with a 5° increment. The received signals from the corresponding beamlines are in the middle panel. Pulse signals (in the pink shaded area) are due to the ringing effect of the transducer. The pulse signals will not be used to track objects. The SNR is enhanced and reaches 51 dB after implementing the phased array receive beamforming, as shown in the right panel. The high-quality signals from the stretchable phased array demonstrate its potential for deep tissue sensing. **b**, 3D imaging of three reflectors (iron wires) at a depth of 25 cm (wire a), 30 cm (wire b), and 35 cm (wire c), in different orientations (-30° to 30° in the x-y plane). **c**, Ten consecutive cross-sectional images along the y-axis of the 3D image generated with the stretchable phased array in the sensing scenario in **b**. The 3D scans were conducted by adopting the strategy as illustrated in Supplementary Fig. 8. The positions of the reflectors are labeled by the red cross. The inset shows a zoomed-in image of a reflector. **d**, Three representative cross-sections I, II, and III from **c** with the same scale as **c**. The images are processed using the binarization method (with a 5 V signal threshold). The gain is 100 dB.

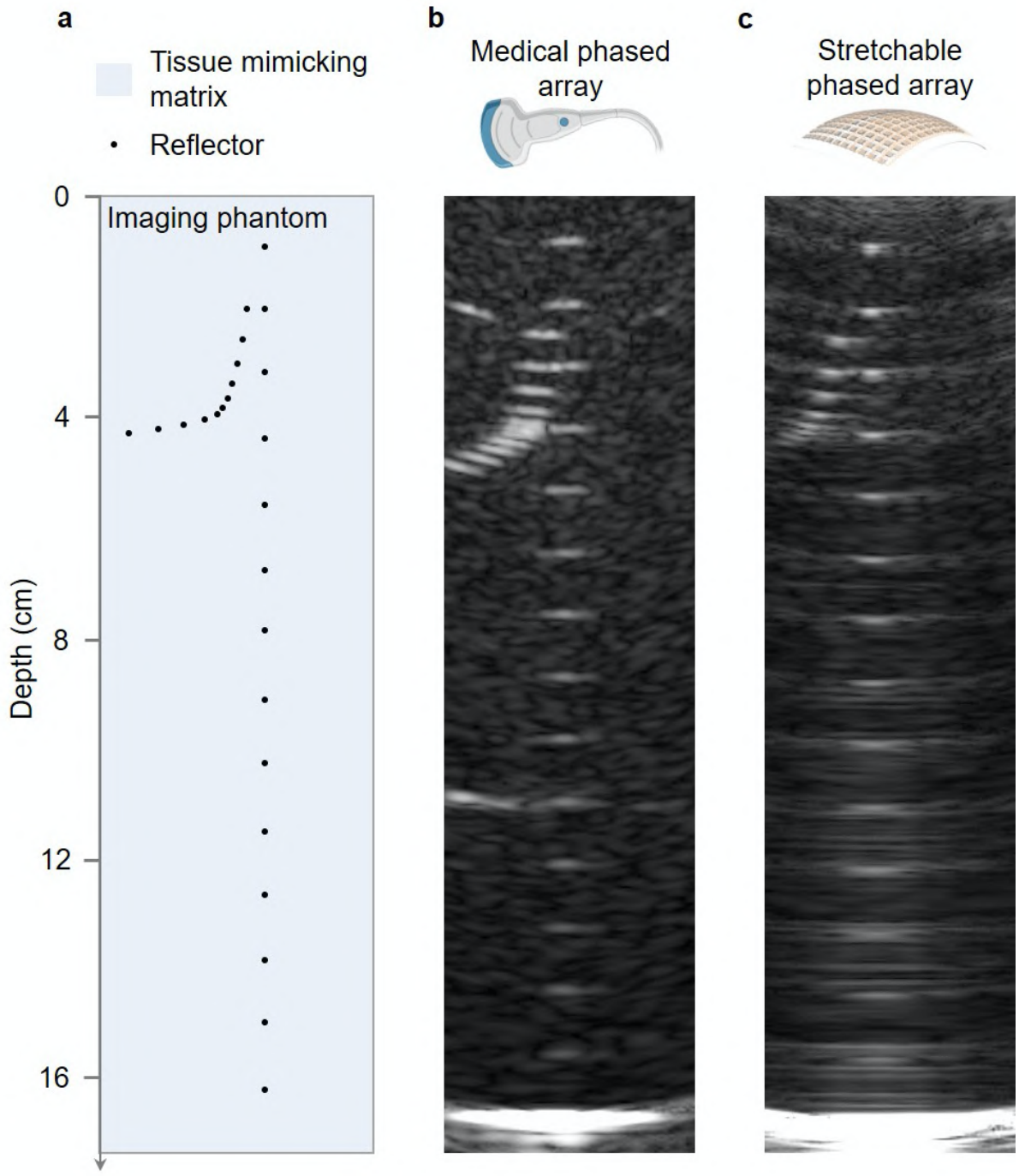

Supplementary Fig. 19 | Detection comparison between the stretchable phased array and a commercial probe on a tissue-mimicking phantom under the same ultrasonic window. a, A tissue-mimicking phantom with reflectors distributed at 0 - 17 cm depth. **b**, The imaging result of a commercial medical ultrasonic probe (Verasonics, P4-2v probe). **c**, The imaging result of the stretchable phased array. The ultrasonic window of our system is ±20°and 17 cm in depth, which is the largest ultrasonic window of the commercial ultrasound system (Chison Eco 5) in our group.

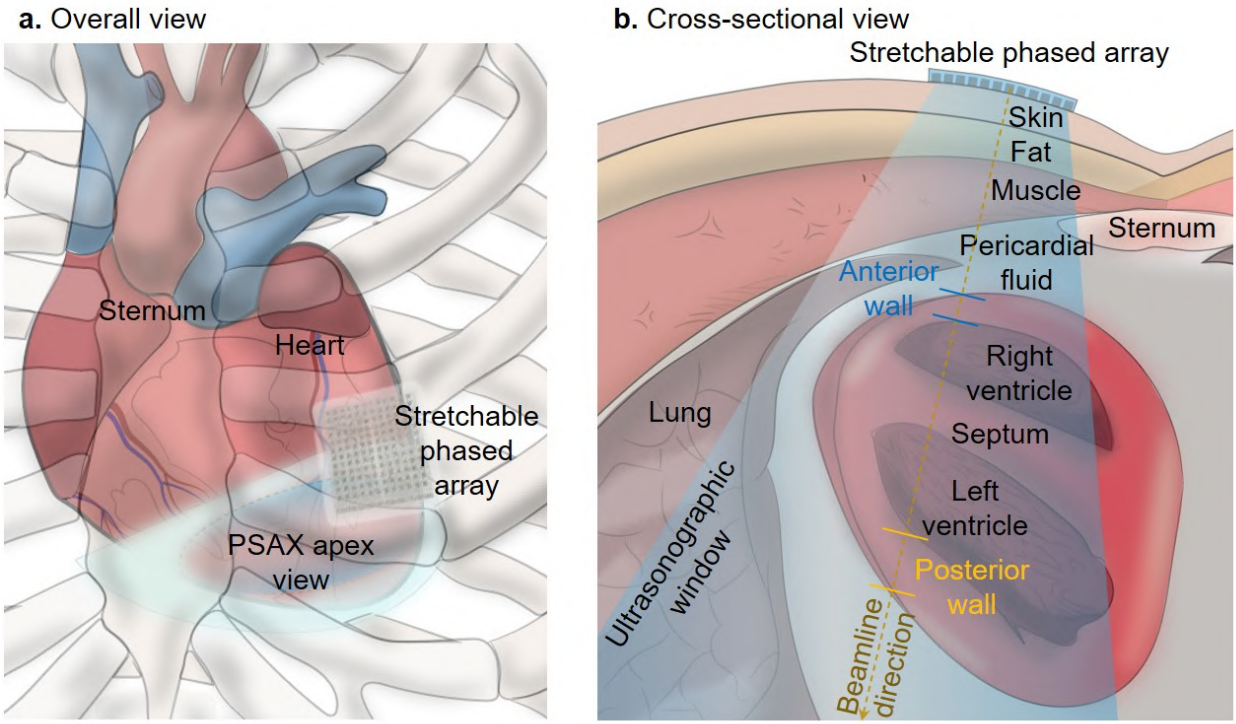

Supplementary Fig. 20 | Anatomy of the human chest during tissue Doppler measurements of cardiac muscles. a, The position of the device on the chest relative to the bones and the heart. **b**, The cross-sectional structure of the parasternal short axis (PSAX) view, showing the relative position and orientation of the stretchable phased array, the insonation area, and nearby tissue structures. The beamline penetrates various tissue layers, including the skin, fat, muscle, pericardial fluid, right ventricle anterior wall, right ventricle, septum, left ventricle, and left ventricle posterior wall.

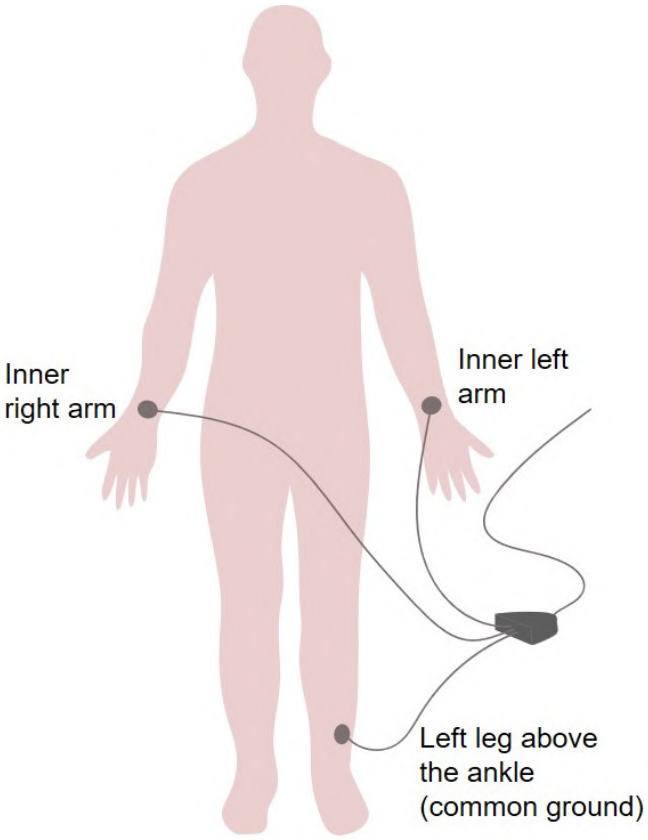

Supplementary Fig. 21 | Schematic illustration of the electrode placement for ECG measurements. Three electrodes are placed at different locations on the limb, including one on each of the inner lower arms, and one on the left leg above the ankle for the common ground.

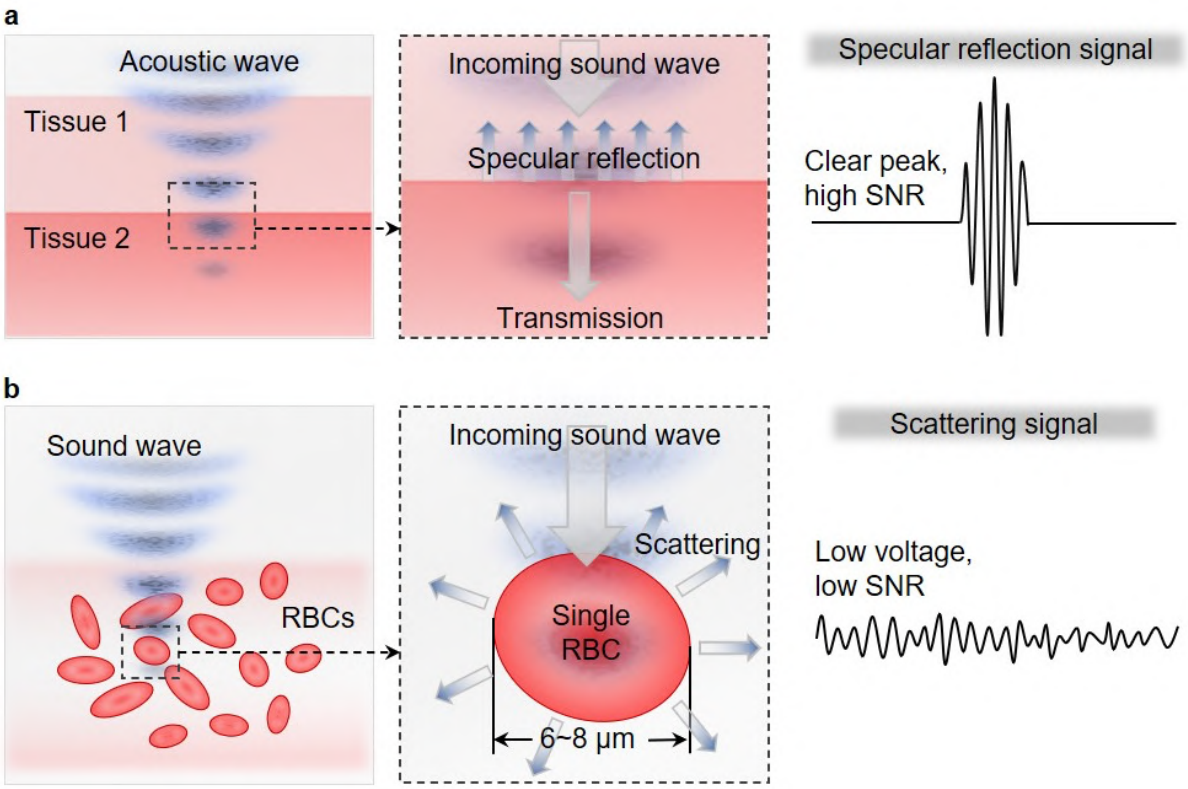

Supplementary Fig. 22 | The distinction between specular reflection and scattering, two major forms of interaction between sound waves and tissues. a, Specular reflection happens when sound meets an interface between two tissues with different ultrasonic properties, i.e., ultrasonic impedance (the left panel). The zoomed-in image in the middle panel shows more details of the specular reflection. Because the interface is much larger compared to the sound wavelength, a large portion of the ultrasonic energy will be bounced back. Specifically, the reflection/transmission ratio depends on the ultrasonic impedance difference between tissues 1 and 2. The specular reflection usually has a clear peak with a relatively high SNR (the right panel). **b**, Scattering happens when sound waves interact with tissues or cells whose scales are much smaller than the sound wavelength, such as red blood cells (RBCs, 8~10 μm in size, the left panel). The zoomed-in image in the middle panel gives more details of scattering. The incoming sound wave will be dispersed by the microscopic tissues or cells in all directions. Therefore, the received reflection signal (along a specific direction) has relatively low SNR, compared to the specular reflection. To receive scattering signals requires relatively high-intensity sound compared to detecting specular reflections.

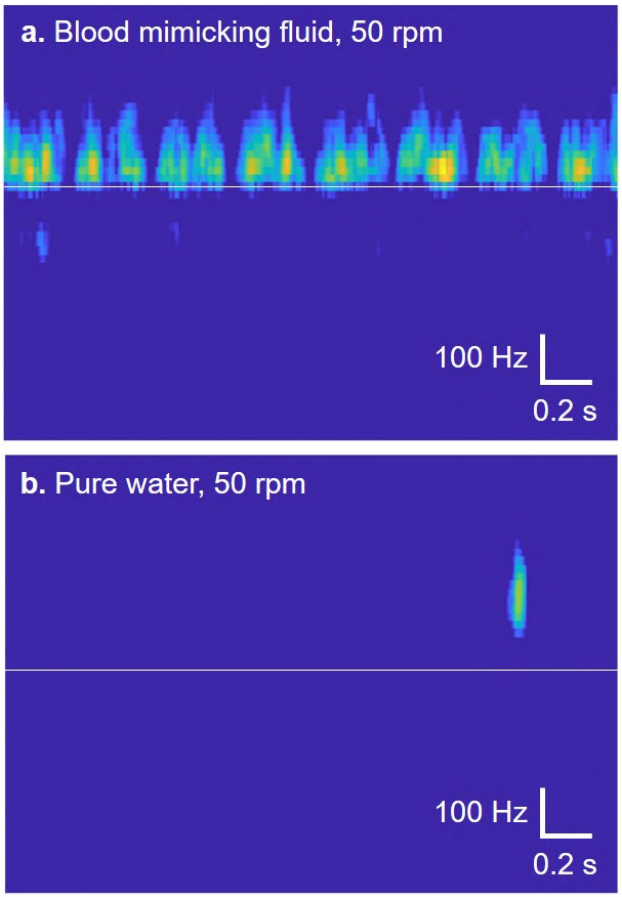

Supplementary Fig. 23 | The scattering spectra with and without scattering particles in water. The experiment is performed with a peristaltic pump **a** with and **b** without scattering particles. The results show that there is only a detectable Doppler shift when the fluid contains scattering particles (5 μm in size, at a concentration of 1.82%). Pure water cannot introduce any Doppler shift in the ultrasonic frequency in this study.

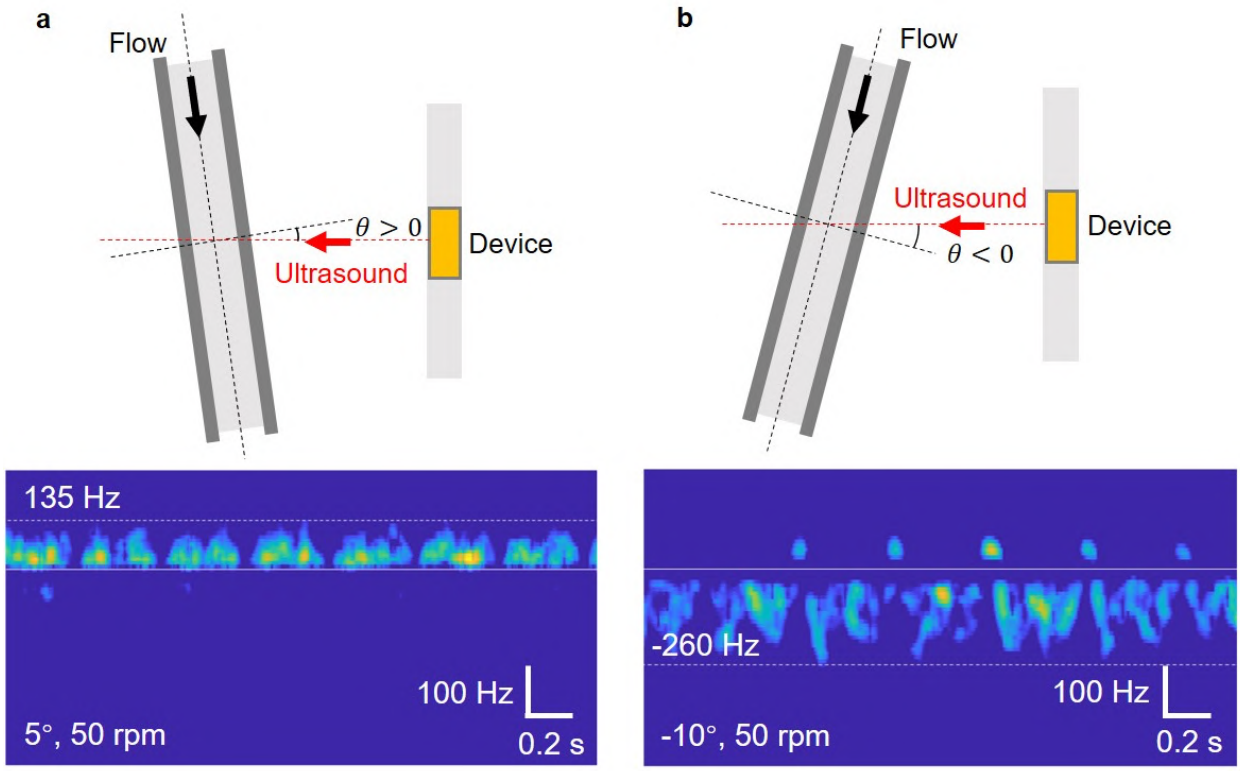

Supplementary Fig. 24 | Two key components for estimating the flow speed, including the Doppler shift and the Doppler angle. While measuring the same fluidic flow, the Doppler shift and the Doppler angle are two interdependent parameters that need to be measured to calculate the flow speed. **a**, Fluid flowing towards the ultrasonic wave can introduce a positive Doppler shift. The corresponding spectrum appears in the bottom panel. **b**, Fluid flowing in the same direction as the ultrasonic wave (with a smaller absolute angle than that in **a**) can introduce a greater, but negative Doppler shift, as shown by the corresponding spectrum in the bottom panel.

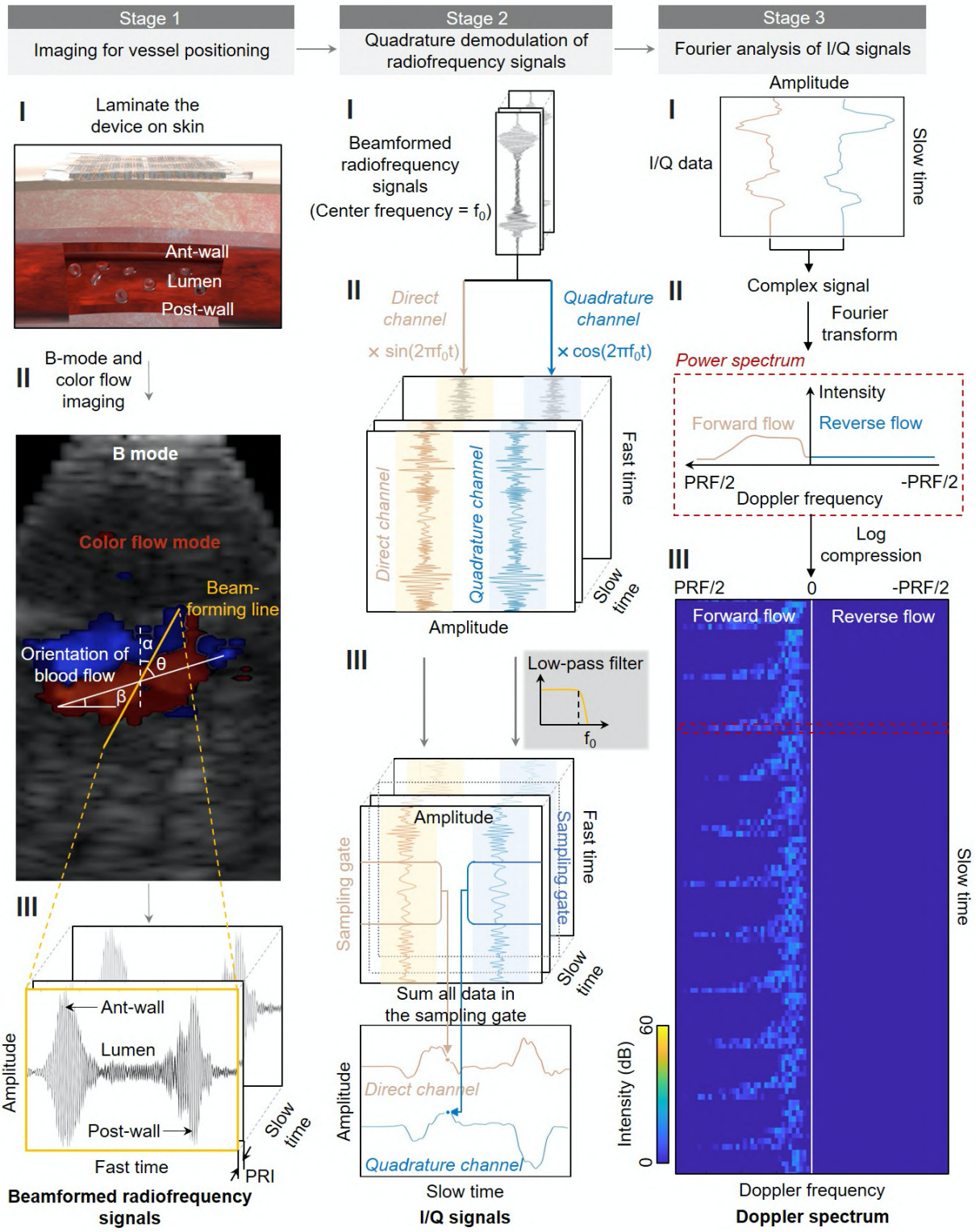

Supplementary Fig. 25 | The process of blood flow measurements using the stretchable phased array. The entire process is divided into three stages. **Stage 1: Imaging for vessel positioning.** The blood vessel contains three parts, including the anterior wall, the lumen area, and the posterior wall (step I). The device will perform combined B mode and color flow imaging (step II), which reveal the directional and spatial information of the vascular flow. The Doppler angles in Fig. 4d and 4e can be calculated as follows. According to measurements from the colour flow image at a beam incidence angle (α) of 20° (see Materials and Methods), the carotid artery and the jugular vein in Fig. 4d and 4e have an inclination angle (β) of 12° and 16°, corresponding to a Doppler angle (θ) of 58° and 54°, respectively, which are within an acceptable range. A beamforming line with an appropriate Doppler angle will then be defined to read out the Doppler information from the radiofrequency signals of this line (step III). In a single frame of the radiofrequency signals, the horizontal axis represents the time-of-flight, labeled as “Fast time”. The vertical axis represents the signal amplitude. From the radiofrequency signals, we can clearly tell the signals from the anterior wall,

lumen area, and posterior wall. The third axis, labeled as “Slow time”, represents the time of multiple ultrasonic wave generations. The time interval between two adjacent frames is the pulse repetition interval (PRI). These series of frames of the radiofrequency signals will be recorded as the raw data for further processing and analysis. **Stage 2: Quadrature demodulation of radiofrequency signals.** After the acquisition of the radiofrequency signals (step I), quadrature demodulation will be performed to extract the fluidic flow information of both the forward and the reverse directions. In step II, each frame of the radiofrequency signals will be multiplied by $\sin(2\pi f_0 t)$ and $\cos(2\pi f_0 t)$, respectively, forming two channels of signals, labeled as “Direct channel” and “Quadrature channel”. f_0 represents the center frequency of the ultrasonic signals. Then, in step III, the resulted signals will pass through a low-pass filter with a cutoff frequency equal to f_0. And then, a sampling gate will be applied to only collect the Doppler shift from the lumen area. All data in this sampling gate will be summed up, resulting in a single point in the in-phase and quadrature (I/Q) data, which is in the slow time domain. **Stage 3: Fourier analysis of I/Q signals.** This step translates the previous I/Q data to flow spectra. Two channels of real I/Q signals (step I) will be used to compose a new complex signal. In step II, by conducting an FFT of this composed signal, the intensity distribution of both scatters contributing to the forward flow and the reverse flow can be differentiated in the Doppler spectrum. The orange curve has a positive Doppler shift (on the left side of 0 Hz); the blue curve is the opposite. Then, in step III, the amplitude information will be encoded into brightness by log compression. By linking all single brightness mode pixels, the flow spectrum containing forward and backward fluidic flow information can be reconstructed. Under normal blood flow conditions at a regular velocity, the spectrum represents mixed Doppler frequencies existing in a particular vessel during a finite time span. Specifically, in the vessel lumen, particularly under laminar flow conditions, blood flow has a velocity gradient across the cross-section of the vessel, wherein the center has the greatest velocity, and the region close to the vascular wall has the least. The gradient in the flow velocities in the vessel lumen generates different scattering intensities.

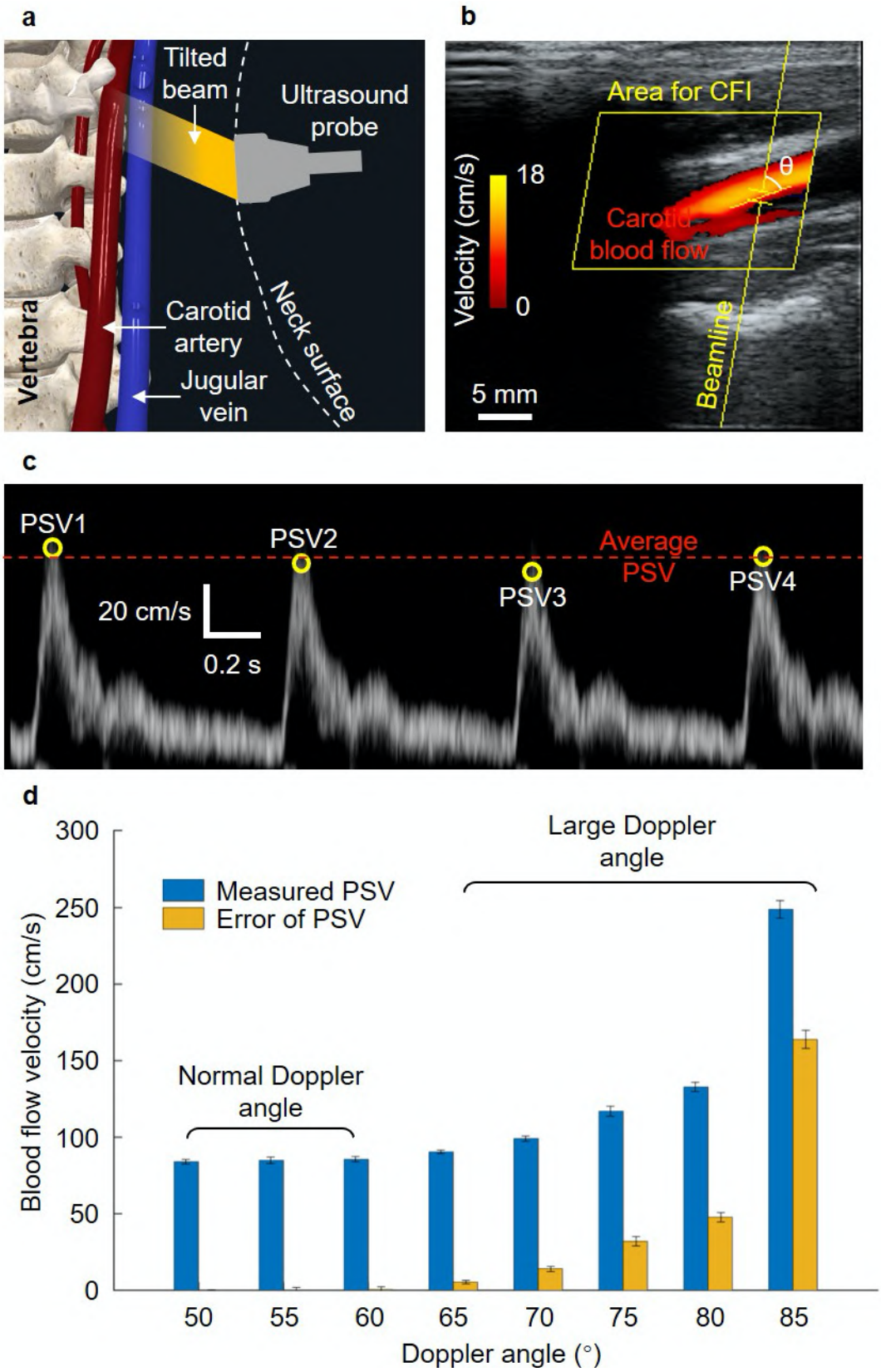

Supplementary Fig. 26 | Doppler angle dependence of the blood flow velocity measurements. a, Illustration of a tilted ultrasonic beam for blood flow measurements. **b**, Integrated B-mode and color flow imaging for measuring the Doppler angle (θ) between the carotid artery and the ultrasonic beam, which is essential for blood flow velocity calculation. **c**, Measured blood flow waveforms. Four peak systolic velocity (PSV) readings and the average PSV are labeled. **d**, Measured PSV (blue bars) and errors (orange bars) on the same subject with different Doppler angles (50°~85°). The measured PSV is significantly overestimated when the Doppler angle exceeds 60°. According to the translational equation between the Doppler shift and flow speed (see Materials and Methods), the larger θ is, the closer $\cos\theta$ is to zero, and the larger the measurement error will be. The Errors of the measured PSV are shown by the orange bars.

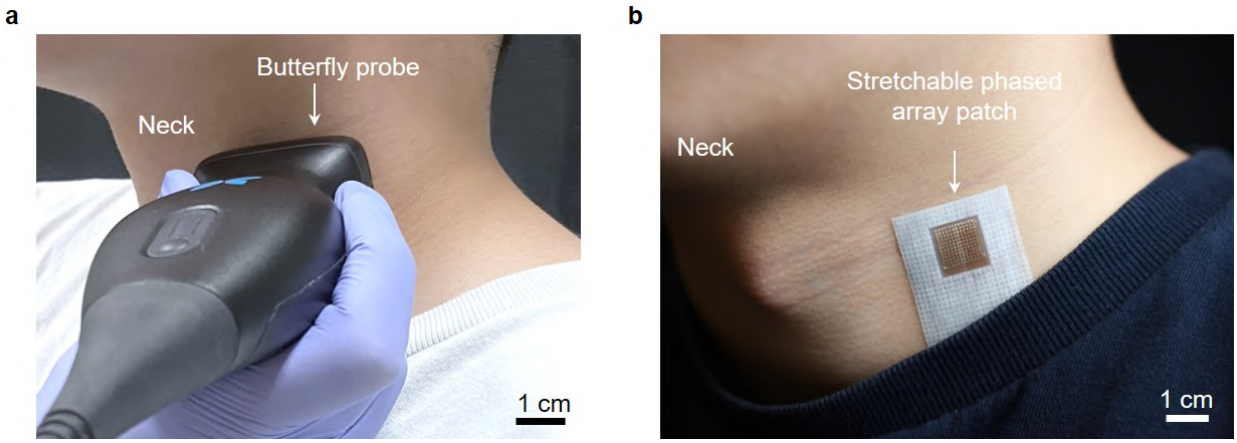

Supplementary Fig. 27 | The long-term skin integration comparison between a, a commercial Butterfly system (the benchmark of cellphone based portable ultrasonic systems) and **b,** a stretchable phased array demonstrated in this work.

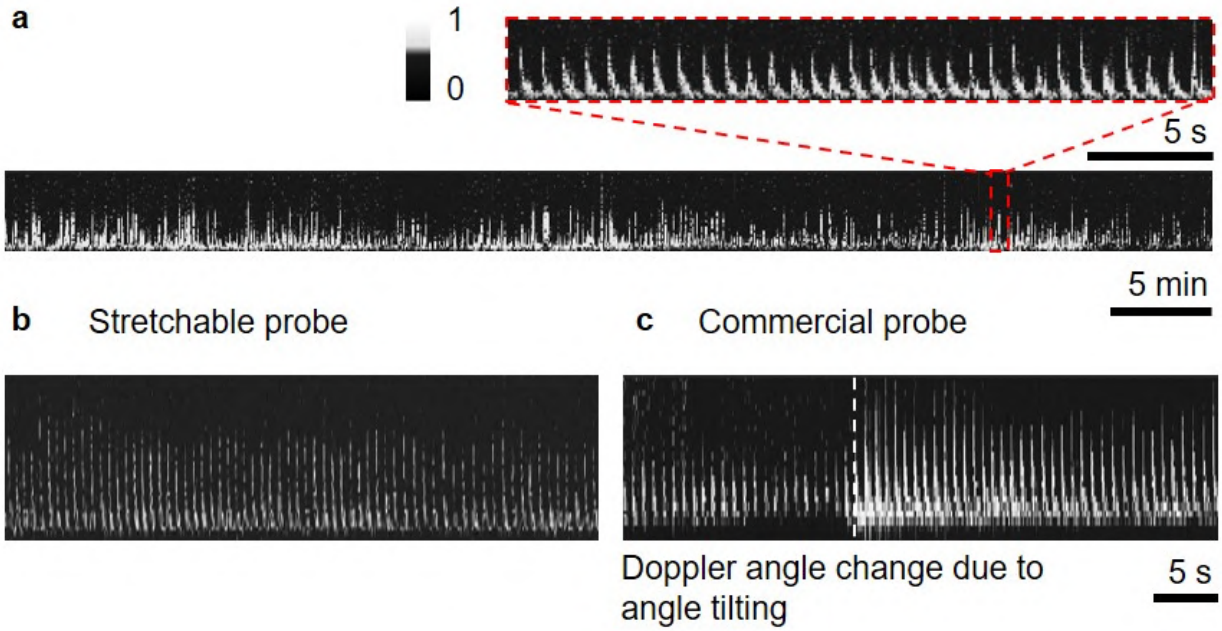

Supplementary Fig. 28 | Continuous recordings of blood flow signals. a, Raw traces of carotid blood flow spectrum of 1 hour. The inset shows the detailed feature of the data trace. **b,** and **c**, are the comparisons between the continuous recording (1 minute) of the stretchable probe and a hand-held probe (the butterfly system) using standard operations. The blood flow traces recorded by the commercial probe requires stable holding, which is very challenging for humans, especially in long-term.

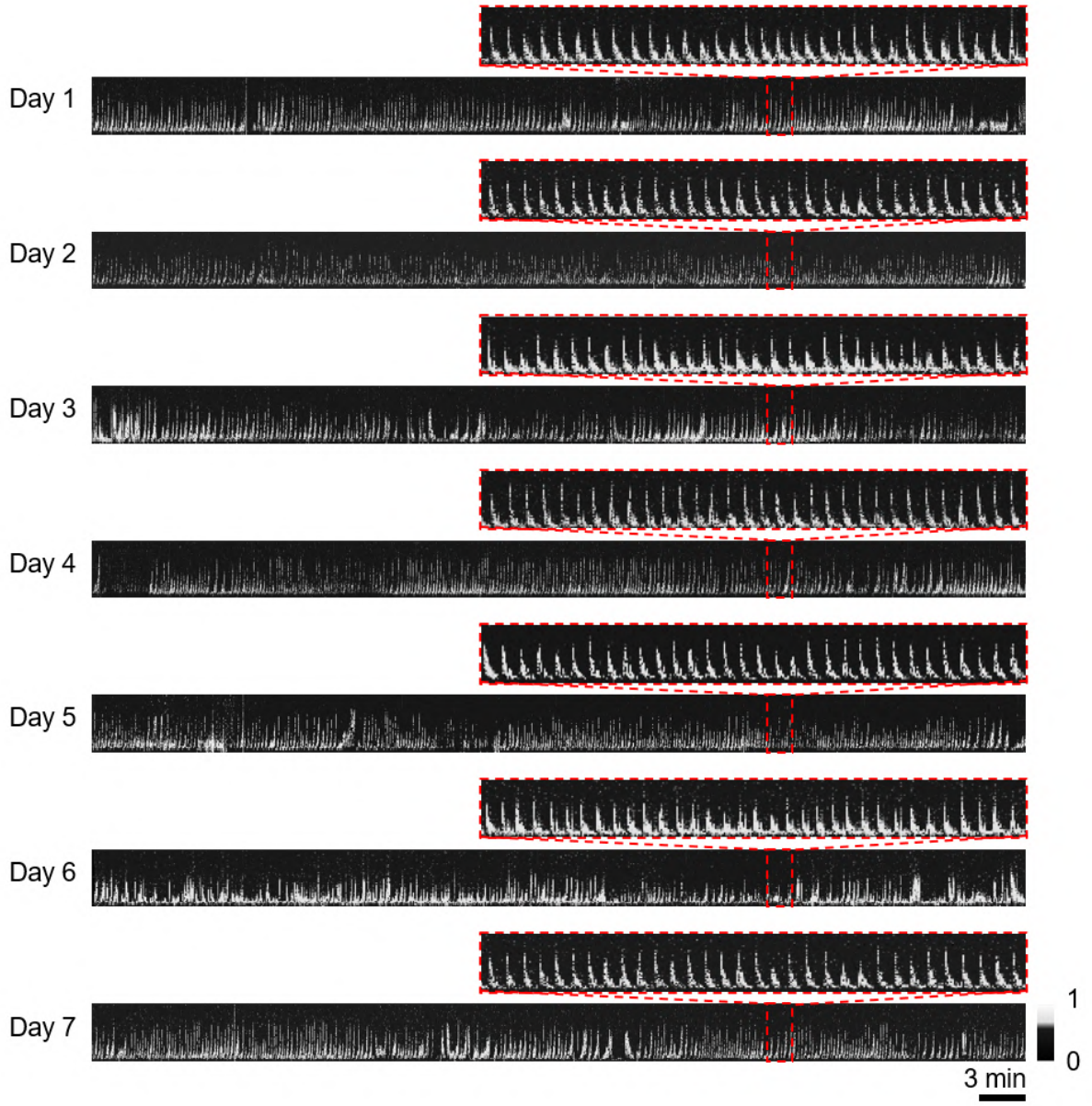

Supplementary Fig. 29 | Raw traces of carotid blood flow spectra recorded from the carotid artery by the stretchable phased array. Each trace lasts 60 minutes. The measurements are for seven consecutive days.

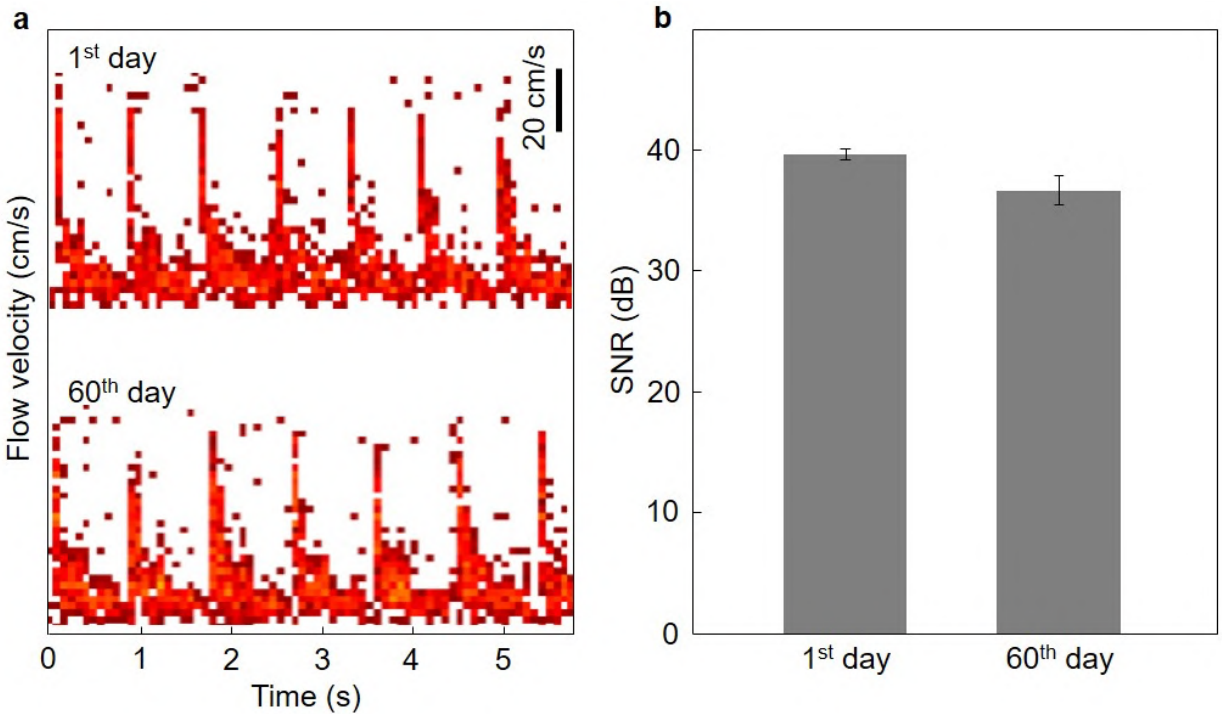

Supplementary Fig. 30 | The lifetime of the stretchable phased array. a, Measurements of CBF of a subject on the 1st day right after device fabrication (top) and on the 60th day (bottom) using the same device on the same human subject. Both tests can achieve reliable and similar results. Heart rates for the 1st day and the 60th day are 71 and 64 beats per minute, respectively. **b**, SNRs of the same device, measured underwater at a depth of 30 cm on the 1st day and 60th day, showing a 2.5 dB drop after long-term testing, probably due to the wear of the substrate, potential depolarization of the transducer material, or the degradation of the $PbZrTiO_3$-based transducer material induced by moisture. The average device usage between the 1st and 60th days is ~3-4 times per week. Each testing lasts 30 minutes to 1 hour.

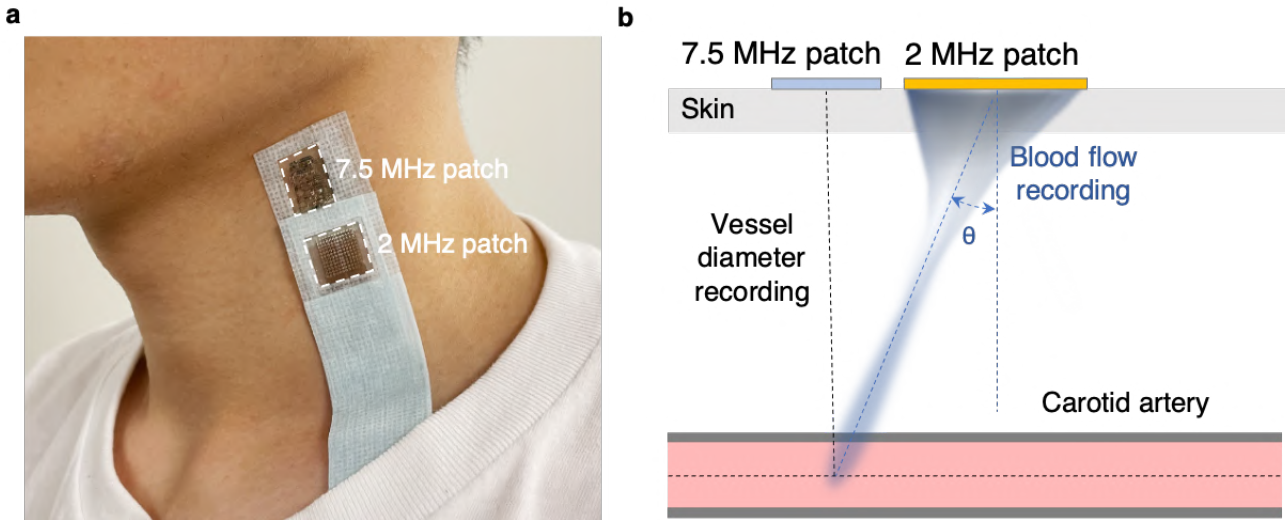

Supplementary Fig. 31 | The testing setup for carotid output measurements. a, A picture showing the location of the 7.5 MHz patch and the 2 MHz patch on the skin. **b,** Schematics showing the measurement cross-section of the simultaneous measurements, where key components are labelled.

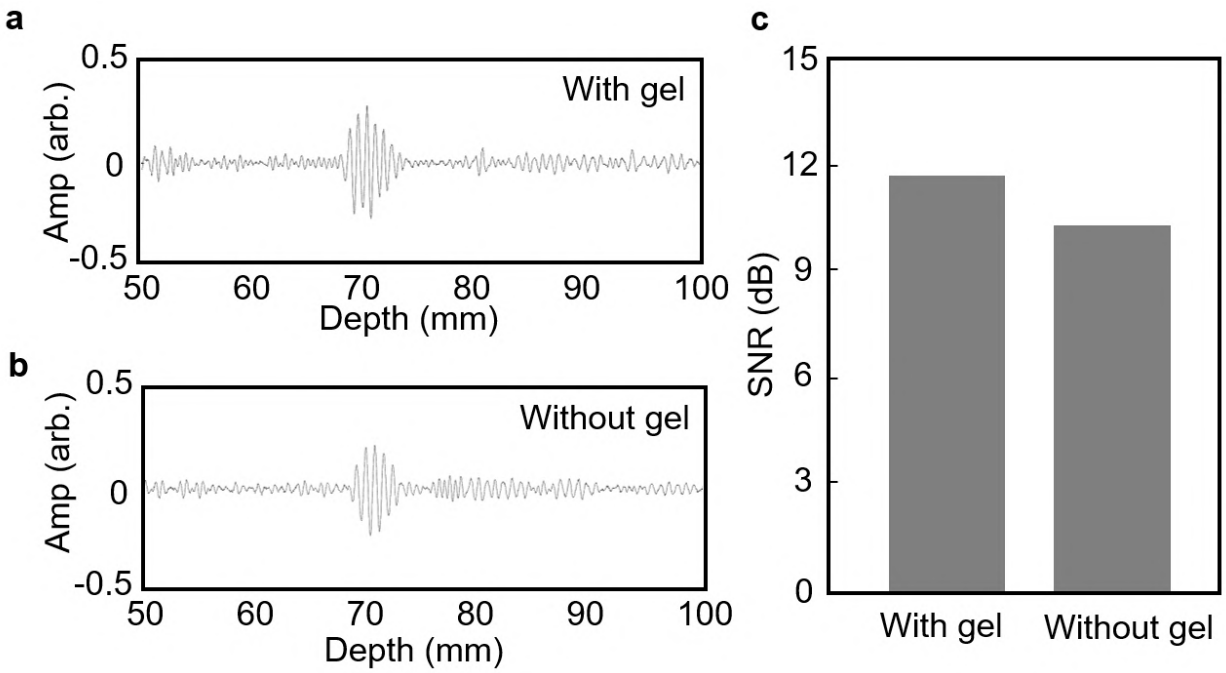

Supplementary Fig. 32 | The ultrasonic emission performance comparison of a single element in a stretchable array on a tissue phantom with and without ultrasonic gels. Received signals of the single element **a**, with and **b**, without gels. **c**, Comparison of the corresponding SNRs of the received signals.

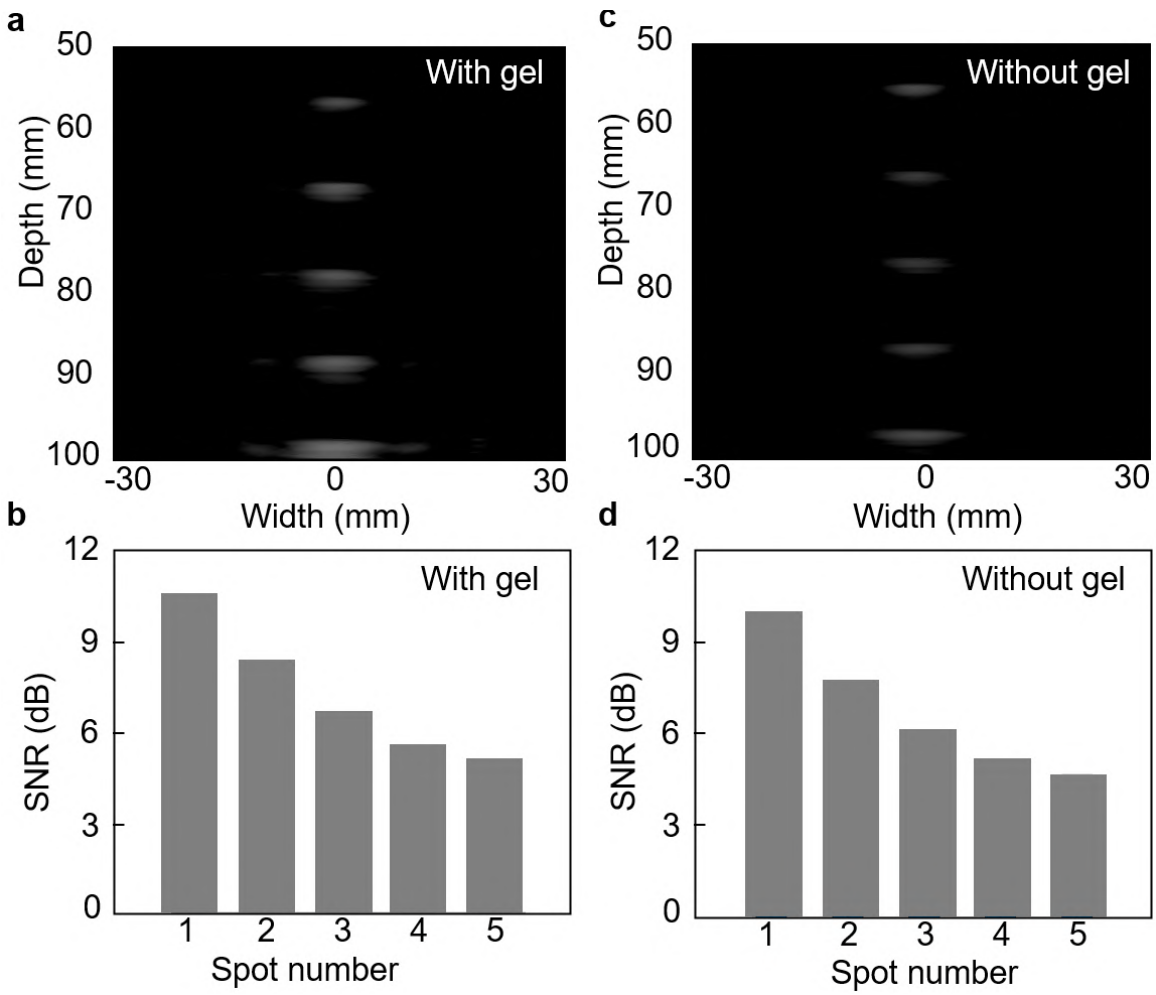

Supplementary Fig. 33 | The imaging results of the stretchable array on a tissue phantom with and without gels. a, Imaging results of the stretchable array with gels. **b,** The SNR of the reflector in a phantom along the imaging axis with gels. **c,** Imaging results of the stretchable array without gels. **d,** The SNR of the reflector in a phantom along the imaging axis without gels.

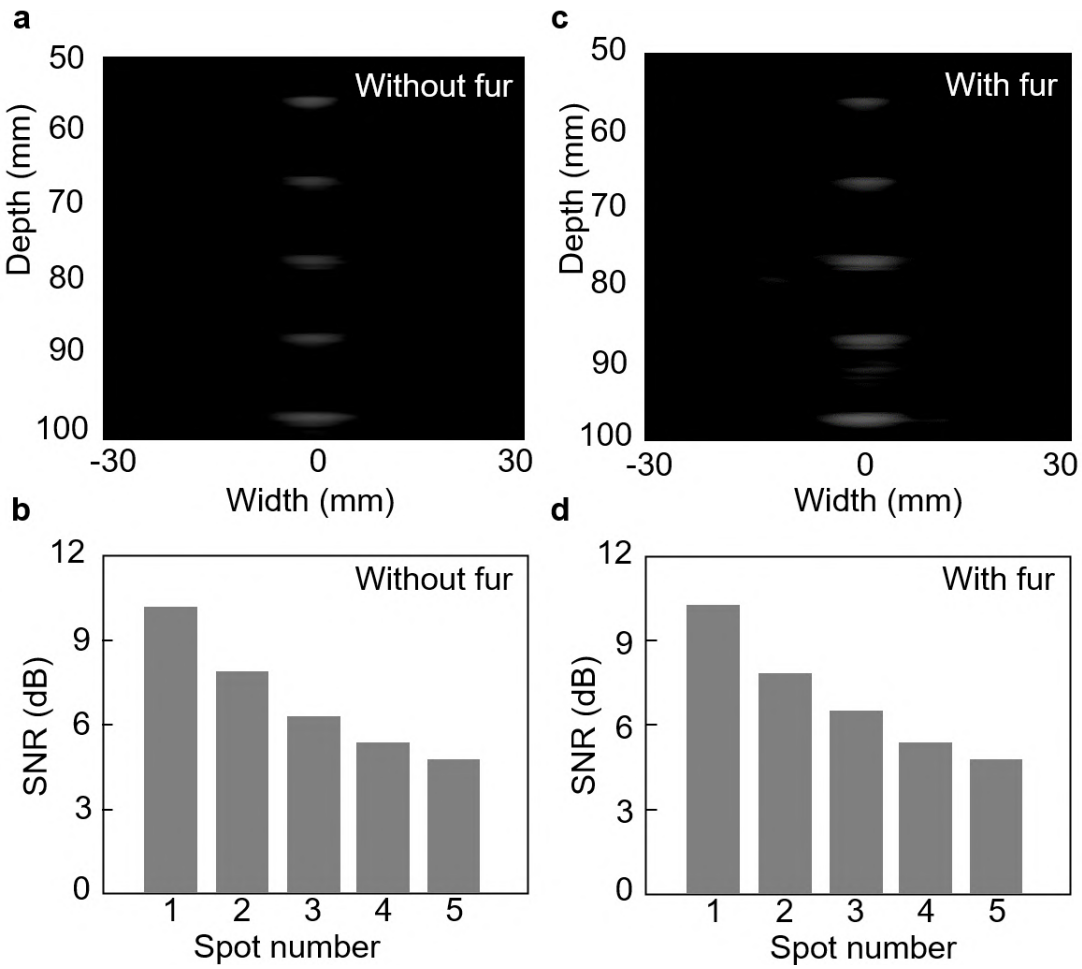

Supplementary Fig. 34 | The imaging results of the stretchable array on a tissue-mimic phantom with the influence of hairs. a, Imaging results of the stretchable array without hairs. **b**, SNR of the reflector in phantom along the imaging axis under without hairs. **c**, Imaging result of the stretchable array with hair. **d**, SNR of the reflector in phantom along the imaging axis with hairs.

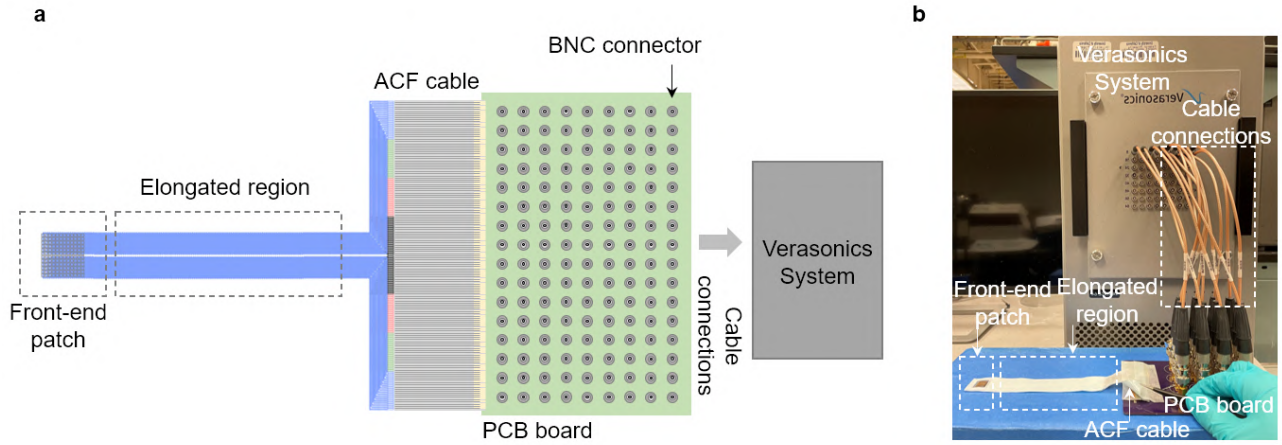

Supplementary Fig. 35 | The connection design between the front-end patch and the post-end Verasonics system. a, A schematic diagram showing the major component of the entire system. **b,** An image showing the actual experimental setup, with all key components labeled in the image.

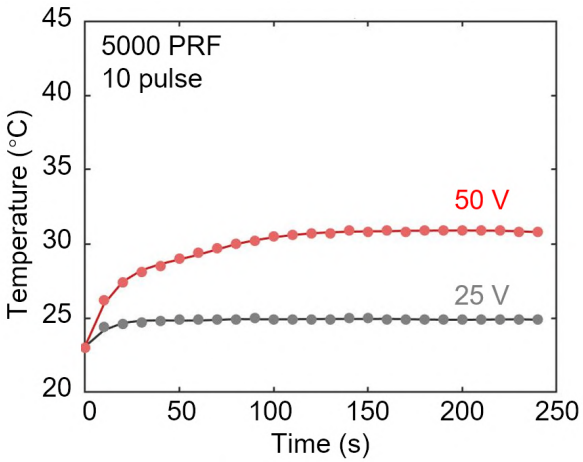

Supplementary Fig. 36 | Device heating comparison using activation voltages of 25 V and 50 V, while keeping the other parameters the same. We characterized 25 V and 50 V activation voltage with 5000 Hz PRF and with pulse number 10 (used in our normal measurements). The results show both 25 V and 50 V (maximum voltage of Verasonics system) excitation voltages have a temperature increase at the device surface, and the temperature gradually becomes stable at around 25°C and 30°C, respectively. These results indicate that the electrical activation can introduce heating to the stretchable patch, and the 25 V activation scheme with 5000 PRF and 10 pulses is more suitable for skin integration application than 50 V.

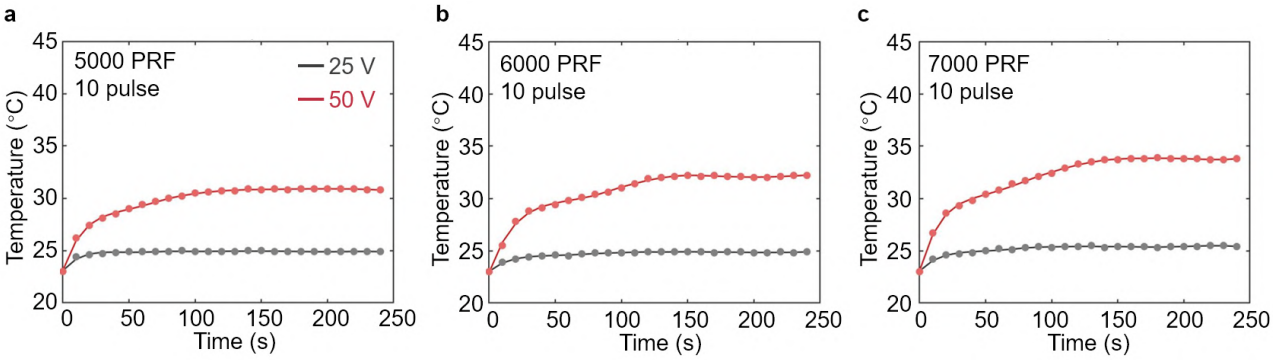

Supplementary Fig. 37 | Device heating characterizations of 25 V and 50 V as the activation voltage under different PRFs, while keeping the pulse length the same. a, 5000 PRF. **b,** 6000 PRF. **c**, 7000 PRF.

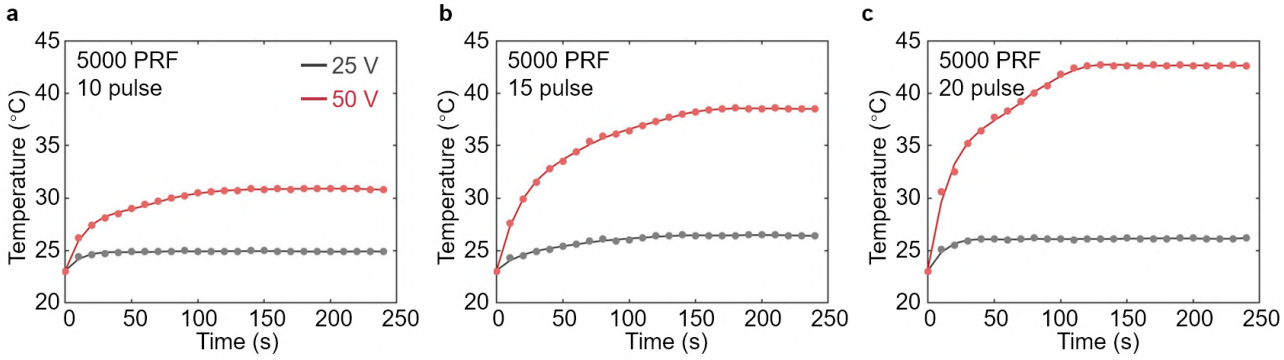

Supplementary Fig. 38 | Device heating characterizations of 25 V and 50 V activation voltages under different pulse lengths, while keeping the PRF the same. a, 10 pulses. **b**, 15 pulses. **c**, 20 pulses.

Video Captions

Video S1 | Phased array steerability. Ultrasonic field mapping of the stretchable phased array when the beam is scanned from -35° to 35° (left panel) in the x-z plane. The actual device position is labeled as the top orange bar, in scale. The dashed circle labels the extraction line (r=30 mm) of the ultrasonic field for analyzing the beam pattern. The right panel shows the corresponding beam pattern of the ultrasonic field.

Video S2 | Comparison of wave propagation of the stretchable phased array on a planar and a curved surface. The left panel shows the simulated ultrasonic wave propagation in the x-z plane on a planar surface, and the right panel shows the simulated results on a complex surface (with a 4.2 cm curvature radius). The device in both situations has a focal depth of 3 cm and a tilting angle of 15°. Each element can generate a pulse wave with encoded time delay and interfere with other pulse waves at the focal point. The locations of elements are labeled in red crosses. The comparison result shows the curvature radius of the skin has a minimal impact on the interaction and focusing of ultrasonic waves of the phased array.

Video S3 | Real-time imaging of the stretchable array on deep tissue phantom. The movie shows the imaging of raw sonograph during the consecutive processes of laminating and removal of the stretchable array. We performed this process for twice. The Verasonics system provided the post-end imaging software.

References

1 Pietrangelo, S. J., Lee, H.-S. & Sodini, C. G. in *Intracranial Pressure & Neuromonitoring XVI* 111-114 (Springer, 2018).

2 Song, I. *et al.* Design and implementation of a new wireless carotid neckband Doppler system with wearable ultrasound sensors: preliminary results. *Appl.* **9**, 2202 (2019).

3 Pashaei, V. *et al.* Flexible Body-Conformal Ultrasound Patches for Image-Guided Neuromodulation. *IEEE Trans. Biomed. Circuits. Syst*. **14**, 305-318 (2019).

4 Bhuyan, A. *et al.* in *2011 IEEE International Ultrasonics Symposium.* 1060-1063 (IEEE).

5 Hu, H. *et al.* Stretchable ultrasonic transducer arrays for three-dimensional imaging on complex surfaces. *Sci. Adv.* **4**, eaar3979 (2018).

6 Wang, C. *et al.* Monitoring of the central blood pressure waveform via a conformal ultrasonic device. *Nat. Biomed. Eng.* **2**, 687-695 (2018).

7 Agrawal, D. R. *et al.* Conformal phased surfaces for wireless powering of bioelectronic microdevices. *Nat. Biomed. Eng.* **1**, 0043 (2017).

8 Cheng, K. C. *et al.* Single crystal PMN-0.33 PT/epoxy 1-3 composites for ultrasonic transducer applications. *IEEE Trans. Ultrason. Ferroelectr. Freq. Control.* **50**, 1177-1183 (2003).

9 Retz, K. *et al.* Measured acoustic intensities for clinical diagnostic ultrasound transducers and correlation with thermal index. Ultrasound Obstet. Gynecol. **50**, 236-241 (2017).

10 Food & Drug Administration. Guide for measuring and reporting acoustic output of diagnostic ultrasound medical devices. Document 510 (k). US. Department of Health and Human Services, FDA. *Center for Devices and Radiological Health, Rockville, MD* (1985).

11 Henderson, J., Willson, K., Jago, J. & Whittingham, T. A survey of the acoustic outputs of diagnostic ultrasound equipment in current clinical use. *Ultrasound Med. Biol.* **21**, 699-705 (1995).

12 Nelson, T. R., Fowlkes, J. B., Abramowicz, J. S. & Church, C. C. Ultrasound biosafety considerations for the practicing sonographer and sonologist. *J. Ultrasound Med.* **28**, 139-150 (2009).

13 Carter, A. & Morley, R. Electric current flow through human skin at power frequency voltages. *Occup. Environ. Med*. **26**, 217-223 (1969).

14 Fish, R. M. & Geddes, L. A. Conduction of electrical current to and through the human body: a review. *Eplasty* **9**, e44, (2009).

15 Shung, K. K., Sigelmann, R. A. & Reid, J. M. Scattering of ultrasound by blood. *IEEE Trans. Biomed. Eng*. 460-467 (1976).